Numerical simulation of rarefied gas flow in micro and vacuum devices

by

Anirudh Singh Rana

A Dissertation Submitted in Partial Fulfillment of the
Requirements for the Degree of

DOCTOR OF PHILOSOPHY

in the Department of Mechanical Engineering

Numerical simulation of rarefied gas flow in micro and vacuum devices

by

Anirudh Singh Rana

Supervisory Committee

Prof. H. Struchtrup, Supervisor
(Department of Mechanical Engineering, University of Victoria)

Prof. B. Buckham, Departmental Member
(Department of Mechanical Engineering, University of Victoria)

Prof. R. Bhiladvala, Departmental Member
(Department of Mechanical Engineering, University of Victoria)

Prof. S. Ibrahim, Outside Member
(Department of Mathematics and Statistics, University of Victoria)

Supervisory Committee

Prof. H. Struchtrup, Supervisor
(Department of Mechanical Engineering, University of Victoria)

Prof. B. Buckham, Departmental Member
(Department of Mechanical Engineering, University of Victoria)

Prof. R. Bhiladvala, Departmental Member
(Department of Mechanical Engineering, University of Victoria)

Prof. S. Ibrahim, Outside Member
(Department of Mathematics and Statistics, University of Victoria)

ABSTRACT

It is well established that non-equilibrium flows cannot properly be described by traditional hydrodynamics, namely, the Navier-Stokes-Fourier (NSF) equations. Such flows occur, for example, in micro-electro-mechanical systems (MEMS), and ultra vacuum systems, where the dimensions of the devices are comparable to the mean free path of a gas molecule. Therefore, the study of non-equilibrium effects in gas flows is extremely important.

The general interest of the present study is to explore boundary value problems for moderately rarefied gas flows, with an emphasis on numerical solutions of the regularized 13–moment equations (R13). Boundary conditions for the moment equations are derived based on either phenomenological principles or on microscopic gas-surface scattering models, e. g., Maxwell's accommodation model and the isotropic scattering model.

Using asymptotic analysis, several non-linear terms in the R13 equations are transformed into algebraic terms. The reduced equations allow us to obtain numerical solutions for multidimensional boundary value problems, with the same set of boundary conditions for the linearized and fully non-linear equations.

Some basic flow configurations are employed to investigate steady and unsteady rarefaction effects in rarefied gas flows, namely, planar and cylindrical Couette flow,

stationary heat transfer between two plates, unsteady and oscillatory Couette flow. A comparison with the corresponding results obtained previously by the DSMC method is performed.

The influence of rarefaction effects in the lid driven cavity problem is investigated. Solutions obtained from several macroscopic models, in particular the classical NSF equations with jump and slip boundary conditions, and the R13–moment equations are compared. The R13 results compare well with those obtained from more costly solvers for rarefied gas dynamics, such as the Direct Simulation Monte Carlo (DSMC) method.

Flow and heat transfer in a bottom heated square cavity in a moderately rarefied gas are investigated using the R13 and NSF equations. The results obtained are compared with those from the DSMC method with emphasis on understanding thermal flow characteristics from the slip flow to the early transition regime. The R13 theory gives satisfying results including flow patterns in fair agreement with DSMC in the transition regime, which the conventional Navier-Stokes-Fourier equations are not able to capture.

Contents

List of Tables

List of Figures

ACKNOWLEDGEMENTS

First and foremost I wish to express my deepest gratitude to my research guide Prof. Henning Struchtrup, for accepting me as his research student and extending all his support and guidance. I acknowledge his inspirations, encouragements and teachings from the bottom of my heart.

My special thanks to Prof. Manuel Torrilhon at RWTH Aachen (Germany) for his valuable suggestions during my Ph.D. work, and also for his support during my visit to ETH Zurich (Switzerland) and RWTH Aachen (Germany). I also thank Vinay Gupta, Paul Weber, Dr. James McDonald and Armin Westerkamp for their kind help and support during my visit to Aachen. In particular, Vinay, to whom I extend my special thanks for carefully proof-reading this dissertation.

I deeply acknowledge the support from my friends and colleagues Dr. Peter Kauf, Dr. Peyman Taheri, Michael Fryer, Tom Burdyny, Behnam Rahimi, Alireza Mohammadzadeh. I would like to thank my teachers and friends at CMS University of Pune (India), Prof. Mihir Arjunwadkar, Prof. Sukratu Barve, Dr. William Sawyer, Absar, Anvesh, Ashwini, Gayatri, Maneesha and Neelakshi.

I would also like to express my appreciation to various Professors of UVic as well as the technical and administrative staff at Department of Mechanical Engineering who helped me directly or indirectly during my research. I express my profound gratitude to all past teachers and mentors for imbibing good values in my character.

My deepest gratitude goes to my parents for their love and blessings. I thank Davendra, Vikram, Ruby, Abhimanyu, Urvashi, Yogita, Sourabh, Haresh, Pragya, Rananjay and all my family members, friends and relatives from the bottom of my heart. Without their love, support and help, this research would never be finished.

Finally, I thank the almighty God *Sri Ram* for his blessings and wisdom.

I sincerely acknowledge the funding from Natural Sciences and Engineering Research Council (NSERC) of Canada.

Anirudh Singh Rana

Victoria, BC

O Lord, I am offering you what you have bestowed on me.

Chapter 1

Introduction

As a result of the recent technological advances of micro- and nano-machining and fabrication, the miniaturization of mechanical and electrical devices has become an important focus of interest. Gas flows in micro-systems—such as, micro heat-exchangers [47], micro pumps and turbines [25, 29], micro-sensors and pressure gauges [21] and other Micro/Nano Electro Mechanical Systems (MEMS/NEMS)—are of great importance due to their tremendous industrial and scientific potential. Therefore, a good understanding of the hydrodynamics and heat transport mechanisms of rarefied gas flows is crucial in designing, fabricating, and operating these devices.

Simulation of gas flows in micro systems are, however, more challenging than those in classical gas dynamics, since gas rarefaction leads to the breakdown of the underlying assumptions of the classical theory, i. e., the Navier-Stokes-Fourier (NSF) equations. Gases exhibit rarefaction effects when the characteristic length scale of the system becomes comparable to the mean free path λ, which is defined as the average distance traveled by a molecule between successive collisions.

The degree of rarefaction in a gas is characterized by the Knudsen number, Kn, which is defined as the ratio of the molecular mean free path to the macroscopic length scale of the device. Based on the value of the Knudsen number, the gas flow can be classified into four regimes—namely, hydrodynamic flow regime (for $\mathrm{Kn} \lesssim 0.001$), slip flow regime (for $0.001 \lesssim \mathrm{Kn} \lesssim 0.1$), transition regime (for $0.1 \lesssim \mathrm{Kn} \lesssim 10$), and free molecule flow regime (for $\mathrm{Kn} \gtrsim 10$) [47].

It is commonly accepted that the classical description based on the NSF equations is only valid in the hydrodynamic flow regime. Micro-electrical-mechanical systems are usually operated in air at standard conditions, for which the mean free path is $\approx 0.065\mu m$ [47]. Therefore, for gas flows in MEMS the Knudsen number is not

sufficiently small to guarantee the validity of the NSF equations and the processes in MEMS need be modelled with more accurate transport models.

For flows outside the hydrodynamic regime, many interesting rarefaction effects—such as, velocity slip and temperature jump at the walls [62, 63, 61, 89, 104], Knudsen paradox, Knudsen layers [49, 50, 60], transpiration flow [46, 76, 75, 93], thermal stress [89, 93], heat flux without temperature gradients [89, 104], etc.—are observed. These effects are termed as non-equilibrium effects and they cannot be described by the classical NSF equations. The range of validity of the NSF equations may further be extended to the slip flow regime by applying appropriate slip and jump boundary conditions to model the velocity slip and temperature jump at the walls, as well as transpiration flows. However, they still cannot describe the Knudsen layers and other rarefaction effects.

Non-equilibrium effects are also encountered when the pressure in the system becomes small, as in ultra vacuum systems [27] or in the outer atmosphere [7]. Since the mean free path in the gas is inversely proportional to the density, the mean-free-path becomes comparable to macroscopic length scales at sufficiently low pressure.

The processes in any flow regime can be well described by the Boltzmann equation which is the evolution equation for the *distribution function* of the gas particles [17, 16, 51, 120]. The Boltzmann equation requires detailed information of phase space and thus the direct solution of the Boltzmann equation typically requires huge computational time. An alternative to the direct solution of the Boltzmann equation is offered by macroscopic transport models, which capture micro-scale effects with reasonable compromise between computational effort and desired accuracy [73, 97, 52]. In macroscopic theories, the behavior of a gas is described through physical quantities such as mass density, temperature, velocity, heat flux, stress tensor, and so on. The goal of these macroscopic transport models is to reduce the high dimensional phase space of the particle description to a low-dimensional continuum model by relating the physical quantities as *moments* of the distribution function.

The macroscopic models, usually, consist of partial differential equations—which are referred to as *moment equations*—describing the evolution of the macroscopic quantities. Moment equations are obtained by an asymptotic reduction of the Boltzmann equation at different levels of approximation [73, 51, 97, 52]. Conventionally, these equations are derived based on either the Chapman–Enskog expansion method [19, 51, 97], or Grad's moment method [32, 33, 97].

The Chapman–Enskog expansion method relies on an asymptotic expansion of the

Boltzmann equation in powers of the Knudsen number [19, 51, 97]. The NSF equations are obtained from first order expansion, while second and third order expansions result in the Burnett and super-Burnett equations, respectively [19, 8, 51, 97]. However, Burnett and super-Burnett equations lack a complete set of boundary conditions and are usually unstable for time-dependent problems [8, 9]. During the last decade, several modified forms of the Burnett equations have been suggested in the literature [128, 11, 10, 88, 44] that are, indeed, stable; however, at present no boundary conditions are available for any of these sets of equations. The 13-moment equations, obtained via Grad's moment method are always linearly stable. However, due to their hyperbolic character, they produce unphysical sub-shocks for the flows with Mach number, Ma $\gtrsim$ 1.65 [117, 4]. Furthermore, the non-linear Grad's moment equations lack suitable boundary conditions.

To overcome the drawbacks of both these methods, Struchtrup and Torrilhon [102, 96, 97] regularized the 13-moment equations by combining elements of the Chapman-Enskog expansion method and Grad's moment method, and using the order of magnitude analysis in the Knudsen number up to third order. This resulted in the regularized 13-moment (R13) equations, which contain the classical Burnett and super-Burnett equations asymptotically, see, e.g., the textbook [97]. The R13 equations are always stable [96] and give smooth shock structures for all Mach numbers, particularly, in good agreement with kinetic theory for Ma $\lesssim$ 3 [117]. Furthermore, the linear R13 equations are accompanied by an H-theorem [103], and are equipped with a complete set of boundary conditions [118].

The R13–moment equations have been considered for bulk processes, such as stability and sound propagation [102, 97], shock waves [117], and two-dimensional (2D) bulk numerical simulations [111]. The boundary problems studied using the linear R13–moment equations so far include planar and cylindrical Couette and Poiseuille flows, transpiration flows, acoustic resonators, and gas flow past a sphere and a cylinder [108, 107, 12, 100, 113, 124], among others.

In this dissertation, we concentrate on numerical solutions for the R13–moment equations for non-linear problems. The main objective is the implementation of a computationally efficient, yet accurate, macroscopic description of moderately rarefied flows, so as to gain a better understanding of hydrodynamic and heat transfer processes in micro and vacuum devices.

1.1 Outline

The contents of this dissertation are thematically divided into two parts with 10 chapters. In Part I, which includes four chapters, we introduce background and theory of moment equations and present various type of boundary conditions. Part II includes six chapters, where we present simulation results for the different boundary value problems.

Part I: BACKGROUND AND THEORY

Basic concepts in kinetic theory of gases are presented in **Chapter 2**, where the Boltzmann equation, velocity distribution function, moments and the conservation laws are introduced.

Chapter 3 presents sets of moment equations which are used in subsequent parts of this dissertation. Particular attention is given to the regularized 13–moment (R13) and regularized 10–moment (R10) equations. It turns out that the original non-linear R13 equations need a higher number of boundary conditions than the linearized equations, so this issue is discussed in Section (3.2.3). As part of the preparation of the R13 equations for the numerical scheme, in Section (3.2.3), we use order of magnitude arguments to rewrite the non-linear part of the R13 equations such that the third order accuracy is maintained, but linear and nonlinear equations require the same number of boundary conditions. A regularization of Levermore's 10 moment equations [56, 55] is derived in Section (3.3). The proposed approach to obtain the R10 equations is founded on the framework of phenomenological linear irreversible thermodynamics.

Chapter 4 introduces various gas-surface interaction models in kinetic theory. Macroscopic boundary conditions based on Maxwell's accommodation model are introduced in Section (4.1.2). In Section (4.2), we develop macroscopic adiabatic wall boundary conditions by using an isotropic scattering model. Additionally, in Section (4.4), we propose a general phenomenological theory of boundary conditions for the R13 and R10 equations. The resulting boundary conditions contain free parameters (Onsager coefficients) that can be adjusted to measurements. With properly chosen coefficients, the boundary conditions agree with those from the Maxwell model.

Part II: SOLUTIONS OF BOUNDARY VALUE PROBLEMS

Chapter 5 introduces analytic solutions for the linearized R13 and NSF equations by using them to address the classical problems of viscous slip and temperature jump. In Section (5.3) and Section (5.4), we discuss slip and jump coefficients obtained from

the R13 equations and compare them with more accurate kinetic solutions.

Through **Chapters 6** to **9**, a collection of benchmark boundary value problems for different geometries and processes are solved numerically for the different macroscopic moment equations and boundary conditions.

In **Chapter 6**, we present numerical solutions of the R13, R10, R21, and NSF equations for 1D nonlinear problems, e. g., Couette flow and steady state heat transfer, and compare the results with other theories.

In **Chapter 7**, we present a 2D finite difference scheme to compute steady state solutions for the lid driven cavity problem. Lid driven cavities with isothermal boundaries and mixed boundaries (adiabatic-isothermal) are considered in Section (7.1), and Section (7.4), respectively. Some results presented in this chapter are published in [80].

Flow and heat transfer in a bottom heated square cavity is investigated in **Chapter 8**, by using the R13 equations and the Navier-Stokes-Fourier equations. The results obtained are compared with those from the Direct Simulation Monte Carlo (DSMC) method. Some preliminary results related to those presented in this chapter are published in [119].

In **Chapter 9**, we derive a Kinetic-Flux-Vector-Splitting (KFVS) based finite volume method for the R13 equations, results of which were published in [79]. Numerical solutions for the unsteady Couette flow and oscillatory Couette flow are presented in Section (9.2.4) and Section (9.3), respectively. In Section (9.4), we present our preliminary results for linear R13 equations, obtained using in/out flow boundary conditions.

The dissertation ends with our final conclusions and recommendations, given in **Chapter 10**.

1.2 Original contributions

In **Chapter 3** we present a set of modified R13 equations which are derived from the original R13 equations. This new set of equations requires the same number of boundary conditions for both linear and nonlinear equations and also consistent with the original R13 equations up to third order. The modified R13 equations are used in the subsequent chapters to study boundary value problems. The results were published in [80].

In **Chapter 3** we derive a set of the R10 moment equations based on the second law of thermodynamics.

In **Chapter 4** we develop an adiabatic wall boundary conditions for the R13 equations using an isotropic scattering model. Unlike previous studies using the Maxwell accommodation model, the isotropic scattering model allows us to study the adiabatic-rough surfaces for the R13 equations.

In **Chapter 4** we derive a set of phenomenological boundary conditions for the linearized R13 equations which respect the second law of thermodynamics. We study the linearized R13 equations to investigate viscous slip and jump coefficients in the boundary conditions in **Chapter 5**.

Form **Chapter 6** to **Chapter 8**, we explore many one and two dimensional boundary value problems by using the Navier-Stokes-Fourier equations, Modified R13 equations, and the R10 equations, etc., and compare the numerical solutions with the direct simulation Monte Carlo simulations. It is seen that the R13 equations gives better results then the R10 and the Navier-Stokes-Fourier equations and compares well with more accurate theories for moderate Knudsen numbers. The results were published in [80, 79, 119].

In **Chapter 9** we develop a finite volume based numerical method for the R13, R10 and Navier-Stokes-Equations. The derived method allows as to simulate non-stationary problems with emphasis on the correct implementation of the complex boundary conditions and numerical fluxes. The results were published in [79].

Part I

BACKGROUND AND THEORY

Chapter 2

Kinetic theory

In this chapter we shall first review the elementary kinetic theory of a monatomic gas and introduce the Boltzmann equation, which is the fundamental governing equation for processes in dilute gases. Then, we shall discuss some of its direct consequences, and the standard methods—namely, the DSMC method and Chapman–Enskog expansion method—for solving it. We shall also discuss the macroscopic equations of continuum mechanics, such as the continuity equation, the momentum balance equation, and the energy balance equation. Excellent references for this chapter are [51][52][97].

2.1 Boltzmann equation

In kinetic theory a gas is described by a distribution function $f(t, x_i, c_i)$ such that $f d\mathbf{x} d\mathbf{c}$ denotes the number of particles which at time t are situated at $\mathbf{x} \in [\mathbf{x}, \mathbf{x} + \mathbf{dx}]$ and have a microscopic velocity $\mathbf{c} \in [\mathbf{c}, \mathbf{c} + \mathbf{dc}]$. The Boltzmann equation describes the evolution of the distribution function in phase space $(\mathbf{x}, \mathbf{c})$ by accounting for the motion and collisions of the particles in the gas, as [17][51]

$$\frac{\partial f}{\partial t} + c_k \frac{\partial f}{\partial x_k} + G_k \frac{\partial f}{\partial c_k} = \mathcal{S}(f, f_*), \tag{2.1}$$

where G_k is the external force per unit mass acting on the gas and is assumed to be independent of the microscopic velocity $\mathbf{c}$, e.g., gravity. The term $\mathcal{S}(f, f_*)$ is the collision operator (or Boltzmann collision operator) that describes the change of the distribution function due to interaction between particles. While writing the Boltzmann equation (2.1), it is assumed that the gas is dilute enough so that the probability

of collisions where three or more molecules participate is negligible in comparison to binary encounters. Furthermore it is also assumed that the collisions are elastic, microreversible and that molecular chaos prevails [17]. Under these assumptions, one can derive the bilinear collision operator $\mathcal{S}(f, f_*)$, as [17][51]

$$\mathcal{S}(f, f_*) = \int \int_0^{2\pi} \int_0^{\pi/2} \left(f' f'_* - f f_* \right) g\sigma \sin\Theta d\Theta d\varepsilon d\mathbf{c}_* \tag{2.2}$$

where f and f_* are the distribution functions of the colliding molecules (and prime denotes the distribution functions after collision), Θ is the collision angle, g is the relative velocity between the two colliding molecules, and ε is the azimuth angle in collision plane which describes the orientation of the collision plane, see Ref. [17] .

The Boltzmann equation is an integrodifferential equation for f in seven independent variables, which are the time t, the three physical coordinates x_i, and three velocity components c_i. The mathematical difficulty associated with the Boltzmann equation is further compounded by the integral form of the nonlinear collision term $\mathcal{S}(f, f_*)$.

2.2 Macroscopic variables

For many processes, the main interest is not the detailed knowledge of the distribution function f, but the knowledge of its macroscopically relevant moments such as mass density, macroscopic velocity, temperature, etc.

In kinetic theory, these macroscopic quantities are defined as average values of the microscopic quantities of the gas molecules such as mass m, momentum, mc_i and kinetic energy $mc^2/2$. For example, mass density ρ, macroscopic velocity v_i, and absolute temperature T are identified as the moments of the distribution, through

$$\rho = m \int f d\mathbf{c}, \quad \rho v_i = m \int c_i \, f \, d\mathbf{c}, \text{ and } \quad \rho \mathrm{R} T = \frac{m}{3} \int C^2 \, f \, d\mathbf{c}, \tag{2.3}$$

where R is the gas constant and $C_i = c_i - v_i$ is the peculiar velocity, defined as the velocity of a molecule relative to the flow velocity. For convenience, we shall write temperature T in energy units as $\theta = \mathrm{R}T$.

The pressure tensor p_{ij}, and the heat flux vector q_i are the second and contracted

third order moments of the distribution function f, respectively, i.e.,

$$p_{ij} = m \int C_i C_j \, f \, d\mathbf{c}, \text{ and } \quad q_i = \frac{m}{2} \int C^2 C_i \, f \, d\mathbf{c}. \tag{2.4}$$

The other higher-order moments do not have any physical meaning in general. Nevertheless, it is useful to define them in symmetric traceless form as following [97, 120]

$$u^a_{i_1 i_2 .. i_n} = m \int C^{2a} C_{\langle i_1} C_{i_2} ... C_{i_n \rangle} f d\mathbf{c}. \tag{2.5}$$

Here, indices inside angular brackets denote the symmetric trace-free part of tensors [97]. From the definition of generic moments (2.5), one immediately identifies that

$$u^0 = \rho, \quad u^0_i = 0, \quad u^1 = 3\rho\theta, \text{ and } \quad u^1_i = 2q_i.$$

Furthermore, the pressure tensor is expressed in terms of its trace and traceless part as

$$p_{ij} = p\delta_{ij} + u^0_{ij}, \tag{2.6}$$

where δ_{ij} is the Kronecker delta tensor, $u^0_{ij} = \sigma_{ij}$ is the deviatoric stress tensor, and $p = p_{kk}/3$ is the pressure, given by the ideal gas equation of state as $p = \rho\theta$.

2.3 General equation of transfer and conservation laws

The multiplication of the Boltzmann equation (2.1) by an arbitrary function $\Psi_A(\mathbf{x}, t, \mathbf{c})$ and subsequent integration over the microscopic velocity space yields the *transfer equation* for the property $\rho\langle\Psi_A\rangle$, [17, 97, 52]

$$\frac{\partial \rho \langle \Psi_A \rangle}{\partial t} + \frac{\partial \rho \langle \Psi_A c_k \rangle}{\partial x_k} - \rho \left\langle \frac{\partial \Psi_A}{\partial t} \right\rangle - \rho \left\langle c_k \frac{\partial \Psi_A}{\partial x_k} \right\rangle - \rho \left\langle G_k \frac{\partial \Psi_A}{\partial c_k} \right\rangle = \mathcal{P}_{\Psi_A}, \tag{2.7}$$

where $\rho\langle\Psi_A\rangle$ denotes the weighted average of Ψ_A, defined as

$$\rho \langle \Psi_A \rangle = m \int \Psi_A f d\mathbf{c}, \tag{2.8}$$

and the production term $\mathcal{P}_{\Psi_A}$ is given by

$$\mathcal{P}_{\Psi_A} = m \int \Psi_A \mathcal{S}\left(f, f_*\right) d\mathbf{c} = m \int \int \int_0^{2\pi} \int_0^{\pi/2} \Psi_A \left(f' f'_* - f f_*\right) g\sigma \sin\Theta d\Theta d\varepsilon d\mathbf{c}_* d\mathbf{c}. \tag{2.9}$$

2.3.1 Conservation laws

Clearly, from (2.8), $\rho\langle 1\rangle = \rho$, $\rho\langle c_i\rangle = \rho v_i$, $\rho\langle C^2/3\rangle = \rho\theta$. The conservation laws—which are the evolution equations for mass density ρ, macroscopic velocity v_i, and temperature θ—are obtained from the transfer equation (2.7) by choosing $\Psi = 1$, c_i and $\frac{1}{2}C^2$, respectively

$$\text{mass conservation}: \frac{D\rho}{Dt} + \rho\frac{\partial v_k}{\partial x_k} = 0, \tag{2.10a}$$

$$\text{momentum conservation}: \frac{Dv_i}{Dt} + \frac{1}{\rho}\frac{\partial(p\delta_{ik} + \sigma_{ik})}{\partial x_k} = G_i, \tag{2.10b}$$

$$\text{energy conservation}: \frac{3}{2}\frac{D\theta}{Dt} + \theta\frac{\partial v_k}{\partial x_k} + \frac{\sigma_{ik}}{\rho}\frac{\partial v_i}{\partial x_k} + \frac{1}{\rho}\frac{\partial q_k}{\partial x_k} = 0. \tag{2.10c}$$

Here, t and x_i are temporal and spatial coordinates, respectively and $D/Dt \equiv \partial/\partial t + v_k\partial/\partial x_k$ is the material derivative. The collision terms vanish because mass, momentum and energy are conserved quantities.

Equations (2.10) are the fundamental equations of continuum mechanics. However, they can not be solved as they stand, since they contain the stress tensor σ_{ik} and heat-flux q_i as unknowns. In order to close the system in (2.10), constitutive relations—which express the unknowns σ_{ik}, and q_k in terms of the variables ρ, v_i and θ—are needed.

2.3.2 Classical theory

The classical hydrodynamic equations describing viscous flow are obtained from the Navier-Stokes-Fourier (NSF) equations. In NSF theory, shear stress and heat flux are described according to the laws of Newton and Fourier, respectively, i.e.,

$$\sigma_{ij} = -2\mu\frac{\partial v_{\langle i}}{\partial x_{j\rangle}}, \tag{2.11}$$

$$q_i = -\kappa\frac{\partial\theta}{\partial x_i}, \tag{2.12}$$

where μ and κ, are the viscosity, and thermal conductivity of the gas, respectively; they are functions of temperature alone. Equations (2.10) with the closure (2.11)–(2.12) result into NSF equations.

Obviously, the NSF equations pose a mathematically less complex problem than the Boltzmann equation. However, the NSF equations are inadequate in terms of accurately describing strong non-equilibrium flows, especially in circumstances such as those encountered for rarefied gases. To explain the rarefaction effects, several extended macroscopic transport equations are proposed, which can describe the flows beyond the hydrodynamic (NSF) limit. These will be discussed in detail in the next chapter.

The most accurate description of gas flows is provided by the Boltzmann equation itself, which is valid for flows at all Knudsen numbers. Because of the complexity in the Boltzmann collision operator $\mathcal{S}$, one is often interested in model equations which are easier to handle than the Boltzmann equation but which should also have the same fundamental properties, listed in next section.

2.3.3 Some properties of the Boltzmann equation

- Collision invariants:

It can be shown [17, 52] that for any distribution function f,

$$\mathcal{P}_\Psi = \int \Psi(\mathbf{c})\, \mathcal{S}(f, f_*)\, d\mathbf{c}$$

vanishes if and only if

$$\Psi(\mathbf{c}) = \mathsf{x} + \mathsf{y}_k c_k + \mathsf{z} c^2 \tag{2.13}$$

where x, y_k, and z are any arbitrary functions independent of $\mathbf{c}$.

- Equilibrium distribution function:

The collision operator on the right-hand side of the Boltzmann equation (2.1) describes the change of the distribution function due to interaction between particles. This change should vanish when a gas is in equilibrium state, therefore

$$\mathcal{S}(f|_{\mathrm{E}},\ f|_{\mathrm{E}}) = 0,$$

where $f|_{\mathrm{E}}$ represents the equilibrium distribution function. The above equation is fulfilled when $f|_{\mathrm{E}} f|_{\mathrm{E}} = f^{'}|_{\mathrm{E}} f^{'}|_{\mathrm{E}}$, i.e., $\ln f|_{\mathrm{E}}$ is a collision invariant. Therefore, according to (2.13), $\ln f|_{\mathrm{E}}$ must be of form

$$\ln f|_{\mathrm{E}} = \mathsf{x} + \mathsf{y}_k c_k + \mathsf{z} c^2.$$

The quantities x , y_k and z are determined from the substitution of the last equation into (2.3), which by using the positiveness and integrability of the $f|_{\mathrm{E}}$, yields [17, 52]

$$f|_{\mathrm{E}} = \frac{\rho}{m\sqrt{2\pi\theta}^3} \exp\left(-\frac{C^2}{2\theta}\right). \tag{2.14}$$

which is the Maxwellian distribution.

- H-theorem:

The next direct consequence of the Boltzmann equation is the so-called Boltzmann H-theorem. The Boltzmann H-function is defined as

$$\eta = -k_B \int f \ln \frac{f}{y} d\mathbf{c},$$

where k_B is the Boltzmann constant and y is another constant having the dimensions of the distribution function. The equation of transfer for η is obtained by taking $\Psi_A = -k_B \ln \frac{f}{y}$ in (2.7). It reads

$$\frac{\partial \eta}{\partial t} + \frac{\partial \Phi_k}{\partial x_k} = \Sigma \geq 0, \tag{2.15}$$

where

$$\Phi_k = -k_B \int f c_k \ln \frac{f}{y} d\mathbf{c}, \text{ and } \quad \Sigma = \mathcal{P}_{-k \ln \frac{f}{y}}.$$

Here, η always has a positive production and it is bounded. Furthermore, in an isolated system, η is a monotonically increasing, and hence η must approach to a maximum limit as $t \to \infty$.

The H-theorem in kinetic theory is equivalent to the second law of thermodynamics, which states: *The entropy of an isolated system not in equilibrium will increase over time, until it attends a maximum value at equilibrium.* Therefore, η can be

considered as the entropy density of the gas by defining

$$\eta = \rho s = -k_B \int f \ln \frac{f}{y} d\mathbf{c}, \tag{2.16}$$

where s denotes the specific entropy of the gas. For convenience, we shall write entropy s in energy units as $s = \mathrm{R}s$.

The specific entropy of a monatomic gas in equilibrium follows from (2.16), when evaluated using the Maxwellian (2.14), as

$$s = \ln \frac{\theta^{3/2}}{\rho} + s_0 \quad \text{where} \quad s_0 = \frac{3}{2} + \ln \left(my\sqrt{2\pi}^3 \right). \tag{2.17}$$

2.4 Collision operator and kinetic models

The collision operator $\mathcal{S}$ in the Boltzmann equation (2.1) requires the definition of the intermolecular force between two considered molecules. This intermolecular force is repulsive at short distances and weakly attractive at large distances. For a general intermolecular force, $\mathcal{S}$ is very difficult to evaluate, therefore, various models have been proposed to describe the intermolecular force. The more classic one is the so-called inverse power law (IPL) model [17, 7]. In this model the intermolecular force is purely repulsive, and is obtained from an intermolecular potential

$$\phi(r) \propto \frac{1}{(\eta - 1)\, r^{(\eta - 1)}}, \tag{2.18}$$

where η is a constant and r denotes the distance between the centers of two molecules. The intermolecular force is given by $-\frac{d\phi}{dr}$.

Inverse power law potentials do not describe particle attraction that leads to condensation at low temperature. Attraction forces can be neglected as long as the temperatures in a process are well above the saturation or critical temperatures. For power potentials, the temperature dependency of the viscosity μ and the thermal conductivity κ of the gas is given by [17, 97]

$$\mu = \mu_0 \left(\frac{T}{T_0} \right)^{\omega}, \text{ and } \quad \kappa = \frac{5}{2} \frac{\mu}{\mathrm{Pr}}, \tag{2.19}$$

where μ_0 is the viscosity at reference temperature T_0, $\omega = (\eta + 3) / (2\eta - 2)$ is the viscosity exponent, and Pr is the Prandtl number.

Many binary collision models based on the IPL assumption are described in the literature, e.g., Maxwell molecule (MM) model, hard sphere (HS) model and variable hard sphere (VHS) model, are based on the IPL model. The HS model—which assumes that the total collision cross-section σ is constant and the viscosity μ is proportional to the square root of the temperature—may be derived from the IPL by choosing $\eta \to \infty$ and $\omega = 1/2$ [17]. For VHS it is assumed that the particles with higher relative velocity have a bigger cross section. Another classic model are Maxwell molecules (MM), which are a special case of the inverse power law model with $\eta = 5$, which gives $\omega = 1$.

2.4.1 Kinetic models

In the context of kinetic theory, approximations to the Boltzmann equation are obtained by using simplified collision models. The Boltzmann equation can be simplified by making approximations of the collision operator $\mathcal{S}$ in Eq. (2.2).

BGK model

The most classical kinetic model was proposed by Bhatnagar, Gross and Krook [6] and is called the BGK model. It has the following form

$$\mathcal{S}|_{\mathrm{BGK}} = -\nu \left(f - f|_{\mathrm{E}} \right),$$

where $f|_{\mathrm{E}}$ is the local equilibrium distribution and ν is the mean collision frequency. The collision frequency ν is independent of molecular velocity, it is given by (from CE expansion, see Section 2.5)

$$\nu = \frac{p}{\mu}.$$

Evidently, the BGK equation gives the correct solution $f = f|_{\mathrm{E}}$ at equilibrium and guarantees the conservation of mass, momentum and energy. Also the H-theorem can be proved for the BGK model [6]. However, the BGK model yields an incorrect value for the Prandtl number $\mathrm{Pr}\,|_{\mathrm{BGK}} = 1$, whereas the correct value for the Prandtl number for monatomic gases is 2/3 [17].

ES-BGK model

Many statistical models for constructing the collision term have been put forward which give the correct Prandtl number, typical examples are the ES-BGK [42] and the S-model [85]. In the ES-BGK model the Maxwellian that appears in the original BGK model is replaced with an anisotropic Gaussian so that the collision term now reads

$$\mathcal{S}|_{\mathrm{ES-BGK}} = -\nu \left(f - f|_{\mathrm{ES}} \right), \tag{2.20}$$

where

$$f|_{\mathrm{ES}} = \frac{\rho}{m\sqrt{\det\left(2\pi\lambda_{ij}\right)}} \exp\left[-\frac{1}{2}\lambda_{ij}^{-1} C_i C_j \right], \tag{2.21}$$

and the matrix λ_{ij} is given by

$$\lambda_{ij} = \theta\delta_{ij} + b\frac{\sigma_{ij}}{\rho}, \text{ with } \quad -\frac{1}{2} \leq b \leq 1. \tag{2.22}$$

In Eq. (2.22), σ_{ij} is the stress tensor, b is a parameter which can be adjusted to yield the proper Prandtl number; later, in Section 2.5, we shall show that $b = 1 - \frac{1}{\mathrm{Pr}}$. The ES-BGK model conserves mass, momentum and energy. Also the H-theorem can be proved for the ES-BGK model [1].

These kinetic models offer a significant computational advantage over the full collision operator in many practical situations [85]. However, despite these simplifications kinetic models still give an integro–partial differential equation and their numerical solutions are very involved. Therefore, there is a strong desire for macroscopic models that allow the calculation of processes in the transition regime at lower computational cost.

A variety of macroscopic models can be derived from the Boltzmann equation, which aim at describing rarefied gas flows at least approximately [97]. The best known among these are the Burnett and super-Burnett equations, derived by means of the Chapman Enskog method [51, 97]. This method is rather involved and will be presented here only in outline. A detailed discussion of the Chapman-Enskog (CE) method can be found in [51, 97, 52, 19].

2.5 Chapman-Enskog (CE) method

In the CE method, the distribution function f is expanded in powers of a smallness parameter ϵ as

$$f = f^{(0)}\left(1 + \epsilon f^{(1)} + \epsilon^2 f^{(2)} \ldots\right), \tag{2.23}$$

where $f^{(0)}$, $f^{(1)}$ and $f^{(2)}$ represent the first, second and third order approximation to the distribution function, respectively, and so on. The parameter ϵ is usually the Knudsen number. Inserting (2.23) into the Boltzmann equation (2.1) and assuming that the conserved quantities are same at any level of expansion, i.e.

$$\begin{aligned}
\rho &= m\int f d\mathbf{c} = m\int f^{(0)} d\mathbf{c}, \\
\rho v_i &= m\int c_i f d\mathbf{c} = m\int c_i f^{(0)} d\mathbf{c}, \\
\rho\theta &= \frac{m}{3}\int C^2 f d\mathbf{c} = \frac{m}{3}\int C^2 f^{(0)} d\mathbf{c},
\end{aligned}$$

and

$$0 = m\int f^{(\alpha)} d\mathbf{c}, \quad 0 = m\int c_i f^{(\alpha)} d\mathbf{c}, \quad 0 = m\int C^2 f^{(\alpha)} d\mathbf{c}, \quad \forall \alpha > 0,$$

we get [51, 97, 52]

$$f^{(0)} = f|_{\mathrm{E}} = \frac{\rho}{m\sqrt{2\pi\theta}^3}\exp\left(-\frac{C^2}{2\theta}\right). \tag{2.24}$$

Accordingly, the Chapman-Enskog expansions for the stress tensor and for the heat flux vector are

$$\sigma_{ij} = \sigma_{ij}^{(0)} + \epsilon\sigma_{ij}^{(1)} + \epsilon^2\sigma_{ij}^{(2)} + \ldots, \text{ and } \quad q_i = q_i^{(0)} + \epsilon q_i^{(1)} + \epsilon^2 q_i^{(2)} + \ldots, \tag{2.25}$$

where

$$\sigma_{ij}^{(\alpha)} = m\int C_{\langle i} C_{j\rangle} f^{(\alpha)} d\mathbf{c}, \text{ and } q_i^{(\alpha)} = \frac{m}{2}\int C^2 C_i f^{(\alpha)} d\mathbf{c}.$$

Equation (2.24) gives zeroth order contribution for the pressure tensor and the heat flux vector, as

$$\sigma_{ij}^{(0)} = m\int C_{\langle i} C_{j\rangle}\, f|_{\mathrm{E}}\, d\mathbf{c} = 0 \text{ and } q_i^{(0)} = \frac{m}{2}\int C^2 C_i\, f|_{\mathrm{E}}\, d\mathbf{c} = 0. \tag{2.26}$$

The conservation laws (2.10a-2.10c) along with (2.26) are called the Euler equations. The Euler equations are the fundamental hydrodynamic equations for non-viscous fluid flow. Therefore, to the zeroth order Chapman-Enskog method corresponds to the inviscid Euler equations.

The evaluation of $f^{(1)}$ is a bit more involved. For simplicity, we shall assume the scaled ES-BGK model for the collision term,

$$\frac{D\hat{f}}{D\hat{t}} + \hat{C}_k \frac{\partial \hat{f}}{\partial \hat{x}_k} + \hat{G}_k \frac{\partial \hat{f}}{\partial \hat{c}_k} = -\frac{1}{\mathrm{Kn}} \nu \left(\hat{f} - \hat{f}|_{\mathrm{ES}} \right) \tag{2.27}$$

Here, $\bar{C} = \sqrt{\frac{8}{\pi}\theta_0}$, L, $L/\bar{C}$, $\frac{\rho_0}{m}\bar{C}^{-3}$, ρ_0, and $\bar{C}^2/L$ have been used to nondimensionalize the microscopic velocity c_i, length x_i, average flow time t, distribution function f, density ρ, and the body force G_k. The Knudsen number Kn enters the ES-BGK equation (2.27) by choosing the mean free path $\lambda = \bar{C}/\nu$. We shall replace Kn by ϵ and drop the hats for better readability.

Furthermore, the material time derivative is also expanded as

$$\frac{D}{Dt} \equiv \frac{D^{(0)}}{Dt} + \epsilon \frac{D^{(1)}}{Dt} + \epsilon^2 \frac{D^{(2)}}{Dt} + ...$$

The conservation laws (2.10a-2.10c) must remain unchanged. Inserting these expansions into the conservation laws (2.10) and balancing terms with powers of ϵ, yields

$$\frac{D^{(0)}\rho}{Dt} + \rho \frac{\partial v_k}{\partial x_k} = 0, \;\; \frac{D^{(0)} v_i}{Dt} + \frac{1}{\rho}\frac{\partial p}{\partial x_i} = G_i, \; \frac{3}{2}\frac{D^{(0)}\theta}{Dt} + \theta \frac{\partial v_k}{\partial x_k} = 0,$$

and

$$\frac{D^{(\alpha)}\rho}{Dt} = 0, \;\; \frac{D^{(\alpha)} v_i}{Dt} + \frac{1}{\rho}\frac{\partial \sigma_{ik}^{(\alpha)}}{\partial x_k} = 0, \; \frac{3}{2}\frac{D^{(\alpha)}\theta}{Dt} + \frac{\sigma_{ik}^{(\alpha)}}{\rho}\frac{\partial v_i}{\partial x_k} + \frac{\partial q_k^{(\alpha)}}{\partial x_k} = 0 \;\; \forall \alpha > 0.$$

The operation $D^{(\alpha)}/Dt$ on the equilibrium distribution (2.24) is therefore well defined, as

$$\frac{D^{(\alpha)} f^{(0)}}{Dt} = \frac{\partial f^{(0)}}{\partial \rho}\frac{D^{(\alpha)}\rho}{Dt} + \frac{\partial f^{(0)}}{\partial v_i}\frac{D^{(\alpha)} v_i}{Dt} + \frac{\partial f^{(0)}}{\partial \theta}\frac{D^{(\alpha)}\theta}{Dt}.$$

If we substitute the assumed velocity distribution (2.23) into the dimensionless ES-BGK Boltzmann equation (2.27), and collect the terms up to the first order in ϵ, we

get

$$\frac{D^{(0)}f^{(0)}}{Dt} + C_k\frac{\partial f^{(0)}}{\partial x_k} + G_k\frac{\partial f^{(0)}}{\partial \hat{c}_k}$$
$$+\epsilon\left[\frac{D^{(1)}f^{(0)}}{Dt} + \frac{D^{(0)}f^{(1)}}{Dt} + C_k\frac{\partial f^{(1)}}{\partial x_k} + G_k\frac{\partial f^{(1)}}{\partial \hat{c}_k}\right] = -\nu\left(f^{(1)} - f|^{(1)}_{\rm ES}\right) - \epsilon\nu\left(f^{(2)} - f|^{(2)}_{\rm ES}\right), \tag{2.29}$$

where

$$f|_{\rm ES} = f|^{(0)}_{\rm ES} + \epsilon f|^{(1)}_{\rm ES} + \epsilon^2 f|^{(2)}_{\rm ES} + \ldots, \text{ and } f^{(0)}|_{\rm ES} = f^{(0)}.$$

To evaluate $f^{(1)}$, we consider the terms of order ϵ^0 in (2.29) to obtain

$$f^{(1)} = f_{\rm E}\frac{b}{2\rho\theta^2}\sigma^{(1)}_{ij}C_{\langle i}C_{j\rangle} - \frac{1}{\nu}\left(\frac{D^{(0)}f^{(0)}}{Dt} + C_k\frac{\partial f^{(0)}}{\partial x_k} + G_k\frac{\partial f^{(0)}}{\partial \hat{c}_k}\right),$$

where first term on the right hand side in the last equations is $f|^{(1)}_{\rm ES}$. By replacing the time derivatives and after some simplifications, the first order contribution to the distribution reads

$$f^{(1)} = f_{\rm E}\frac{b}{2\rho\theta^2}\sigma^{(1)}_{ij}C_{\langle i}C_{j\rangle} - f_{\rm E}\frac{1}{\nu}\left(\frac{C_{\langle i}C_{j\rangle}}{\theta}\frac{\partial v_{\langle i}}{\partial v_{j\rangle}} + \frac{C_k}{\theta}\left(\frac{C^2}{2\theta} - \frac{5}{2}\right)\frac{\partial\theta}{\partial x_k}\right). \tag{2.30}$$

Equation (2.30) gives first order contribution for the stress tensor and the heat flux vector, as

$$\sigma^{(1)}_{ij} = m\int C_{\langle i}C_{j\rangle}f^{(1)}d\mathbf{c} = -\frac{2}{1-b}\frac{p}{\nu}\frac{\partial v_{\langle i}}{\partial v_{j\rangle}}, \tag{2.31}$$

$$q^{(1)}_i = \frac{m}{2}\int C^2C_if^{(1)}d\mathbf{c} = -\frac{5}{2}\frac{p}{\nu}\frac{\partial\theta}{\partial x_i}\ . \tag{2.32}$$

The relations given by equations (2.31–2.32) are the constitutive equations of Navier-Stokes and Fourier, described earlier in equations (2.11–2.12), where

$$\mu = \frac{2}{1-b}\frac{p}{\nu} \text{ and } \kappa = \frac{5}{2}\frac{p}{\nu} \tag{2.33}$$

are viscosity and thermal conductivity, respectively. The correct value of the Prandtl number Pr is obtained for $b = -1/2$. Similarly, second and third order corrections lead to the Burnett and super-Burnett equations, respectively, see [97, 8] for the detailed procedure.

It has been shown in the literature that the Burnett and Super-Burnett equations are unstable in time [9]. Consequently, several modified forms of the Burnett equations have been suggested in the literature that are stable [128, 44, 88, 10, 11]. For example, Zhong et. al. suggested that super-Burnett order terms should be linearly added to the Burnett equations, to obtain the new equation set as the augmented Burnett equations [128]. However, this stabilization procedure is rather ad-hoc, and leads to an inconsistency with the tensorial structure in the general 3–dimensional case [97]. For a detailed review of the literature on Burnett-type equations, see Garcia Colin et. al. [31]. Even more, the Burnett–type equations, which contains third and higher–order derivatives, lack any systematic approach to derive boundary conditions.

2.6 DSMC method

The DSMC method is a numerical tool to solve the Boltzmann equation by using the statistical simulation of molecular processes [7]. In order to implement DSMC, the physical domain is divided into computational cells which are inhabited by simulating particles, where each simulating particle represents a large number of real gas molecules. The simulating particles move with different microscopic speed and collide; however, the motion and collision of the particles are assumed to be decoupled. The cells are further divided into sub-cells to facilitate the random selection of collision pairs. The time step Δt is chosen as a fraction of the mean collision time to ensure pure motion in the elapsed movement time. In the end, the macroscopic thermodynamic properties are sampled from molecular properties with in each cell. The DSMC solutions are proved to converge to the Boltzmann equation in the limit of infinite simulating particles in each computation cell [122].

The DSMC method is a very powerful numerical tool, which can simulate very complicated process including polyatomic gases, dense gases, and chemical reactions. However, due to their statistical nature, the DSMC method is prone to stochastic noise, in particular for microflows where the Mach number is very small [**?**]. Elimination of the noise requires long-time time averages in steady state problems, and averages over large ensembles in transient problems; this makes the method costly.

Recently, Hadjiconstaninou and co-workers developed a low-noise Monte-Carlo method which greatly reduces the noise and leads to a affordable speed of simulation for linear problems [43]. This method relies on consideration of the deviation from an equilibrium groundstate, and thus is equivalent to the linearized Boltzmann equation.

Chapter 3

Macroscopic moment equations

One method of approaching the Boltzmann equation is to consider its moment equations. The moment equations are obtained by taking the moments of the Boltzmann equation, however, this process generates an infinite hierarchy of equations [73, 97, 52]. In other words, the evolution equations for the moments of a given order will contain terms involving higher-order moments. Thus, to obtain a closed set of moment equations, one has to introduce some closure scheme for truncation of the moment hierarchy by representing higher order moments in terms of lower order moments.

The purpose of this chapter is to present the following closure schemes: the Grad closure [32], the regularized 13 (R13) closure [97, 102, 96, 98] and the phenomenological closure of the Gaussian 10 moment equations (R10) [56, 55, 73]. It will be shown in this chapter that the original R13 equations require different number of boundary conditions for the linear and nonlinear equations. In Section 3.2.3 we shall reformulate the original R13 equations using order of magnitude arguments and show that this new system is consistent for the boundary value problems in linear and nonlinear regimes. The modified R13 equations will be used in subsequent parts of this thesis.

3.1 Extended moment equations

In pronounced nonequilibrium situations, it is necessary to extend the set of macroscopic variables beyond the hydrodynamic variables (mass density ρ, temperature θ, velocity v_i), so as to include higher-order moments. These higher-order quantities typically include the full stress tensor σ_{ij}, the heat flux vector q_i, and other higher moments of the distribution function.

The governing equations for these extended macroscopic variables follows by multiplying the Boltzmann equation (2.1) with suitable polynomials in the microscopic velocity, $\Psi(\mathbf{c})$, and then integrating over the velocity space $\mathbf{c}$. For instance, in the thirteen-moment approximation, $\Psi_A = \{1,\ c_i,\ \frac{1}{2}C^2,\ C_{\langle i}C_{j\rangle},\ \frac{1}{2}C^2C_i\}$, corresponding to the moments $u_A = \{\rho,\ \rho v_i,\ \frac{3}{2}\rho\theta,\ \sigma_{ij},\ q_i\}$. The corresponding transport equations are the conservation laws (2.10) alongside the balance equations for the stress tensor σ_{ij} and the heat-flux vector q_i, as [97, 32, 73]

$$\frac{D\sigma_{ij}}{Dt} + \frac{4}{5}\frac{\partial q_{\langle i}}{\partial x_{j\rangle}} + 2\sigma_{k\langle i}\frac{\partial v_{j\rangle}}{\partial x_k} + \sigma_{ij}\frac{\partial v_k}{\partial x_k} + 2p\frac{\partial v_{\langle i}}{\partial x_{j\rangle}} + \frac{\partial u^0_{ijk}}{\partial x_k} = \mathcal{P}^0_{ij}, \tag{3.1}$$

and

$$\begin{aligned}\frac{Dq_i}{Dt} + \frac{5}{2}p\frac{\partial\theta}{\partial x_i} - \sigma_{ik}\frac{\partial\theta}{\partial x_k} - \theta\sigma_{ik}\frac{\partial \ln\rho}{\partial x_k} - \frac{\sigma_{ik}}{\rho}\frac{\partial\sigma_{kl}}{\partial x_l} - \frac{5}{2}\theta\frac{\partial\sigma_{ik}}{\partial x_k} + \frac{7}{5}q_k\frac{\partial v_i}{\partial x_k} \\ + \frac{7}{5}q_i\frac{\partial v_k}{\partial x_k} + \frac{2}{5}q_k\frac{\partial v_k}{\partial x_i} + u^0_{ikl}\frac{\partial v_k}{\partial x_l} + \frac{1}{2}\frac{\partial u^1_{ik}}{\partial x_k} + \frac{1}{6}\frac{\partial w^2}{\partial x_i} = \frac{1}{2}\mathcal{P}^1_i.\end{aligned} \tag{3.2}$$

However, the balance equations (3.1–3.2) do not form a closed set, since they contain additional higher moments

$$u^0_{ijk} = m\int C_{\langle i}C_jC_{k\rangle}f\,d\mathbf{c},\ u^1_{ij} = m\int C^2C_{\langle i}C_{j\rangle}f\,d\mathbf{c},\ w^2 = m\int C^4\left(f - f|_{\mathrm{E}}\right)d\mathbf{c}, \tag{3.3}$$

as well as the production terms

$$\mathcal{P}^0_{ij} = m\int C_{\langle i}C_{j\rangle}\mathcal{S}d\mathbf{c}, \text{ and } \quad \mathcal{P}^1_i = m\int C^2C_i\mathcal{S}d\mathbf{c}. \tag{3.4}$$

In order to close the system, constitutive relations are needed to express the fluxes u^0_{ijk}, u^1_{ik} and w^2 and collisional terms $\mathcal{P}^0_{ij}$ and $\mathcal{P}^1_i$ as functions of the variables u_A, and possibly their derivatives, thus forming a closed system.

The collisional terms can be computed without additional knowledge of the distribution function by assuming a gas of Maxwell molecules (2.18). In this case the production terms take the form [120]

$$\mathcal{P}^0_{ij} = -\frac{p}{\mu}\sigma_{ij}, \text{ and } \quad \mathcal{P}^1_i = -2\,\mathrm{Pr}\,\frac{p}{\mu}q_i.$$

3.1.1 Grad's 13–moment closure

H. Grad [32] expanded the distribution function in Hermite polynomials, the coefficients of which are linear combinations of the moments as

$$f_{\mathrm{G13}} = \frac{\rho}{m\sqrt{2\pi\theta}^3} \exp\left(-\frac{C^2}{2\theta}\right)\left(1 + \frac{1}{2\rho\theta^2} C_i C_j \sigma_{ij} - \frac{1}{\rho\theta^2}\left(1 - \frac{C^2}{5\theta}\right) C_k q_k\right). \tag{3.5}$$

This distribution reproduces the first 13 moments from their definitions in Eqs. (2.3–2.4). The constitutive equations for the unknown moments u^0_{ijk}, u^1_{ij} and w^2 are obtained using f_{G13} in (3.3), as

$$u^0_{ijk}|_{\mathrm{G13}} = m \int C_{\langle i} C_j C_{k\rangle} f_{\mathrm{G13}} d\mathbf{c} = 0, \tag{3.6a}$$

$$u^1_{ij}|_{\mathrm{G13}} = m \int C^2 C_{\langle i} C_{j\rangle} f_{\mathrm{G13}} d\mathbf{c} = 7\theta\sigma_{ij}, \tag{3.6b}$$

$$w^2|_{\mathrm{G13}} = m \int C^4 \left(f_{\mathrm{G13}} - f|_{\mathrm{E}}\right) d\mathbf{c} = 0\ . \tag{3.6c}$$

Eqs. (2.10a)−(2.10c), (3.1)−(3.2) and (3.6a)−(3.6c) form the well known 13–moment equations of Grad (G13 equations).

3.1.2 Grad's 26–moment closure

The next member of this moment hierarchy is the 26–moment system. Besides the thirteen variables $\{\rho,\ v_i,\ \theta,\ \sigma_{ij},\ q_i\}$, the 26–moment equations contain 13 additional variables u^0_{ijk}, u^1_{ij}, and w^2, i.e., the fluxes of σ_{ij} and q_i. For convenience, definitions of higher order moments are devised in deviation from Grad's 13–moment closure, where

$$\begin{array}{lll} m_{ijk} & = u^0_{ijk} - u^0_{ijk}|_{\mathrm{G13}} & = u^0_{ijk} \\ R_{ij} & = u^1_{ij} - u^1_{ij}|_{\mathrm{G13}} & = u^1_{ij} - 7\theta\sigma_{ij} \\ \Delta & = w^2 - w^2|_{\mathrm{G13}} & = w^2 \end{array} \tag{3.7}$$

so that Grad's 13–moment closure yields $m_{ijk} = R_{ij} = \Delta = 0$.

The balance equations for m_{ijk}, R_{ij} and Δ are obtained by multiplying the Boltzmann equation (2.1) with $C_{\langle i} C_j C_{k\rangle}$, $C^2 C_{\langle i} C_{j\rangle}$, and C^4, respectively, and then inte-

grating over the velocity space $\mathbf{c}$ [97]. After some simplification they read

$$\frac{Dm_{ijk}}{Dt} + 3\theta\frac{\partial\sigma_{\langle ij}}{\partial x_{k\rangle}} + 3\sigma_{\langle ij}\frac{\partial\theta}{\partial x_{k\rangle}} - 3\frac{\sigma_{\langle ij}}{\rho}\left(\frac{\partial p}{\partial x_{k\rangle}} + \frac{\partial\sigma_{k\rangle l}}{\partial x_l}\right) + \frac{12}{5}q_{\langle i}\frac{\partial v_j}{\partial x_{k\rangle}} + \frac{3}{7}\frac{\partial R_{\langle ij}}{\partial x_{k\rangle}} + 3m_{l\langle ij}\frac{\partial v_{k\rangle}}{\partial x_l} + m_{ijk}\frac{\partial v_l}{\partial x_l} + \frac{\partial u^0_{ijkl}}{\partial x_l} = \mathcal{P}^0_{ijk}, \quad (3.8)$$

$$\frac{DR_{ij}}{Dt} + \frac{2}{5}\frac{\partial u^2_{\langle i}}{\partial x_{j\rangle}} - \frac{28}{5}\theta\frac{\partial q_{\langle i}}{\partial x_{j\rangle}} - \frac{28}{5}\frac{q_{\langle i}}{\rho}\left(\frac{\partial p}{\partial x_{j\rangle}} + \frac{\partial\sigma_{j\rangle k}}{\partial x_k}\right) - \frac{14}{3}\frac{\sigma_{ij}}{\rho}\frac{\partial q_k}{\partial x_k} + 8\theta\sigma_{k\langle i}S_{j\rangle k} - \frac{14}{3}\frac{\sigma_{ij}\sigma_{kl}}{\rho}\frac{\partial v_k}{\partial x_l} - 7\theta\frac{\partial m_{ijk}}{\partial x_k} - 2\frac{m_{ijk}}{\rho}\left(\frac{\partial p}{\partial x_k} + \frac{\partial\sigma_{kl}}{\partial x_l}\right) + \frac{\partial u^1_{ijk}}{\partial x_k} + 2u^0_{ijkl}\frac{\partial v_k}{\partial x_l} + \frac{6}{7}R_{\langle ij}\frac{\partial v_{k\rangle}}{\partial x_k} + \frac{4}{5}R_{k\langle i}\frac{\partial v_k}{\partial x_{j\rangle}} + 2R_{k\langle i}\frac{\partial v_{j\rangle}}{\partial x_k} + R_{ij}\frac{\partial v_k}{\partial x_k} + \frac{14}{15}\Delta\frac{\partial v_{\langle i}}{\partial x_{j\rangle}} = \mathcal{P}^1_{ij} - 7\theta\mathcal{P}^0_{ij}, \quad (3.9)$$

and

$$\frac{D\Delta}{Dt} - 20\theta\frac{\partial q_k}{\partial x_k} + 8\theta\sigma_{kl}S_{kl} + 4R_{kl}\frac{\partial v_k}{\partial x_l} - 8\frac{q_k}{\rho}\left(\frac{\partial p}{\partial x_k} + \frac{\partial\sigma_{kl}}{\partial x_l}\right) + \frac{\partial u^2_k}{\partial x_k} + \frac{7}{3}\Delta\frac{\partial v_k}{\partial x_k} = \mathcal{P}^2, \quad (3.10)$$

where

$$S_{ij} = \frac{\partial v_{\langle i}}{\partial x_{j\rangle}} = \frac{1}{2}\left(\frac{\partial v_i}{\partial x_j} + \frac{\partial v_j}{\partial x_i}\right) - \frac{1}{3}\delta_{ij}\frac{\partial v_k}{\partial x_k}\ .$$

The moment equations for m_{ijk}, R_{ij}, and Δ contain the additional moments u^0_{ijkl}, u^1_{ijk}, and u^2_i, identified as

$$u^0_{ijkl} = m\int C_{\langle i}C_jC_kC_{l\rangle}fd\mathbf{c},\ u^1_{ijk} = m\int C^2C_{\langle i}C_jC_{k\rangle}fd\mathbf{c},\ u^2_i = m\int C^4C_ifd\mathbf{c}, \quad (3.11)$$

and the production terms

$$\mathcal{P}^0_{ijk} = m\int C_{\langle i}C_jC_{k\rangle}\mathcal{S}d\mathbf{c},\ \mathcal{P}^1_{ij} = m\int C^2C_{\langle i}C_{j\rangle}\mathcal{S}d\mathbf{c}, \text{ and } \quad \mathcal{P}^2 = m\int C^4\mathcal{S}d\mathbf{c}. \quad (3.12)$$

These unknowns, again, need be expressed with respect to the 26 variables, i.e., ρ, v_i, θ, σ_{ij}, q_i, m_{ijk}, R_{ij}, and Δ. The analogous Grad distribution for the for 26–

moment system is

$$f_{\mathrm{G26}} = f|_{\mathrm{E}} \left(1 + \frac{\sigma_{ij}}{2\rho\theta^2} C_i C_j - \frac{q_k}{\rho\theta^2}\left(1 - \frac{C^2}{5\theta}\right) C_k + \frac{\Delta}{8\rho\theta^2}\left(1 - \frac{2C^2}{3\theta} + \frac{C^4}{15\theta^2}\right) - \frac{R_{ij}}{4\rho\theta^3}\left(1 - \frac{C^2}{7\theta}\right) C_i C_j + \frac{m_{ijk}}{6\rho\theta^3} C_i C_j C_k\right). \quad (3.13)$$

This distribution reproduces the first 26 moments from their definitions (2.3), (2.4), and (3.3). Accordingly, the closure for the 26–moment case is

$$u^0_{ijkl}|_{\mathrm{G26}} = m \int C_{\langle i} C_j C_k C_{l\rangle} f_{\mathrm{G26}} d\mathbf{c} = 0, \quad (3.14a)$$

$$u^1_{ijk}|_{\mathrm{G26}} = m \int C^2 C_{\langle i} C_j C_{k\rangle} f_{\mathrm{G26}} d\mathbf{c} = 9\theta m_{ijk}, \quad (3.14b)$$

$$u^2_i|_{\mathrm{G26}} = m \int C^4 C_i f_{\mathrm{G26}} d\mathbf{c} = 28\theta q_i \ . \quad (3.14c)$$

The production terms in (3.4) and (3.12), for Maxwell molecules (MM), BGK and ES-BGK model can be found in [120, 97, 116], as

$$\mathcal{P}^0_{ij} = -\frac{p}{\mu}\sigma_{ij}, \quad (3.15a)$$

$$\mathcal{P}^1_i = -2\,\mathrm{Pr}\,\frac{p}{\mu} q_i, \quad (3.15b)$$

$$\mathcal{P}^2 = -\mathrm{Pr}_\Delta \frac{p}{\mu}\left(w^2 + \mathsf{B}_1 \frac{\sigma_{ij}\sigma_{ij}}{\rho}\right) \quad (3.15c)$$

$$\mathcal{P}^0_{ijk} = -\mathrm{Pr}_m \frac{p}{\mu} m_{ijk}, \quad (3.15d)$$

$$\mathcal{P}^1_{ij} = -\mathrm{Pr}_R \frac{p}{\mu}\left(u^1_{ij} + \mathsf{A}_1\theta\sigma_{ij} + \mathsf{A}_2 \frac{\sigma_{k\langle i}\sigma_{j\rangle k}}{\rho}\right). \quad (3.15e)$$

where the transport coefficients, Pr, Pr_R, Pr_M, Pr_Δ etc., can be found from Table 3.1.

Table 3.1: Transport coefficients for Maxwell molecules, BGK model and ES-BGK model.

	Pr	Pr_R	Pr_m	Pr_Δ	A_1	A_2	B_1
MM	$\frac{2}{3}$	$\frac{7}{6}$	$\frac{3}{2}$	$\frac{2}{3}$	-1	$\frac{4}{7}$	1
BGK	1	1	1	1	0	0	0
ES-BGK	$\frac{2}{3}$	$\frac{2}{3}$	$\frac{2}{3}$	$\frac{2}{3}$	$\frac{7}{2}$	$-\frac{1}{2}$	$-\frac{1}{2}$

Here Pr is the Prandtl number with $\mathrm{Pr} = \frac{2}{3}$ for Maxwell molecule and ES-BGK

model, Pr = 1 for the BGK model. Indeed, the ES-BGK model was constructed specifically to produce this value of the Prandtl number.

3.1.3 Larger Sets of Moment Equations

Similarly, the extension of the Grad–type equations can be constructed for higher number of moments, which provide a more refined description of nonequilibrium flows due to inclusion of more moments.

Grad's moment method offers no criterion on what moments are needed to describe a certain process with a desired accuracy. The merits of these moment equations are difficult to assess as such, since there is a no mathematical basis for choosing the number of moments. Various investigations on one-dimensional problems with large moment systems can be found, e.g., in [73, 116, 4], which indicate that moment theories converge eventually to the solutions of the Boltzmann solution if only enough moments are included. However, the number of moments might be huge, and the required computational effort to solve the system might even exceed that for kinetic approaches. Thus, no profit remains in solving large moment systems instead of the kinetic equation, since the purpose of using moment equations is to save computational time by avoiding the solution of the Boltzmann equation.

When considering a relatively low number of moments, the moment equations can be solved (numerically or analytically) much faster [108, 104, 106, 80, 12]. It will be shown that for moderate Knudsen numbers the 13–moments system offers a good agreement with solutions of the Boltzmann equation, e.g., those obtained from the DSMC method. At larger Knudsen numbers, when thirteen moments are insufficient, nevertheless their solutions can offer valuable insights into the process compared to the required computational cost.

The G13 equations, however, are hyperbolic in nature, yielding finite wave speeds and discontinuous sub-shock structures when the Mach number lies above $\mathrm{Ma} \gtrsim 1.65$. We also note that the G13 equations for non-linear problems lack suitable boundary conditions.

Over the last decades moment theories have been investigated in detail and further developed in various directions. Attempts to develop low order moment equations that obey the entropy law are found in [55, 65]. Torrilhon [112] proposed a procedure based on a Pearson–type–IV distribution to approximate the distribution function.

A regularization technique that overcomes some problems in Grad 13 closures have

been suggested in [97, 102, 96, 98] producing the regularized 13 equations (R13). The R13 equations yield infinite wave speeds, resulting in smooth shock structures, with good agreement to kinetic theory for Ma $\lesssim 3$ [117]. Furthermore, the R13 equations obey the H-theorem for the linear case [103], and are equipped with a complete set of boundary conditions [118].

3.2 Regularized Moment Equations

In the papers [102, 96, 98], Struchtrup and Torrilhon proposed a new procedure, the so-called *order of magnitude method,* to derive approximations to the Boltzmann equation from its infinite set of corresponding moment equations. Next, we shall describe the order of magnitude method and demonstrate how it can be used to formally derive the R13 equations.

3.2.1 Order of magnitude method

In the order of magnitude method, the first step is to determine the leading order of all moments by means of a Chapman–Enskog expansion [96, 98]. The next step is to re-define moments by linear combinations of moments in order to have the minimum number of moments at a given order. Then the moment equations are rewritten in these new moments, and steps one and two are repeated until the rescaled moment equations are obtained to a desired accuracy. Finally, the rescaled moment equations are systematically reduced by cancelling terms of higher order. To better understand how the process works, we shall look at the step-by-step derivation of the regularized systems, up to third order.

For the proper scaling procedure dimensionless variables and equations are used. In order to non-dimensionalize the moment equations and related variables, we introduce suitable reference quantities. Let x_0, ρ_0, θ_0, μ_0 be reference length, density, temperature, and viscosity, respectively. As a result of non-dimensionalization the Knudsen number appears in the governing equations, as $\mu_0 = \mathrm{Kn}\rho_0\sqrt{\theta_0}L$. We shall replace Kn by ϵ to determine the order of terms in the equations. In the end, we shall set $\epsilon = 1$, which is equivalent to re-inserting the dimensions into the corresponding dimensionless equations.

The first step is to determine the leading order of the moments appearing in moment equations (2.10, 3.1, 3.2, and 3.8–3.10), by means of a Chapman–Enskog

expansion (see Section 2.5).

The equilibrium variables ρ, v_i, θ are considered to be of order $\mathcal{O}(1)$, and are not expanded. The non-equilibrium moments are expanded in terms of ϵ, i.e.,

$$\sigma_{ij} = \sigma_{ij}^{(0)} + \epsilon\,\sigma_{ij}^{(1)} + \cdots, \qquad q_i = q_i^{(0)} + \epsilon\, q_i^{(1)} + \cdots, \tag{3.16a}$$

$$m_{ijk} = m_{ijk}^{(0)} + \epsilon\, m_{ijk}^{(1)} + \cdots, \qquad R_{ij} = R_{ij}^{(0)} + \epsilon\, R_{ij}^{(0)} + \cdots \tag{3.16b}$$

$$\Delta = \Delta^{(0)} + \epsilon\,\Delta^{(1)} + \cdots, \text{ and so on.} \tag{3.16c}$$

and replaced back in Eqs. (2.10, 3.1, 3.2, 3.8–3.10). When terms with equal powers in ϵ are equated, we get

$$\sigma_{ij}^{(0)} = q_i^{(0)} = 0, \tag{3.17}$$

which means that the leading orders for σ_{ij} and q_i are at least $\mathcal{O}(\epsilon)$. Similarly, we find that the other moments, i.e., m_{ijk}, R_{ij}, Δ, u^0_{ijkl}, u^1_{ijk}, and u^2_k are also of order ϵ or higher. Therefore, to zeroth order accuracy we recover the Euler equations.

In the next iteration, by comparing the terms of $\mathcal{O}(\epsilon)$, we obtain

$$\sigma_{ij}^{(1)} = -2\mu \frac{\partial v_{\langle i}}{\partial x_{j\rangle}}, \qquad q_i^{(1)} = -\frac{1}{\mathrm{Pr}}\frac{5}{2}\mu\frac{\partial \theta}{\partial x_i} \text{ and} \tag{3.18a}$$

$$m_{ijk}^{(1)} = R_{ij}^{(1)} = \Delta^{(1)} = 0. \tag{3.18b}$$

Furthermore, CE expansion of the moment equation for u^2_k, as [97], yields

$$u_k^{2(1)} = -70\theta\frac{1}{\mathrm{Pr}}\mu\frac{\partial\theta}{\partial x_i}.$$

At first order, all first order terms in the conservation laws are considered, and thus the complete conservation laws (2.10) must be considered together with the leading order expressions for stress and heat flux, i.e., the leading terms in (3.18). This gives, again, the Navier–Stokes and Fourier equations,

$$\sigma_{ij}^{\mathrm{NSF}} = \sigma_{ij}^{(1)} = -2\mu\frac{\partial v_{\langle i}}{\partial x_{j\rangle}} \tag{3.19a}$$

$$q_i^{\mathrm{NSF}} = q_i^{(1)} = -\frac{1}{\mathrm{Pr}}\frac{5}{2}\mu\frac{\partial\theta}{\partial x_i}. \tag{3.19b}$$

We note that in (3.18), to first order m_{ijk}, R_{ij}, and Δ vanish. Indeed, the moments in (3.7) were constructed specifically to yield this result.

In the second step, the knowledge of the order of magnitude of all variables is used to construct a new set of variables which has the minimum number of variables at the first order, i.e., we redefine the moments $u_i^2 = \Omega_i + 28\theta q_i$, so that

$$\Omega_i = \epsilon^2\,\Omega_i^{(2)} + \epsilon^3\,\Omega_i^{(3)} + \cdots \tag{3.20}$$

Note that $\Omega_i^{(1)} = u_i^{2(1)} - 28\theta q_i^{(1)} = 0$.

Equations (3.8)–(3.10), after the proper order is assigned to the various terms using (3.16) and (3.20), read

$$\epsilon\left[3\theta\frac{\partial\sigma_{\langle ij}}{\partial x_{k\rangle}} - 3\frac{\sigma_{\langle ij}}{\rho}\frac{\partial p}{\partial x_{k\rangle}} + 3\sigma_{\langle ij}\frac{\partial\theta}{\partial x_{k\rangle}} + \frac{12}{5}q_{\langle i}\frac{\partial v_j}{\partial x_{k\rangle}}\right] + \\ + \epsilon^2\,[...] = \epsilon\left[-\mathrm{Pr}_m\frac{p}{\mu}m_{ijk}\right], \tag{3.21}$$

$$\epsilon\left[\frac{28}{5}\theta\frac{\partial q_{\langle i}}{\partial x_{j\rangle}} - \frac{28}{5}\frac{q_{\langle i}}{\rho}\frac{\partial p}{\partial x_{j\rangle}} + \frac{56}{5}q_{\langle i}\frac{\partial\theta}{\partial x_{j\rangle}} + 8\theta\sigma_{k\langle i}S_{j\rangle k}\right] + \\ + \epsilon^2\,[...] = \epsilon\left[-\mathrm{Pr}_R\frac{p}{\mu}\left(R_{ij} + \mathsf{A}_2\frac{\sigma_{k\langle i}\sigma_{j\rangle k}}{\rho}\right)\right], \tag{3.22}$$

and

$$\epsilon\left[8\theta\frac{\partial q_k}{\partial x_k} - 8\frac{q_k}{\rho}\frac{\partial p}{\partial x_k} + 28q_k\frac{\partial\theta}{\partial x_k} + 8\theta\sigma_{kl}S_{kl}\right] + \\ + \epsilon^2\,[...] = \epsilon\left[-\mathrm{Pr}_\Delta\frac{p}{\mu}\left(\Delta + \mathsf{B}_1\frac{\sigma_{ij}\sigma_{ij}}{\rho}\right)\right]. \tag{3.23}$$

As before, we need to find the leading order expressions for the moments m_{ijk}, R_{ij}, and Δ, which we determine from the Eqs. (3.21–3.23). By comparing the terms of $\mathcal{O}(\epsilon)$, we get

$$m_{ijk}^{(2)} = -\frac{3}{\mathrm{Pr}_m}\frac{\mu}{p}\left(\theta\frac{\partial\sigma_{\langle ij}}{\partial x_{k\rangle}} - \frac{\sigma_{\langle ij}}{\rho}\frac{\partial p}{\partial x_{k\rangle}} + \sigma_{\langle ij}\frac{\partial\theta}{\partial x_{k\rangle}} + \frac{4}{5}q_{\langle i}\frac{\partial v_j}{\partial x_{k\rangle}}\right), \tag{3.24a}$$

$$R_{ij}^{(2)} = -\mathsf{A}_2\frac{\sigma_{k\langle i}\sigma_{j\rangle k}}{\rho} - \frac{28}{5\mathrm{Pr}_R}\frac{\mu}{p}\left(\theta\frac{\partial q_{\langle i}}{\partial x_{j\rangle}} - \frac{q_{\langle i}}{\rho}\frac{\partial p}{\partial x_{j\rangle}} + 2q_{\langle i}\frac{\partial\theta}{\partial x_{j\rangle}} + \frac{10}{7}\theta\sigma_{k\langle i}S_{j\rangle k}\right), \tag{3.24b}$$

$$\Delta^{(2)} = -\mathsf{B}_1\frac{\sigma_{ij}\sigma_{ij}}{\rho} - \frac{8}{\mathrm{Pr}_\Delta}\frac{\mu}{p}\left(\theta\frac{\partial q_k}{\partial x_k} - \frac{q_k}{\rho}\frac{\partial p}{\partial x_k} + \frac{7}{2}q_k\frac{\partial\theta}{\partial x_k} + \theta\sigma_{kl}S_{kl}\right), \tag{3.24c}$$

where, again, we used the abbreviation $S_{ij} = \frac{\partial v_{\langle i}}{\partial x_{j\rangle}}$.

We shall not go beyond this level of the order of magnitude method, and we shall only consider the leading terms in m_{ijk}, R_{ij} and Δ, which are given by (3.24). The resulting equations are the R13 equations, summarized as follows:

3.2.2 R13–moment equations

■ **Conservation laws**:

$$\frac{D\rho}{Dt} + \rho\frac{\partial v_k}{\partial x_k} = 0 \tag{3.25a}$$

$$\frac{Dv_i}{Dt} + \frac{1}{\rho}\frac{\partial(p\delta_{ik} + \sigma_{ik})}{\partial x_k} = G_i \tag{3.25b}$$

$$\frac{3}{2}\frac{D\theta}{Dt} + \theta\frac{\partial v_k}{\partial x_k} + \frac{\sigma_{ik}}{\rho}\frac{\partial v_i}{\partial x_k} + \frac{1}{\rho}\frac{\partial q_k}{\partial x_k} = 0 \tag{3.25c}$$

■ **The equations for pressure deviator and the heat flux vector**:

$$\frac{D\sigma_{ij}}{Dt} + \frac{4}{5}\frac{\partial q_{\langle i}}{\partial x_{j\rangle}} + 2\sigma_{k\langle i}\frac{\partial v_{j\rangle}}{\partial x_k} + \sigma_{ij}\frac{\partial v_k}{\partial x_k} + 2p\frac{\partial v_{\langle i}}{\partial x_{j\rangle}} + \frac{\partial m_{ijk}}{\partial x_k} = -\frac{p}{\mu}\sigma_{ij} \tag{3.26}$$

$$\begin{aligned}\frac{Dq_i}{Dt} + \frac{5}{2}p\frac{\partial\theta}{\partial x_i} + \frac{5}{2}\sigma_{ik}\frac{\partial\theta}{\partial x_k} - \theta\sigma_{ik}\frac{\partial \ln\rho}{\partial x_k} + \theta\frac{\partial\sigma_{ik}}{\partial x_k} - \frac{\sigma_{ik}}{\rho}\frac{\partial\sigma_{kl}}{\partial x_l} + \frac{7}{5}q_k\frac{\partial v_i}{\partial x_k} \\ + \frac{7}{5}q_i\frac{\partial v_k}{\partial x_k} + \frac{2}{5}q_k\frac{\partial v_k}{\partial x_i} + m_{ikl}\frac{\partial v_k}{\partial x_l} + \frac{1}{2}\frac{\partial R_{ik}}{\partial x_k} + \frac{1}{6}\frac{\partial\Delta}{\partial x_i} = -\Pr\frac{p}{\mu}q_i\end{aligned} \tag{3.27}$$

■ **R13 constitutive laws for m_{ijk}, R_{ij}, and Δ:**

$$m_{ijk} = -\frac{3}{\mathrm{Pr}_m}\frac{\mu}{p}\left(\theta\frac{\partial\sigma_{\langle ij}}{\partial x_{k\rangle}} - \frac{\sigma_{\langle ij}}{\rho}\frac{\partial p}{\partial x_{k\rangle}} + \sigma_{\langle ij}\frac{\partial\theta}{\partial x_{k\rangle}} + \frac{4}{5}q_{\langle i}\frac{\partial v_j}{\partial x_{k\rangle}}\right) \tag{3.28a}$$

$$R_{ij} = -\mathsf{A}_2\frac{\sigma_{k\langle i}\sigma_{j\rangle k}}{\rho} - \frac{28}{5\mathrm{Pr}_R}\frac{\mu}{p}\left(\theta\frac{\partial q_{\langle i}}{\partial x_{j\rangle}} - \frac{q_{\langle i}}{\rho}\frac{\partial p}{\partial x_{j\rangle}} + 2q_{\langle i}\frac{\partial\theta}{\partial x_{j\rangle}} + \frac{10}{7}\theta\sigma_{k\langle i}S_{j\rangle k}\right) \tag{3.28b}$$

$$\Delta = -\mathsf{B}_1\frac{\sigma_{ij}\sigma_{ij}}{\rho} - \frac{8}{\mathrm{Pr}_\Delta}\frac{\mu}{p}\left(\theta\frac{\partial q_k}{\partial x_k} - \frac{q_k}{\rho}\frac{\partial p}{\partial x_k} + \frac{7}{2}q_k\frac{\partial\theta}{\partial x_k} + \theta\sigma_{kl}S_{kl}\right) \tag{3.28c}$$

The R13 equations give smooth shock structures for high Mach numbers [117], and they are stable [102, 96]. Therefore, the order of magnitude method yields a marked improvement over the original Chapman-Enskog and Grad methods.

A Chapman-Enskog expansion of the R13–moment equations (3.2.2) shows that the terms added to the Grad 13 moment equation are of super-Burnett order [97], thus the R13 equations are of third order in the Chapman-Enskog sense. Furthermore, for the linearized R13 equations, an entropy inequality can be found [103], which also includes thermodynamically consistent boundary conditions. Just recently, a set of nonlinear R13 moment equations with entropy was suggested by Torrilhon, see [114] for details. These equations differ from those above in the non-linear terms for m_{ijk}, R_{ij}, Δ.

While the model developed here is for 13 moments, all ideas of the order of magnitude method can be applied to larger moment numbers. However, as we proceed with the treatment towards higher orders of magnitude, the equations become more involved; Gu and Emerson have developed and solved the regularized 26–moment equations [35, 36].

3.2.3 Coherence of Boundary Conditions

A difficult issue in the theory of extended transport equations is the problem to prescribe boundary conditions for higher moments, which are not controlled in experiments.

For the original R13 equations (3.2.2), it turns out that the non-linear equations require more boundary conditions than the linearized equations [118, 80]. To resolve this inconsistency in the R13 system, we shall use order of magnitude arguments to rewrite the non-linear part of the R13 constitutive equations (3.28) such that the third order accuracy is maintained, but linear and nonlinear equations require the

same boundary conditions.

For better understanding of this issue, let us consider the R13 moment equations for a two dimensional steady state process, where all variables depend only on $\{x, y\}$. In this setting, we have 17 independent variables in the R13 equations, namely

$$U = \{\rho, v_x, v_y, \theta, q_x, q_y, \sigma_{xx}, \sigma_{xy}, \sigma_{yy}, R_{xx}, R_{xy}, R_{yy}, m_{xxx}, m_{xyy}, m_{xxy}, m_{yyy}, \Delta\},$$

The R13 system (3.2.2), for a two dimensional steady state processes can be written in matrix form as

$$\mathcal{A}(U)\frac{\partial U}{\partial x} + \mathcal{B}(U)\frac{\partial U}{\partial y} + P(U)U = 0 \tag{3.29}$$

where $\mathcal{A}(U)$ and $\mathcal{B}(U)$ are the coefficient matrices in x and y–directions, respectively. The matrix $P(U)$ is the production matrix. The matrices $\mathcal{A}(U)$, $\mathcal{B}(U)$ and $P(U)$ are presented in Appendix (A).

For convenience let us consider the $x-$direction only, however, a similar argument will hold for an arbitrary direction. If $\mathcal{N}$ is the dimension of the system (3.29) and the matrix $\mathcal{A}(U)$ has a zero eigenvalue with multiplicity α, then we must describe $\mathcal{N}-\alpha$ boundary conditions [118]. Moreover, the normal convective flux vanishes, i.e., $v_x = 0$, at a point infinitesimally close to a non-permeable wall, therefore one has to take into account the eigenvalues of the matrix $\mathcal{A}(U : v_x = 0)$.

A detailed inspection of the coefficient matrices $\mathcal{A}(U)$ and $\mathcal{B}(U)$ shows that $\mathcal{A}(U : v_x = 0)$ and $\mathcal{B}(U : v_y = 0)$ possess a zero eigenvalue with multiplicity $\alpha = 3$, thus one needs to prescribe $17 - 3 = 14$ conditions altogether. On the other hand, if a small deviation from equilibrium is considered and the matrix $\mathcal{A}(U)$ is linearized with respect to the equilibrium state U_0, where

$$U_0 = \left[\rho_0, \quad 0, \quad 0, \quad \theta_0, \quad \mathbf{0} \in \mathbb{R}^{13}\right],$$

then the linearized matrix $\mathcal{A}(U_0)$ has a zero eigenvalue with multiplicity 5, thus the integration requires $17 - 5 = 12$ boundary conditions for each direction. Thus, it seems that a different number of boundary conditions is required for the linearized and the fully non-linear equations, which leads to spurious oscillations in numerical solutions of non-linear equations [67].

The hypothesis of coherence of boundary conditions [118] states that, "*The transition from a process in the linear regime to a non-linear process should not change the number of boundary conditions".* That is, describing a non-linear process with

R13 equations should not require more boundary conditions than in the linear case. To avoid this inconsistency, we reformulate the constitutive relations in Eqs. (3.30), without altering the third order asymptotic accuracy of the equations.

Using (3.19), we can rewrite the R13 constitutive equations (3.28), as

$$m_{ijk} = \frac{6}{5}\frac{1}{\mathrm{Pr}_m}\left(\mathrm{Pr}\,\frac{\sigma_{\langle ij}q^{\mathrm{NSF}}_{k\rangle}}{p} + \frac{q_{\langle i}\sigma^{\mathrm{NSF}}_{jk\rangle}}{p}\right) - \frac{3\mu}{\mathrm{Pr}_m}\theta\frac{\partial\left(\sigma_{\langle ij}/p\right)}{\partial x_{k\rangle}}, \tag{3.30a}$$

$$R_{ij} = -\mathsf{A}_2\frac{\sigma_{k\langle i}\sigma_{j\rangle k}}{\rho} + \frac{28}{5\mathrm{Pr}_R}\left(\frac{5}{7}\frac{\sigma_{k\langle i}\sigma^{\mathrm{NSF}}_{j\rangle k}}{\rho} + \frac{4\,\mathrm{Pr}}{5}\frac{q_{\langle i}q^{\mathrm{NSF}}_{j\rangle}}{p}\right) - \frac{28\mu}{5\mathrm{Pr}_R}\theta\frac{\partial\left(q_{\langle i}/p\right)}{\partial x_{j\rangle}}, \tag{3.30b}$$

$$\Delta = -\mathsf{B}_1\frac{\sigma_{ij}\sigma_{ij}}{\rho} + \frac{8}{\mathrm{Pr}_\Delta}\left(\frac{1}{2}\frac{\sigma_{kl}\sigma^{\mathrm{NSF}}_{kl}}{\rho} + \frac{7\,\mathrm{Pr}}{5}\frac{q_kq^{\mathrm{NSF}}_k}{p}\right) - \frac{8\mu}{\mathrm{Pr}_\Delta}\theta\frac{\partial\left(q_k/p\right)}{\partial x_k}. \tag{3.30c}$$

Now, we can reformulate the constitutive relations in Eqs. (3.30) by replacing the Navier-Stokes stress and the Fourier heat flux in (3.30) by the actual stress and heat flux, to obtain

$$m_{ijk} = \frac{6}{5}\frac{(\mathrm{Pr}+1)}{\mathrm{Pr}_m}\frac{\sigma_{\langle ij}q_{k\rangle}}{p} - \frac{3\mu}{\mathrm{Pr}_m}\theta\frac{\partial\left(\sigma_{\langle ij}/p\right)}{\partial x_{k\rangle}}, \tag{3.31a}$$

$$R_{ij} = \left(\frac{4}{\mathrm{Pr}_R} - \mathsf{A}_2\right)\frac{\sigma_{k\langle i}\sigma_{j\rangle k}}{\rho} + \frac{112}{25}\frac{\mathrm{Pr}}{\mathrm{Pr}_R}\frac{q_{\langle i}q_{j\rangle}}{p} - \frac{28\mu}{5\mathrm{Pr}_R}\theta\frac{\partial\left(q_{\langle i}/p\right)}{\partial x_{j\rangle}}, \tag{3.31b}$$

$$\Delta = \left(\frac{4}{\mathrm{Pr}_\Delta} - \mathsf{B}_1\right)\frac{\sigma_{ij}\sigma_{ij}}{\rho} + \frac{56}{5}\frac{\mathrm{Pr}}{\mathrm{Pr}_\Delta}\frac{q_kq_k}{p} - \frac{8\mu}{\mathrm{Pr}_\Delta}\theta\frac{\partial\left(q_k/p\right)}{\partial x_k}. \tag{3.31c}$$

Note that the changed terms appear as a multiples of stress, σ_{ij}, and heat flux, q_i, which both are of $\mathcal{O}(\mathrm{Kn})$. Therefore, the transformation introduces an asymptotic error of $\mathcal{O}(\mathrm{Kn}^3)$ in the expressions for Δ, R_{ij}, m_{ijk}, and the overall asymptotic accuracy of the R13 system remains at $\mathcal{O}(\mathrm{Kn}^3)$.

Replacing the original constitutive equations (3.30) by the new equations (3.31) results in new matrices $\mathcal{A}(U)$ and $\mathcal{B}(U)$, which, as is easy to show, possess a zero eigenvalue with multiplicity $\alpha = 5$ in the linear and non-linear cases. Thus one needs only 12 boundary conditions as in the linearized case. Note that the linear terms is R13 equations are not affected by this transformation, since only non-linear terms are changed. The new matrices $\mathcal{A}(U)$ and $\mathcal{B}(U)$, for Maxwell molecules, are presented in Appendix A.

A similar transformation was suggested in [118] where pressure gradients in (3.30)

were replaced by means of the steady state momentum balance. The transformation shown above has the following advantages: 1. No pressure gradients are replaced; consequently, this transformation is justified even in presence of high pressure gradients or strong body forces. 2. The transformation rule is obtained for the full three dimensional R13 equations rather than for a simplified geometry as in [118]; therefore the transformation can be performed for arbitrary geometries and dimensions.

The transformed system, i.e., (3.25), (3.26), (3.27) along with (3.31) will be used from now on.

3.3 R10–moment equations

Levermore [55] derived a hierarchy of moment equations based on the assumption that the approximate form for the distribution function corresponds to that of the maximum-entropy distribution [26]. Levermore's hierarchy shares all features with Rational Extended Thermodynamics [73].

If only the first 10 moments (ρ, v_i, θ, and σ_{ij}) are considered, the maximum-entropy distribution leads to the Gaussian distribution function, given as [56]

$$f_{\text{Gauss}} = \frac{\rho}{m\sqrt{\det\left(2\pi\Theta\right)}} \exp\left(-\frac{1}{2}\Theta_{ij}^{-1} C_i C_j\right) \tag{3.32}$$

where Θ_{ij} is the temperature tensor given by $\Theta_{ij} = p_{ij}/\rho$; p_{ij} is the pressure tensor (2.4). The temperature tensor can be written as

$$\Theta_{ij} = \theta_{ij} + \theta\delta_{ij} \tag{3.33}$$

where θ_{ij} is the deviatoric part of the temperature tensor, i.e., $\theta_{ij} = \Theta_{\langle ij\rangle} = \sigma_{ij}/\rho$, and $\theta = \frac{1}{3}\Theta_{kk}$.

The evolution equation for θ_{ij} is obtained from equations (3.25a) and (3.26), as

$$\frac{D\theta_{ij}}{Dt} + 2\Theta_{k\langle i}\frac{\partial v_{j\rangle}}{\partial x_k} + \frac{4}{5}\frac{1}{\rho}\frac{\partial q_{\langle i}}{\partial x_{j\rangle}} + \frac{1}{\rho}\frac{\partial m_{ijk}}{\partial x_k} = -\frac{p}{\mu}\theta_{ij}. \tag{3.34}$$

The set of equations (3.25), (3.34) form Levermore's 10–moment equations. For closure, constitutive relations for q_i and m_{ijk} are required. The Gaussian closure for

the 10–moment case is

$$q_i|_{\text{Gauss}} = \frac{m}{2}\int C^2 C_i\, f_{\text{Gauss}}\, d\mathbf{c} = 0 \tag{3.35a}$$

$$m_{ijk}|_{\text{Gauss}} = m\int C_{\langle i} C_j C_{k\rangle}\, f_{\text{Gauss}}\, d\mathbf{c} = 0 \tag{3.35b}$$

The resulting equations are globally hyperbolic and have an entropy law [56, 57, 26]. The usefulness of the Levermore's 10-moment equations is, however, limited as the heat flux vector vanishes identically for the Gaussian closure (3.35). McDonald and Groth [65, 66] derived the regularization of Levermore's 10–moment equations using the Chapman-Enskog (CE) expansion of the ES–BGK model, which gives non-zero expressions for q_i and m_{ijk}.

In the next subsection, we shall describe the derivation of the regularized 10–moment equations (R10), however, our approach is founded on the framework of phenomenological linear irreversible thermodynamics [23, 48, 71]. The proposed approach is more general, in the sense that it is independent of the collision model. It is shown that both techniques yield identical results if the ES-BGK model is considered for the computation of transport coefficients.

3.3.1 Phenomenological theory

Now, the required constitutive relations for q_i, m_{ijk} will be constructed such that they ensure non-negative entropy production. The nonequilibrium entropy s not only depends on the equilibrium variables, ρ and θ, but in addition on the nonequilibrium variable θ_{ij}. The Θ_{ij} dependence of entropy is taken from the Gaussian distribution function (3.32), as [56]

$$s = -\frac{k_B}{\mathrm{R}}\int f \ln\frac{f}{y} d\mathbf{c} = \ln\left(\frac{\sqrt{\det(\Theta)}}{\rho}\right) + s_0. \tag{3.36}$$

This stands in agreement with the equilibrium entropy (2.17), since $\theta_{ij} = 0$ in equilibrium.

From (3.36), we get the partial derivatives of the entropy with respect to the density ρ, and the temperature tensor Θ_{ij}, as

$$\frac{\partial s}{\partial \rho} = -\frac{1}{\rho}, \text{ and } \quad \frac{\partial s}{\partial \Theta_{ij}} = \frac{1}{2}\Theta^{-1}_{ij}.$$

This allows us to write the entropy law (second law of thermodynamics) for the 10–moment equations, as

$$\rho\frac{Ds}{Dt} = -\frac{D\rho}{Dt} + \frac{1}{2}\rho\Theta_{ij}^{-1}\frac{D\theta}{Dt}\delta_{ij} + \frac{1}{2}\rho\Theta_{ij}^{-1}\frac{D\theta_{ij}}{Dt}. \tag{3.37}$$

After introducing the continuity equation (3.25a), energy equation (3.25c), and the equation for the deviatoric part of the temperature tensor (3.34) into equation (3.37), we obtain

$$\begin{aligned}\rho\frac{Ds}{Dt} = \rho\Theta_{ij}^{-1}\left(\frac{1}{3}\theta_{ij}\frac{\partial v_k}{\partial x_k} - \frac{1}{3}\theta_{rk}\frac{\partial v_r}{\partial x_k}\delta_{ij} - \theta_{k\langle i}\frac{\partial v_{j\rangle}}{\partial x_k} - \theta\frac{\partial v_{\langle i}}{\partial x_{j\rangle}}\right)\\ - \frac{1}{3}\Theta_{ij}^{-1}\delta_{ij}\frac{\partial q_k}{\partial x_k} - \frac{2}{5}\Theta_{ij}^{-1}\frac{\partial q_{\langle i}}{\partial x_{j\rangle}} - \frac{1}{2}\Theta_{ij}^{-1}\frac{\partial m_{ijk}}{\partial x_k} - \frac{1}{2}\frac{p}{\mu}\rho\Theta_{ij}^{-1}\theta_{ij}.\end{aligned} \tag{3.38}$$

In the last equation, all terms containing the velocity gradients cancel, therefore, (3.38) takes the form

$$\rho\frac{Ds}{Dt} = -\frac{1}{3}\Theta_{ij}^{-1}\delta_{ij}\frac{\partial q_k}{\partial x_k} - \frac{2}{5}\Theta_{ij}^{-1}\frac{\partial q_{\langle i}}{\partial x_{j\rangle}} - \frac{1}{2}\Theta_{ij}^{-1}\frac{\partial m_{ijk}}{\partial x_k} - \frac{1}{2}\frac{p}{\mu}\rho\Theta_{ij}^{-1}\theta_{ij}. \tag{3.39}$$

In the next step, we use the product rule of differentiation on the right hand side of the equation (3.39) to obtain

$$\begin{aligned}\rho\frac{Ds}{Dt} + \frac{1}{3}\frac{\partial\Theta_{ij}^{-1}\delta_{ij}q_k}{\partial x_k} + \frac{2}{5}\frac{\partial\Theta_{ij}^{-1}q_{\langle i}}{\partial x_{j\rangle}} + \frac{1}{2}\frac{\partial\Theta_{ij}^{-1}m_{ijk}}{\partial x_k} =\\ \frac{1}{3}q_k\frac{\partial\Theta_{ij}^{-1}\delta_{ij}}{\partial x_k} + \frac{2}{5}q_{\langle i}\frac{\partial\Theta_{ij}^{-1}}{\partial x_{j\rangle}} + \frac{1}{2}m_{ijk}\frac{\partial\Theta_{ij}^{-1}}{\partial x_k} - \frac{1}{2}\frac{p}{\mu}\rho\Theta_{ij}^{-1}\theta_{ij}.\end{aligned}$$

Comparison of the last equation with the familiar form of the second law [23]

$$\rho\frac{Ds}{Dt} + \frac{\partial\Psi_k}{\partial x_k} = \Sigma\ ,$$

identifies the entropy flux, Ψ_k, and the entropy production per unit volume, Σ, as

$$\Psi_k = \frac{1}{5}q_k\Theta_{rr}^{-1} + \frac{2}{5}q_r\Theta_{rk}^{-1} + \frac{1}{2}\Theta_{ij}^{-1}m_{ijk} \text{ and} \tag{3.40}$$

$$\Sigma = \frac{1}{3}q_k\frac{\partial\Theta_{rr}^{-1}}{\partial x_k} + \frac{2}{5}q_{\langle i}\frac{\partial\Theta_{ij}^{-1}}{\partial x_{j\rangle}} + \frac{1}{2}m_{ijk}\frac{\partial\Theta_{ij}^{-1}}{\partial x_k} - \frac{1}{2}\frac{p}{\mu}\rho\Theta_{ij}^{-1}\theta_{ij}. \tag{3.41}$$

By simplifying the right hand side of equation (3.41), and using the identity $\partial a_{ij}^{-1}/\partial x = -a_{i\alpha}^{-1}\left(\partial a_{\alpha\beta}/\partial x\right)a_{\beta j}^{-1}$, the entropy production Σ in (3.41) can be written as

$$\Sigma = -\frac{1}{5}\left(q_k\delta_{ij}+q_i\delta_{jk}+q_j\delta_{ik}\right)\Theta_{i\alpha}^{-1}\Theta_{j\beta}^{-1}\Theta_{k\gamma}^{-1}\left(\Theta_{r\gamma}\frac{\partial\Theta_{\alpha\beta}}{\partial x_r}\right) - \frac{1}{2}m_{ijk}\Theta_{i\alpha}^{-1}\Theta_{j\beta}^{-1}\Theta_{k\gamma}^{-1}\left(\Theta_{r\gamma}\frac{\partial\Theta_{\alpha\beta}}{\partial x_r}\right) - \frac{1}{2}\frac{p}{\mu}\rho\Theta_{ij}^{-1}\theta_{ij}. \quad (3.42)$$

A close inspection of (3.42) shows that the entropy production Σ has three contributions, due to heat flux q_i (first term in (3.42)), m_{ijk} (second term in (3.42)) and due to relaxation term (third term in (3.42)). Note that the relaxation, i.e., $-\frac{1}{2}\frac{p}{\mu}\rho\Theta_{ij}^{-1}\theta_{ij} \geq 0$ for all (ρ, θ, $\mu \geq 0$), since one can verify that

$$-\Theta_{ij}^{-1}\theta_{ij} = \theta\frac{\left(\sqrt{\frac{\lambda_1}{\lambda_2}}-\sqrt{\frac{\lambda_2}{\lambda_1}}\right)^2+\left(\sqrt{\frac{\lambda_3}{\lambda_2}}-\sqrt{\frac{\lambda_2}{\lambda_3}}\right)^2+\left(\sqrt{\frac{\lambda_3}{\lambda_1}}-\sqrt{\frac{\lambda_1}{\lambda_3}}\right)^2}{(\lambda_1+\lambda_2+\lambda_3)} \geq 0,$$

where $\lambda_i\,(>0)$ are the eigenvalues of the positive definite temperature tensor Θ.

The second law states that the entropy production must be non-negative, i.e., $\Sigma \geq 0$. The non-negativity of the entropy production imposes the following constitutive equations upon the heat flux vector q_k, and the third order tensor m_{ijk}

$$q_i = -\gamma_q\left(\frac{5}{2}\Theta_{im}\frac{\partial\theta}{\partial x_m}+\Theta_{mr}\frac{\partial\theta_{ir}}{\partial x_m}\right), \text{ and } \quad m_{ijk} = -\gamma_m\Theta_{r\langle i}\frac{\partial\theta_{jk\rangle}}{\partial x_r}. \quad (3.43)$$

where γ_q and γ_m are arbitrary non-negative coefficients that can depend on scalar variables, e.g., ρ, θ, and the invariants of the θ_{ij} tensor. The phenomenological coefficients γ_q and γ_m can assume a wide range of values, hence can be used for fitting to experiments, or other models in kinetic theory.

To yield the proper form of the Fourier law in the linear case, one would set $\gamma_q = \frac{\mu}{\theta}\frac{1}{\mathrm{Pr}}$. Similarly, the coefficient γ_m can be set to $2\frac{\mu}{\theta}$ to give agreement to Maxwell molecules, or to $3\frac{\mu}{\theta}$ for the ES-BGK model. Altogether, it makes sense to assume that the coefficients are proportional to mean free time or viscosity.

Note that the contribution of m_{ijk} in the conservation laws is of third–order, so that they vanish in second order theories (i.e., for the Grad 13 equations and the Burnett equations) [97]. Therefore, to a second order accuracy, we can choose $\gamma_m = 0$. Throughout this thesis, the second order R10 equations are used, i.e., we choose the phenomenological coefficients from the Table 3.2.

Table 3.2: Phenomenological transport coefficients for Maxwell molecules, BGK model and ES-BGK model.

	MM	BGK	ES-BGK
γ_q	$\frac{\mu}{\theta}\frac{1}{\mathrm{Pr}}$	$\frac{\mu}{\theta}$	$\frac{\mu}{\theta}\frac{1}{\mathrm{Pr}}$
γ_m	0	0	0

Using definitions, $\Theta_{ij} = \theta\delta_{ij} + \theta_{ij}$ and $\theta_{ij} = \sigma_{ij}/\rho$, and after shuffling of terms, we can rewrite (3.43) as

$$q_i = \underbrace{-\frac{1}{\mathrm{Pr}}\frac{5}{2}\mu\frac{\partial\theta}{\partial x_i}}_{\text{Fourier heat-flux}} \underbrace{-\frac{1}{\mathrm{Pr}}\mu\frac{\partial\left(\sigma_{ik}/\rho\right)}{\partial x_k}}_{\text{Stress induced heat-flux}} - \frac{\mu}{p}\frac{1}{\mathrm{Pr}}\left(\frac{5}{2}\sigma_{ik}\frac{\partial\theta}{\partial x_k} + \sigma_{mk}\frac{\partial\left(\sigma_{ik}/\rho\right)}{\partial x_m}\right). \quad (3.44)$$

A comparison of (3.44) and (3.19) shows that the Fourier heat flux, as indicated by the underlined term, is included in the R10 equations. In addition, the R10 heat flux also contains stress induced contributions. Later in Chapter (7), we shall show that stress can cause heat to flow from cold to hot. Another advantage of the regularized 10–moment equations is that they are similar to the NSF equations, in nature. The numerical solution of the R10—moment equation can therefore be computed using the standard techniques devised for the Navier-Stokes-Fourier equations [13, 65].

The maximum entropy distribution ensures the global hyperbolicity of the moment equations [57, 72, 55, 73], whereas Grad type equations can occasionally lose their hyperbolicity—especially for high-speed applications. Loss of hyperbolicity of Grad type equations can induce serious computational and numerical drawbacks. Thus, in strong non-equilibrium cases the globally hyperbolic equations, such as Levermore's 10–, 14–, 35–moment equations can be used [13, 65, 5]. Nevertheless, in MEMS application merit for any extended transport model is its capability to describe non-equilibrium effects.

Chapter 4

Boundary Conditions

The interaction of the gas particles with walls is a very complex process, which depends on the microscopic details of the surface and the gas particles. In most physical calculations an adequate description of the gas flows can be obtained by using simplified microscopic wall-gas interaction models which correlate the distribution functions of the incoming and reflected molecules. Maxwell [64] provided a simple microscopic approximate description of the wall-gas interaction, typically known as Maxwell accommodation model. In this chapter we shall develop the wall boundary conditions for the R13 equations by using the Maxwell accommodation model and isotropic scattering model. Unlike the Maxwell accommodation model [118], the use of isotropic scattering model allows us to study adiabatic-rough surfaces. We shall also derive a set of phenomenological boundary conditions for the linearized R13 equations through second law of thermodynamics. The resulting boundary conditions contain free parameters that can be adjusted to measurements or other theories. With properly chosen coefficients, the boundary conditions agree with those from the Maxwell model.

4.1 Maxwell accommodation model

Maxwell suggested that the gas particles interact with the wall only in two ways, *specular reflection* and *diffusive reflection*. On a specularly reflecting wall, the tangential velocity of the incident particle remains unchanged, while the normal component of its velocity changes sign. On the other hand, on a diffusive wall, the incident particles equilibrate themselves with the wall instantaneously, and bounce back into the

gas with a Maxwellian distribution, see Fig. 4.1(a). The distribution of the reflected molecules is determined by the wall temperature and velocity.

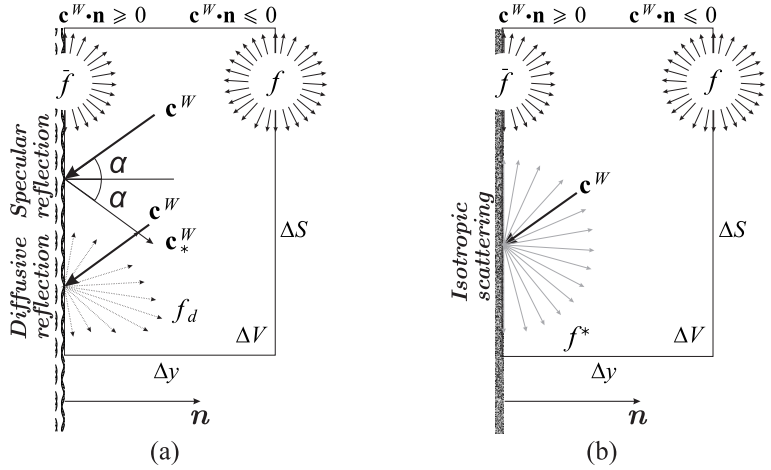

Figure 4.1: Interaction of the gas particles with a surface (a) Maxwell accommodation model (b) Isotropic scattering model.

The fraction of molecules that equilibrate with the wall is given by the accommodation coefficient, χ. The rest of the molecules are specularly reflected. The dimensionless coefficient χ describes the wall characteristics and must be given or measured. From this approximation, Maxwell deduced the slip velocity boundary conditions.

In deriving boundary conditions for macroscopic equations, we consider a wall with temperature θ_W and velocity v_k^W. In a reference frame where the wall is at rest (hereafter, denoted by the superscript 'W'), the microscopic velocity c_i, and the peculiar velocity C_i of the gas particles, are

$$c_i^W = c_i - v_i^W, \quad C_i = c_i - v_i = c_i^W - \mathcal{V}_i, \tag{4.1}$$

respectively, where $\mathcal{V}_i = v_i - v_i^W$ is the slip velocity.

Let $f(c_i^W, x_i, t)$ be the distribution function of the gas in proximity of the wall. In order to simplify the following discussion, it is useful to present f as a function of tangential velocity, $c_i^W - c_k^W n_k n_i$, and normal velocity, $c_k^W n_k$, i.e., $f = f(c_k^W n_k, c_i^W - c_k^W n_k n_i, x_i, t)$. Here, n_k denotes the normal vector to the wall pointing into the gas, see Fig. 4.1(a).

The collisions between particles and wall change the distribution function, so that

in proximity of a wall, the distribution of post-collision particles will be different from f. Consequently, when only specular reflections are considered, the distribution of the particles reflected from the wall is given as

$$f_r = f(-c_k^W n_k, c_i^W - c_k^W n_k n_i, x_i, t). \tag{4.2}$$

In diffusive reflection, the reflected particles are distributed according to the Maxwellian distribution, i.e.,

$$f_d = \frac{\rho^W}{\sqrt{2\pi\theta^W}^3} \exp\left(-\frac{c_W^2}{2\theta^W}\right), \tag{4.3}$$

where ρ^W is the density of the diffused molecules which must be chosen such that there is no accumulation of particles on the surface.

For the Maxwell accommodation model, the distribution function of the particles leaving the surface ($c_k^W n_k \geq 0$) is obtained by combining (4.2) and (4.3) as

$$f^+ = \chi f_d + (1-\chi) f_r, \tag{4.4}$$

so that the distribution directly at the wall $\bar{f}$ according the Maxwell accommodation model is

$$\bar{f} = \begin{cases} f & , c_k^W n_k \leq 0 \\ f^+ & , c_k^W n_k \geq 0. \end{cases} \tag{4.5}$$

The density of the diffused molecules, ρ^W, is obtained from (4.5), using the impermeability condition,

$$v_n^W n_k = \int c_k^W n_k \bar{f} d\mathbf{c} = 0. \tag{4.6}$$

Once $\bar{f}$ is known, details of the gas-surface interaction are precisely described.

4.1.1 Macroscopic boundary conditions

To study the boundary conditions on the macroscopic level, let us consider an infinitesimal volume element adjacent to the wall, see Fig. 4.1(a). For simplicity, we set Cartesian coordinates where $\mathbf{n} = \{0, 1, 0\}$ and the infinitesimal volume element is $\Delta V = \Delta S \Delta y$. The generalization to arbitrary walls is straightforward.

Integrating (2.7) over the volume ΔV and taking $\Delta y \to 0$, we get [97, 118]

$$m \int \Psi_A c_y^W f d\mathbf{c}^W = m \int \Psi_A c_y^W \bar{f} d\mathbf{c}^W. \tag{4.7}$$

with $\Psi_A\left(\mathbf{c}^W\right)$ being the set of velocity weights considered at the wall.

Equation (4.7) is the central equation to obtain boundary conditions for the moments, which relates the normal flux of a moment $u_A = m\int \Psi_A f d\mathbf{c}^W$ to its normal flux on the boundary. Substitution of $\bar{f}$ from (4.5) into (4.7) and decomposing the integral for incoming and outgoing particles yields

$$m\int \Psi_A dc_y^W f d\mathbf{c}^W = m\int\int\int_{c_y^W\le 0} \Psi_A c_y^W f d\mathbf{c}^W + m\int\int\int_{c_y^W\ge 0} \Psi_A c_y^W f^+ d\mathbf{c}^W. \quad (4.8)$$

In the context of the R13 moment equations (or the Grad 26 moment equations), it is assumed that the gas distribution function f in (4.8) is adequately described by the Grad 26 moments distribution function (3.13). Indeed, for any velocity function Ψ_A, equation (4.8) yields a relation between moments u_A in the gas and the wall properties θ_W, v_i^W. However, the question remains—for physical and mathematical consistency between the moment equations and their boundary conditions—which Ψ_A should be considered.

4.1.2 Grad's hypothesis and boundary conditions for R13 moment equations

According to Grad's discussion [32, 33], in order to get meaningful boundary conditions, the velocity function Ψ_A should be even in the normal component of the particle velocity $c_k^W n_k = c_y^W$, i.e., we can only take

$$\Psi_A = 1,\ c_x^W,\ c_z^W,\ c_k^W c_k^W,\ c_x^W c_x^W,\ c_y^W c_y^W,\ c_x^W c_z^W,\ c_k^W c_k^W c_x^W,\ c_k^W c_k^W c_z^W \ldots, \text{ and so on.} \quad (4.9)$$

This list is further restricted by the number of moments in the equations.

In particular, for $\Psi_A = 1$, when (4.8) is solved for $v_y = 0$, a relation for ρ^W is obtained as

$$\rho_W\sqrt{\theta\,\theta_W} = p + \frac{1}{2}\sigma_{yy} - \frac{1}{120}\frac{\Delta}{\theta} - \frac{1}{28}\frac{R_{yy}}{\theta} = \mathcal{P}. \quad (4.10)$$

Similarly, the boundary conditions for moments σ_{xy}, σ_{yz}, q_y, m_{xxy}, m_{yyy}, q_y, m_{xyz}, R_{xy}, and R_{yz} are obtained by choosing the appropriate Ψ_A in (4.9).

Here, for briefness, we shall only consider a two–dimensional process in the x–y plane, where the non-equilibrium quantities in $z-$direction (e.g., $\sigma_{yz}, q_z, m_{xyz},\ R_{yz}, R_{xz}$) vanish and their boundary conditions produce identities. This leaves us with only 6

elements in Ψ_A, as

$$\Psi_A = \left\{1,\, c_x^W,\; c_k^W c_k^W,\, c_x^W c_x^W,\, c_y^W c_y^W,\, c_k^W c_k^W c_x^W\right\}. \tag{4.11}$$

Let us recall, from equation (4.1),

$$c_i^W = C_i + \mathcal{V}_i, \text{ and} \quad c_k^W n_k = C_k n_k$$

where $\mathcal{V}_i = v_i - v_i^W$ denotes the slip velocity, which is parallel to the wall, i.e., $\mathcal{V}_k n_k = 0$. Using these transformations, we can rewrite (4.8) as

$$m\int\int\int_{C_y\le 0} \Psi_A C_y f_{\mathrm{G26}} d\mathbf{C} + m\int\int\int_{C_y\ge 0} \Psi_A C_y f^+ d\mathbf{C} = 0\ . \tag{4.12}$$

Equation (4.12)—when evaluated using (4.11) and (4.10), after some simplifications—produces six boundary conditions for the R13 equations, as [118, 12]

$$v_y = 0 \tag{4.13a}$$

$$\sigma_{xy} = \frac{-\chi}{2-\chi}\sqrt{\frac{2}{\pi\theta}}\left(\mathcal{P}\mathcal{V}_x + \frac{1}{5}q_x + \frac{1}{2}m_{xyy}\right) \tag{4.13b}$$

$$q_y = \frac{\chi}{2-\chi}\sqrt{\frac{2}{\pi\theta}}\left(\frac{1}{2}\mathcal{P}\mathcal{V}_x^2 - 2\mathcal{P}\mathcal{T} - \frac{1}{2}\theta\sigma_{yy} - \frac{1}{15}\Delta - \frac{5}{28}R_{yy}\right) \tag{4.13c}$$

$$m_{yyy} = \frac{-\chi}{2-\chi}\sqrt{\frac{2}{\pi\theta}}\left(\frac{3}{5}\mathcal{P}\mathcal{V}_x^2 - \frac{2}{5}\mathcal{P}\mathcal{T} + \frac{7}{5}\theta\sigma_{yy} - \frac{1}{75}\Delta + \frac{1}{14}R_{yy}\right) \tag{4.13d}$$

$$m_{xxy} = \frac{\chi}{2-\chi}\sqrt{\frac{2}{\pi\theta}}\left(\frac{4}{5}\mathcal{P}\mathcal{V}_x^2 - \frac{1}{5}\mathcal{P}\mathcal{T} - \theta\sigma_{xx} + \frac{\theta}{5}\sigma_{yy} - \frac{\Delta}{150} - \frac{R_{xx}}{14}\right) \tag{4.13e}$$

$$R_{xy} = \frac{-\chi}{2-\chi}\sqrt{\frac{2}{\pi\theta}}\left(\mathcal{P}\mathcal{V}_x^3 - \mathcal{P}\mathcal{V}_x\theta - 6\mathcal{P}\mathcal{T}\mathcal{V}_x + \frac{11}{5}\theta q_x + \frac{1}{2}\theta m_{xyy}\right) \tag{4.13f}$$

where $\mathcal{T} = \theta - \theta^w$ denotes the temperature jump and $\mathcal{P}$ is given in (4.10). Let us recall from our discussion in Section (3.2.3), that the R13 equations require six boundary conditions on each wall; the generalization of (4.13) to arbitrary walls is straightforward.

4.1.3 Boundary Conditions for NSF and R10 Equations

If a 13-moment set is considered (so that the gas distribution function f in (4.8) is described by the Grad 13 distribution function (3.5))— following the same procedure

as above—one can obtain the explicit expressions for slip velocity $\mathcal{V}_x$, and temperature jump $\mathcal{T}$, as

$$\mathcal{V}_x = -\frac{2-\chi}{\chi}\sqrt{\frac{\pi\theta}{2}}\,\frac{\sigma_{xy}}{\mathcal{P}} - \frac{1}{5}\frac{q_x}{\mathcal{P}}, \tag{4.14}$$

$$\mathcal{T} = -\frac{2-\chi}{\chi}\sqrt{\frac{\pi\theta}{2}}\,\frac{q_y}{2\mathcal{P}} + \frac{1}{4}\mathcal{V}_x^2 - \frac{1}{4}\frac{\theta}{\mathcal{P}}\sigma_{yy}, \tag{4.15}$$

along with

$$v_y = 0,$$

where $\mathcal{P} = p + \frac{1}{2}\sigma_{yy}$.

To get jump and slip boundary conditions for the NSF equations, both the stress and the heat flux in (4.14–4.15) must be replaced by the NSF laws (3.19). This gives first order slip and jump boundary conditions for the NSF equations, as

$$\mathcal{V}_x = \mu\frac{2-\chi}{\chi}\sqrt{\frac{\pi\theta}{2}}\,\frac{1}{\mathcal{P}}\frac{\partial v_x}{\partial y} + \mu\frac{1}{2\,\mathrm{Pr}}\frac{1}{\mathcal{P}}\frac{\partial\theta}{\partial x}, \tag{4.16}$$

$$\mathcal{T} = \mu\frac{5}{4\,\mathrm{Pr}}\frac{2-\chi}{\chi}\sqrt{\frac{\pi\theta}{2}}\,\frac{1}{\mathcal{P}}\frac{\partial\theta}{\partial y} + \frac{1}{4}\mathcal{V}_y^2 + \frac{1}{6}\mu\frac{\theta}{\mathcal{P}}\left(2\frac{\partial v_y}{\partial y} - \frac{\partial v_x}{\partial x}\right). \tag{4.17}$$

The R10 equations require the conditions (4.14–4.15) where the heat flux must be replaced by the R10 constitutive law (3.43).

According to (4.16), a slip in velocity results from a velocity gradient along the wall, or due to a temperature gradient along the wall, the latter is known as thermal creep or thermal transpiration [89, 76, 17, 46]. Similarly from (4.17), a temperature jump occurs due to the temperature and velocity gradients.

In extended theories (4.13), however, the slip velocity $\mathcal{V}_x$ results from the shear stress σ_{xy}, the tangential heat flux q_x and m_{xyy}. Similarly, temperature jump $\mathcal{T}$ occurs due to the normal heat flux q_y, normal stress σ_{xy} and higher order moments R_{yy} and Δ; the term $\mathcal{P}\mathcal{V}_x^2$ appearing in (4.13c) represents viscous heating. Later, we shall show that m_{ijk}, R_{ij} and Δ add Knudsen layer corrections to the slip and jump conditions.

4.1.4 Second order jump–slip boundary conditions for NSF

Studies [89, 16] based on kinetic theory indicate that NSF equations show significant deviations with models based on first-order boundary conditions. Therefore, several authors have proposed second-order boundary conditions, hoping to extend

the validity of the slip flow regime to higher Knudsen numbers [89, 39].

The R13 boundary conditions presented in (4.10)–(4.13c) include additional higher order moments. Therefore, they can be used to derive high-order slip and jump boundary conditions for the NSF equations [104, 12].

We find a second-order jump and slip boundary conditions for NSF by combining the equations (4.10)–(4.13c) and (3.31) and replacing the stress tensor and heat flux vector using second order contributions given by the Burnett equations [97]. Considering the leading linear terms only, for Maxwell molecules, we obtain

$$\sigma_{xy}^{\mathrm{NSF}} = \frac{-\chi}{2-\chi}\sqrt{\frac{2}{\pi\theta}}\left(\mathcal{P}\mathcal{V}_x + \frac{1}{5}q_x^{\mathrm{NSF}} + \frac{m_{xyy}^{(2)}}{2} + \right.$$
$$\left. \frac{1}{5}\frac{\mu^2}{\rho}\left(\frac{45}{16}\frac{\partial^2 v_x}{\partial x_k \partial x_k} - \frac{13}{4}\frac{\partial^2 v_k}{\partial x \partial x_k}\right)\right) - \frac{1}{18}\frac{R_{xy}^{(2)}}{\theta}, \quad (4.18)$$

$$q_y^{\mathrm{NSF}} = \frac{-\chi}{2-\chi}\sqrt{\frac{2}{\pi\theta}}\left(2\mathcal{P}\mathcal{T} - \frac{1}{2}\mathcal{P}\mathcal{V}_x^2 + \frac{1}{2}\theta\sigma_{yy}^{\mathrm{NSF}} + \frac{1}{15}\Delta^{(2)}\right.$$
$$\left. + \frac{13}{63}R_{yy}^{(2)}\right) - \frac{\mu^2}{\rho}\left(\frac{45}{16}\frac{\partial^2 v_y}{\partial x_k \partial x_k} - \frac{13}{4}\frac{\partial^2 v_k}{\partial y \partial x_k}\right), \quad (4.19)$$

where the second order corrections, $m_{ijk}^{(2)}$, $\Delta^{(2)}$ and $R_{ij}^{(2)}$ result from the linear contributions of R13 constitutive relations (3.31) by replacing stress σ_{ij} and heat flux q_i with their Navier-Stokes-Fourier expressions,

$$\Delta^{(2)} = -12\frac{\mu}{\rho}\frac{\partial q_k^{\mathrm{NSF}}}{\partial x_k}, \quad R_{ij}^{(2)} = -\frac{24}{5}\frac{\mu}{\rho}\frac{\partial q_{\langle i}^{\mathrm{NSF}}}{\partial x_{j\rangle}}, \text{ and } \quad m_{ijk}^{(2)} = -2\frac{\mu}{\rho}\frac{\partial \sigma_{\langle ij}^{\mathrm{NSF}}}{\partial x_{k\rangle}}. \quad (4.20)$$

The forms of the equations (4.18–4.19) are the same as that of Sone's boundary conditions for flat interfaces [89], only that the R13 equations yield different coefficients than those given by Sone [89] for a hard-sphere gas and BKW model.

It can be shown that for Poiseuille flow, the second order slip and jump boundary conditions yield marked improvement over the first order boundary conditions, in particula,r the prediction of the Knudsen minimum and the overall flow rate [104].

4.2 Isotropic scattering model

In last section, we saw how Maxwell accommodation model can produce macroscopic boundary conditions for moment equations. Let us recall that the Maxwell accommodation model describes the exchange of momentum and energy between gas particles and the wall. In a specular reflection ($\chi = 0$), the incident molecules do not exchange energy with the wall surface, thus the wall behaves like an adiabatic and frictionless surface. In a diffusive reflection ($\chi = 1$), the interaction between gas particles and the surface is very strong, and energy and momentum of the reflected particle are completely uncorrelated to the pre-collision state.

The Maxwell accommodation model, however, cannot describe adiabatic walls with friction. The simplest model to describe such surface is the isotropic scattering model [53, 101], where the particles leaving the surface are isotropically distributed while the magnitude of their velocities is the same as in the pre-collision state, see Fig. 4.1(b). Since the collision with the surface does not change the energy of the particles, the surface behaves as an adiabatic wall, while exchanging momentum with the gas, so that there is friction on the wall.

Accordingly, in (4.5), the distribution function $\bar{f}$ of the particles at the wall according to the isotropic scattering model is

$$\bar{f} = \begin{cases} f & , \quad c_k^W n_k \leq 0 \\ f^* & , \quad c_k^W n_k \geq 0, \end{cases} \tag{4.21}$$

where f^* is an isotropic function of microscopic velocity c_i^W, i.e.,

$$f^*(c_i^W, x_i, t) = f^*(|c^W|, x_i, t).$$

It will be convenient to introduce spherical coordinates $\left\{|c^W|,\ \vartheta,\ \phi\right\}$ for the velocity space, i.e.,

$$c_i^W = |c^W| \upsilon_i = |c^W| \left\{ \sin(\vartheta)\cos(\phi),\quad \sin(\vartheta)\sin(\phi),\quad \cos(\vartheta) \right\}_i$$

where $|c^W| \in [0,\ \infty]$, $\vartheta \in [0,\ \pi]$, $\phi \in [0,\ 2\pi]$, and the solid angle $d\Omega = \sin(\vartheta)\, d\vartheta d\phi$; the direction vector of the particle is denoted as υ_i.

As there is no accumulation of molecules at the wall, so that from (4.6) and (4.21),

we obtain

$$f^*(|c^W|) = \frac{\int_{\pi/2}^{\pi}\int_0^{2\pi} \upsilon_k n_k f \sin(\vartheta)\, d\phi d\vartheta}{\int_{\pi/2}^{\pi}\int_0^{2\pi} \upsilon_k n_k \sin(\vartheta)\, d\phi d\vartheta}. \tag{4.22}$$

For the 26–moment theory, one has to replace $f = f|_{\mathrm{G26}}$ in the equation above. As it turns out, the above equation can not be evaluated explicitly, therefore, we shall be content with linear cases[1].

For flow with small deviations from the equilibrium state, linearization of (4.22) can be performed with respect to a reference equilibrium state, given by ρ_0, θ_0. After linearization, evaluation of (4.12) using (4.22), gives explicit expressions for the boundary conditions as

$$\begin{aligned}
v_y &= 0 && \text{(4.23a)}\\
\sigma_{xy} &= -\sqrt{\frac{2}{\pi\theta_0}}\left(p_0\mathcal{V}_x + \frac{1}{5}q_x + \frac{1}{2}m_{xyy}\right) && \text{(4.23b)}\\
q_y &= 0 && \text{(4.23c)}\\
m_{yyy} &= -\sqrt{\frac{2}{\pi\theta_0}}\left(\frac{3R_{yy}}{28} + \theta_0\frac{3\sigma_{yy}}{2}\right) && \text{(4.23d)}\\
m_{xxy} &= \sqrt{\frac{2}{\pi\theta_0}}\left(-\frac{R_{xx}}{14} + \frac{R_{yy}}{56} - \theta_0\sigma_{xx} + \frac{\theta_0\sigma_{yy}}{4}\right) && \text{(4.23e)}\\
R_{xy} &= -\sqrt{\frac{2}{\pi\theta_0}}\left(-\mathcal{V}_x p_0 + \frac{11}{5}q_x + \frac{1}{2}m_{xyy}\right)\theta_0, && \text{(4.23f)}
\end{aligned}$$

where $\mathcal{V}_x = v_x - v_x^W$, again, is the slip velocity. Note from the equation (4.23c), this surface behaves as an adiabatic wall, while exchanging shear stress with the gas as $\sigma_{xy} \neq 0$, see equation (4.23b).

The corresponding slip boundary conditions for the NSF equations can be obtained from the boundary conditions for the R13 equations (4.23a–4.23c), as

$$\begin{aligned}
v_y &= 0, && \text{(4.24a)}\\
\sigma_{xy}^{\mathrm{NSF}} &= -\sqrt{\frac{2}{\pi\theta_0}}\left(p_0\mathcal{V}_x + \frac{1}{5}q_x^{\mathrm{NSF}}\right), && \text{(4.24b)}\\
q_y &= 0, && \text{(4.24c)}
\end{aligned}$$

where $\sigma_{ij}^{\mathrm{NSF}}$ and q_i^{NSF} in (4.24) are given by the NSF constitutive relations (3.19).

It is interesting to note that in the linear limit (4.13), for $\chi = 1$ and $\mathcal{T} =$

[1]The nonlinear case is discussed in [**?**].

$-\frac{1}{4}\left(\frac{\sigma_{yy}}{\rho_0} - \frac{2}{15}\frac{\Delta}{p_0} - \frac{5}{14}\frac{R_{yy}}{p_0}\right)$, reduce to (4.23). Therefore, in the Maxwell accommodation model, the temperature θ^W of the distribution function for reflecting particles can be adapted locally to yield zero heat flux.

Wang et al. [123] introduced the inverse temperature sampling method to model the heat flux at the wall, and demonstrated that this method can correctly specify the heat flux at the surface, however, this procedure adds further to the computational cost of the DSMC method. Very recently, we implemented the isotropic scattering model in a DSMC scheme; the results with this model will be presented in Section (7.4).

Other scattering kernels have also been proposed over the years. Cercignani and Lampis [18] proposed a scattering kernel which has two accommodation coefficients to account for anisotropic properties of surfaces. Lord [58] further extended this model to account for the anisotropic behavior of polyatomic molecules on surfaces. These kernels are, however, yet to be applied in an extended hydrodynamic framework.

4.3 Open boundary conditions for R13 moment equations

Open systems can exchange both mass and energy with arbitrarily large surroundings. It is, however, obvious that in order to conduct actual computations, we have to somehow restrict the original unbounded domain. That is, to introduce external boundaries and to further consider only a finite domain. This is done by introducing open boundary conditions; the word *open* emphasizing here that systems can exchange both mass and energy with an outside system.

Naturally, we would like these boundary conditions to be well behaved, and more importantly, a proper number of boundary conditions must be specified. Prescribing too many or too few boundary conditions prevents the existence and uniqueness of the solution and dramatically affects the convergence of the numerical schemes.

To find proper open boundary conditions for the non-linear R13 equations is a difficult topic and unfortunately, no conclusive answer it yet available. Well-posed boundary conditions for Euler and Navier-Stokes equations have been investigated by Strikwerda [94], Gustafson and Sundstrom [38], Halpern [41], among others. Here, we shall make use of the concepts developed in these studies and—by taking advantage of the resemblance of (G13 and) R13 equations to compressible (Euler and) Navier-

Stokes equations—discuss some issues related to the open (inflow, outflow or far-field) boundary conditions for the R13 equations.

4.3.1 Some remarks on the number of boundary conditions

The R13 equations introduced in the previous chapter can be written in conservative form as [111]

$$\frac{\partial U}{\partial t} + \frac{\partial F_k}{\partial x_k} + \frac{\partial F_k^{\nu}}{\partial x_k} = \mathcal{S}, \tag{4.25}$$

where U denotes the variables, F_k denotes the convective fluxes, F_k^{ν} denotes the diffusive fluxes and $\mathcal{S}$ denotes the source vector consisting of the production terms. Here we restrict ourself to a one dimensional process in $y\,(= x_2)$ direction. The explicit definitions of U, F_y, F_y^{ν} vectors—for Maxwell molecules— are presented in Appendix B.

In (4.25), U, F_k and $\mathcal{S}$ are explicit functions of 9 *primitive variables*

$$\wp = \{\rho,\, v_1,\, v_2,\, \theta,\, \sigma_{11},\, \sigma_{22},\, \sigma_{12},\, q_1,\, q_2\}\,,$$

whereas, F_k^{ν} depends on $\wp$ and $\nabla\wp$, i.e., $F_k^{\nu} = F_k^{\nu}\,(\wp,\, \nabla\wp)$. Equation (4.25) can also be rewritten using matrix operators as

$$\frac{\partial \wp}{\partial t} = A^2 \frac{\partial \wp}{\partial y} + B^{22} \frac{\partial^2 \wp}{\partial y^2} + \mathcal{B}, \tag{4.26}$$

where A^2 denotes the advection matrices and B^{22} denotes the diffusion matrices.

For flow with small deviations from the equilibrium state, linearization of (4.26) can be performed with respect to a constant state, given by $\rho = \rho_0$, $\theta = \theta_0$, and $v_y = v_0$, so that A^2 and B^{22} become constant coefficient matrices, as

$$A^2 = \begin{pmatrix} A_{11}^2 \in \mathbb{R}^{4\times4} & A_{12}^2 \in \mathbb{R}^{4\times5} \\ A_{21}^2 \in \mathbb{R}^{5\times4} & A_{22}^2 \in \mathbb{R}^{5\times5} \end{pmatrix},\; B^{22} = \begin{pmatrix} 0 \in \mathbb{R}^{4\times4} & 0 \in \mathbb{R}^{4\times5} \\ 0 \in \mathbb{R}^{5\times4} & B_{22}^{22} \in \mathbb{R}^{5\times5} \end{pmatrix}$$

We make the following observations:

1. All eigenvalues of A^2 are real and their eigen-space is complete. The eigenvalues of A^2 are

$$\lambda_i = -v_0,\; -v_0,\; -v_0, -v_0 \pm 0.81298\sqrt{\theta_0}, -v_0 \pm 1.1832\sqrt{\theta_0}, -v_0 \pm 2.1305\sqrt{\theta_0}.$$

2. Matrix B^{22} is rank-deficient, with rank 5 and all eigenvalues of matrix B^{22} are non-negative.

3. System (4.26) is symmetrizable.

4. Sub-systems $\frac{\partial \wp^1}{\partial t} = A^2_{11}\frac{\partial \wp^1}{\partial y}$ and $\frac{\partial \wp^2}{\partial t} = B^{22}_{22}\frac{\partial \wp^2}{\partial^2 y}$ are strictly hyperbolic and parabolic, respectively, where $\wp^1 = \{\rho,\, v_1,\, v_2,\, \theta\}$ and $\wp^2 = \{\sigma_{11},\, \sigma_{22},\, \sigma_{12},\, q_1,\, q_2\}$.

Strikwerda [94] and Gustafson and Sundstrom [38]: *Given conditions 1–4 are satisfied, for the system (4.26) to be well-posed the number of independent boundary conditions is given by $r + p$, where r is the rank of sub matrix B^{22}_{22} and p is the number of negative eigenvalues of A^2_{11}.*

Note that the sub-matrix A^2_{11} corresponds to the (linear) Euler equations which has the following eigen structure:

$$\lambda_i = -v_0, -v_0,\ -v_0 \pm \sqrt{\frac{5}{3}\theta_0}.$$

Therefore, on a subsonic inflow ($v_0 > 0$ and $|v_0| \leq \sqrt{\frac{5}{3}\theta_0}$) the R13–moment system requires $5 + 3 = 8$ boundary conditions, whereas for a subsonic outflow ($v_0 < 0$ and $|v_0| \leq \sqrt{\frac{5}{3}\theta_0}$), $5 + 1 = 6$ boundary conditions are required. On a far-field boundary, sufficiently away from in/out–flow, where $v_0/\sqrt{\theta_0} \approx 0$, a total of $5 + 1 = 6$ boundary conditions must be prescribed. Here, we shall only consider the later case, i.e., $v_0/\sqrt{\theta_0} \approx 0$.

4.3.2 Kinetic formulation of open boundaries

We consider an open boundary, so that, the gas can exchange both mass and energy with the outside surroundings. For instance, consider a gas flow between two large reservoirs through a small pipe, see Fig. (4.2). Both reservoirs are maintained at different pressures and temperatures.

We are primarily interested in the flow properties in the pipe, which, however, depend on the conditions in both reservoirs. In engineering, the usual method is to introduce open boundaries (depicted by dotted lines in Fig. (4.2)) and cut off the unbounded domain of the reservoirs. In general, these artificial boundary conditions are only an approximation, hence, the remaining computational domain must be quite large when high accuracy is required. In practice, in order to limit the computational

cost, open boundaries cannot be chosen too far from the domain of interest. Thus, designing these open boundaries becomes important.

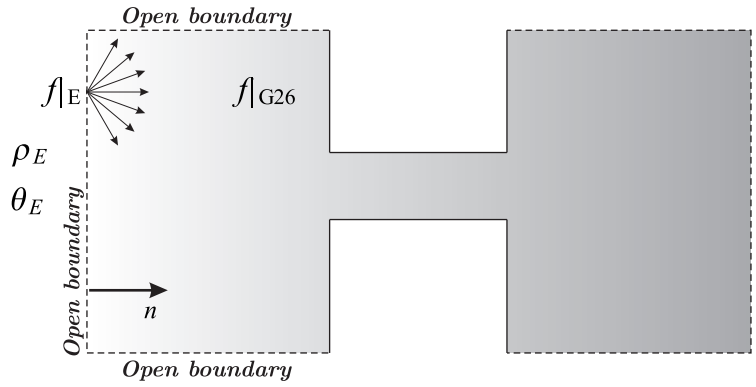

Figure 4.2: An illustration of an open boundary.

We consider an open boundary, where particles flying out ($c_k^B n_k \leq 0$) have a distribution $f|_{\mathrm{G26}}$ and particles entering the gas ($c_k^B n_k \geq 0$) are distributed according to a known distribution, see in Fig. (4.2). The macroscopic density and temperature of gas particles entering the domain ($c_k^B n_k \geq 0$) are ρ_E and θ_E, respectively. The gas flow is driven by the density and temperature differences, $\delta\rho = \rho - \rho_E$ and $\delta\theta = \theta - \theta_E$.

It is assumed that the gas outside the computational domain (i.e., far in the reservoirs) is in equilibrium and leaving or entering of particles does not disturb the equilibrium. In other words, we assume that the open boundaries are far enough and the pressure and temperature deviations are small, i.e., $\delta\theta \ll \theta_0$ and $\delta\rho \ll \rho_0$. Therefore, the distribution function for the gas particles entering through the boundary ($c_k^B n_k \geq 0$) can be represented by a Maxwellian distribution, as

$$f|_{\mathrm{E}} = \frac{\rho_E}{\sqrt{2\pi\theta_E}^3} \exp\left(-\frac{c_B^2}{2\theta_E}\right).$$

Accordingly, in (4.5), the distribution function $\bar{f}$ of the particles at the boundary is

$$\bar{f} = \begin{cases} f|_{\mathrm{G26}} & , \quad c_k^B n_k \leq 0 \\ f|_{\mathrm{E}} & , \quad c_k^B n_k \geq 0. \end{cases} \tag{4.27}$$

Again, assuming small deviations from the equilibrium state, linearization of (4.27) can be performed with respect to a reference equilibrium state, given by $\rho_0 = 1$,

$\theta_0 = 1$. After linearization, evaluation of (4.12) using (4.27), in dimensionless form, give explicit expressions for the open boundary conditions as

$$
\begin{aligned}
v_y &= -\sqrt{\frac{2}{\pi}}\left(\frac{\delta\theta}{2} + \delta\rho + \frac{\sigma_{yy}}{2} - \frac{R_{yy}}{28} - \frac{\Delta}{120}\right) && \text{(4.28a)}\\
\sigma_{xy} &= -\sqrt{\frac{2}{\pi}}\left(v_x + \frac{q_x}{5} + \frac{m_{xyy}}{2}\right) && \text{(4.28b)}\\
q_y + \frac{1}{2}v_y &= -\sqrt{\frac{2}{\pi}}\left(2\delta\theta + \frac{\sigma_{yy}}{2} + \frac{5R_{yy}}{28} + \frac{\Delta}{15}\right) && \text{(4.28c)}\\
R_{xy} &= \sqrt{\frac{2}{\pi}}\left(v_x - \frac{11q_x}{5} - \frac{m_{xyy}}{2}\right) && \text{(4.28d)}\\
m_{xxy} - \frac{1}{5}v_y &= -\sqrt{\frac{2}{\pi}}\left(\frac{\delta\theta}{5} + \sigma_{xx} - \frac{\sigma_{yy}}{5} + \frac{\Delta}{150} + \frac{R_{xx}}{14}\right) && \text{(4.28e)}\\
m_{yyy} + \frac{2}{5}v_y &= \sqrt{\frac{2}{\pi}}\left(\frac{2\delta\theta}{5} - \frac{7\sigma_{yy}}{5} - \frac{R_{yy}}{14} + \frac{\Delta}{75}\right), && \text{(4.28f)}
\end{aligned}
$$

where $\delta\theta = \theta - \theta_E$ and $\delta\rho = \rho - \rho_E$ and, for convenience, we assumed that the boundary is at rest, i.e., $v_i^W = 0$. Note that in this case gas particles can penetrate the boundary, thus $v_k n_k \neq 0$. For $v_k n_k = 0$, (4.28) reduces to the corresponding linear wall boundary conditions (4.13) with $\chi = 1$.

4.4 Phenomenological theory of boundary conditions

In the last chapter, we discussed the derivation of the regularized 10–moment equations using the framework of phenomenological linear irreversible thermodynamics (LIT) [23, 48, 71]. The same principle can also be extended to construct boundary conditions for the moment equations [48, 103].

The entropy production at the surface is given by the difference between the entropy fluxes into and out of the surface

$$\Sigma_W = \left(\Psi_k - \frac{q_k^W}{\theta^W}\right) n_k, \tag{4.29}$$

where n_k denotes the unit normal on the wall pointing towards the gas, q_k^W denotes the non-convective energy flux, and θ^W denotes the temperature at the interface. For

the R10 equations, the entropy flux Ψ_k in (4.29) is given from equation (3.40). Note that the wall is assumed as a Fourier heat conductor, with the entropy flux $\frac{q_k^W}{\theta^W}$.

For a gas-wall interface the jump conditions of momentum and energy, at the impermeable boundary, can be written as [23, 48, 103]

$$\begin{aligned} v_k n_k &= 0, && \text{(4.30a)} \\ [\rho \Theta_{ik}]\, n_k &= 0, && \text{(4.30b)} \\ [\rho \Theta_{ik} v_i + q_k]\, n_k &= 0. && \text{(4.30c)} \end{aligned}$$

Brackets denote the jump of the corresponding quantity across the boundary. The jump conditions (4.30) express the continuity of the normal velocity component, stress vector, and the balance of energy across the interface. Next we use relations (4.30a-4.30c) to eliminate q_k^W in equation (4.29). This yields

$$\Sigma_W^{\mathrm{R10}} = \left(\frac{q_k}{5} \Theta_{rr}^{-1} + \frac{2}{5} q_i \Theta_{ik}^{-1} + \frac{1}{2} \Theta_{ij}^{-1} m_{ijk} - \frac{q_k + \rho \left(v_i - v_i^W \right) \Theta_{ik}}{\theta^W} \right) n_k. \tag{4.31}$$

It will be convenient to introduce the normal and tangential components of q_i, σ_{ij}, $m_{ijk} n_k$ as

$$\begin{aligned} q_i &= q_n n_i + \bar{q}_i, \\ \theta_{ij} &= \theta_{nn} \left(\frac{3}{2} n_i n_j - \frac{1}{2} \delta_{ij} \right) + \bar{\theta}_{ni} n_j + \bar{\theta}_{nj} n_i + \widetilde{\theta}_{ij}, \\ m_{ijk} n_k &= m_{nnn} \left(\frac{3}{2} n_i n_j - \frac{1}{2} \delta_{ij} \right) + \bar{m}_{nni} n_j + \bar{m}_{nnj} n_i + \widetilde{m}_{nij}. \end{aligned}$$

Here, $q_n = q_k n_k$, $\bar{q}_i = (q_i - q_n n_i)$, $\theta_{nn} = \theta_{rk} n_k n_r$, $\bar{\theta}_{ni} = \theta_{ik} n_k - \theta_{nn} n_i$, and $\bar{m}_{nni} = m_{irk} n_k n_r - m_{nnn} n_i$, therefore

$$\bar{q}_k n_k = \bar{\theta}_{nk} n_k = \widetilde{\theta}_{kk} = \widetilde{\theta}_{ik} n_k = \bar{m}_{nnk} n_k = \widetilde{m}_{nkk} = 0.$$

Substituting these into equation (4.31) gives the entropy production per unit area as

$$\Sigma_W^{\mathrm{R10}} = q_n \left(\frac{1}{5} \Theta_{rr}^{-1} + \frac{2}{5} \Theta_{ik}^{-1} n_i n_k - \frac{1}{\theta^W} \right) + \frac{2}{5} \bar{q}_i \Theta_{ik}^{-1} n_k + \frac{1}{2} \Theta_{ij}^{-1} m_{ijk} n_k - \frac{\left(v_i - v_i^W \right) \sigma_{ik}}{\theta^W} n_k \,. \tag{4.32}$$

For Θ_{ij} the Cayley-Hamilton theorem implies

$$\Theta_{ij}^{-1} = \frac{1}{2}\frac{(Tr[\Theta])^2 - Tr[\Theta\cdot\Theta]}{\det[\Theta]}\delta_{ij} - \frac{Tr[\Theta]}{\det[\Theta]}\Theta_{ij} + \frac{\Theta_{im}\Theta_{mj}}{\det[\Theta]}. \tag{4.33}$$

Moreover, we shall make use of the following identity

$$\frac{1}{2}\theta\frac{\theta_{ij}\theta_{ij}}{\det[\Theta]} = \frac{\det[\theta_{ij}]}{\det[\Theta]} + \frac{\theta^3}{\det[\Theta]} - 1,$$

along with the Cayley-Hamilton theorem (4.33) to obtain

$$\Theta_{rr}^{-1} = \frac{3}{\theta} - \frac{3}{\theta}\frac{\det[\theta_{ij}]}{\det[\Theta]} + \frac{\theta_{ij}\theta_{ij}}{\det[\Theta]}, \tag{4.34a}$$

$$\Theta_{ik}^{-1}n_in_k = \frac{1}{\theta} - \frac{1}{\theta}\frac{\det[\theta_{ij}]}{\det[\Theta]} - \frac{\theta\theta_{ik}}{\det[\Theta]}n_in_k + \frac{\theta_{im}\theta_{mk}}{\det[\Theta]}n_in_k, \tag{4.34b}$$

$$\bar{q}_i\Theta_{ik}^{-1}n_k = -\frac{\theta}{\det[\Theta]}\bar{q}_i\theta_{ik}n_k + \frac{\theta_{im}\theta_{mk}}{\det[\Theta]}\bar{q}_in_k, \text{ and} \tag{4.34c}$$

$$\Theta_{ij}^{-1}m_{ijk}n_k = -\frac{\theta}{\det[\Theta]}\theta_{ij}m_{ijk}n_k + \frac{\theta_{im}\theta_{mj}}{\det[\Theta]}m_{ijk}n_k\ . \tag{4.34d}$$

Substitution of relations (4.34a−4.34d) into the entropy production (4.32) gives

$$\begin{aligned}\Sigma_W^{\mathrm{R10}} = &-\frac{q_n}{\theta\det\left[\frac{\Theta}{\theta}\right]}\left[\frac{\hat{\mathcal{T}}}{1-\hat{\mathcal{T}}}\det\left(\frac{\Theta}{\theta}\right) + \frac{2}{5}\frac{\theta_{nn}}{\theta} - \frac{1}{5}\frac{\theta_{ij}\theta_{ij}}{\theta^2} - \frac{2}{5}\frac{\theta_{nn}^2}{\theta^2} - \frac{2}{5}\frac{\bar{\theta}_{nj}\bar{\theta}_{nj}}{\theta^2} + \det\left(\frac{\theta_{ij}}{\theta}\right)\right]\\ &- \frac{\bar{\theta}_{nk}}{\theta\det\left[\frac{\Theta}{\theta}\right]}\left[\rho\mathcal{V}_k\frac{\det\left(\frac{\Theta}{\theta}\right)}{\left(1-\hat{\mathcal{T}}\right)} + \frac{2}{5}\frac{\bar{q}_k}{\theta} + \frac{\bar{m}_{nnk}}{\theta} - \frac{\left(\theta_{ik}+\frac{1}{2}\theta_{nn}\delta_{ik}\right)\left(\bar{m}_{nni}+\frac{2}{5}\bar{q}_i\right)}{\theta^2}\right]\\ &- \frac{m_{nnn}}{\theta\det\left[\frac{\Theta}{\theta}\right]}\left[\frac{3}{4}\frac{\theta_{nn}}{\theta} + \frac{1}{4}\frac{\theta_{ij}\theta_{ij}}{\theta^2} - \frac{3}{4}\frac{\bar{\theta}_{nj}\bar{\theta}_{nj}}{\theta^2} - \frac{3}{4}\frac{\theta_{nn}^2}{\theta^2}\right] - \frac{1}{2}\frac{\widetilde{m}_{nij}}{\theta\det\left[\frac{\Theta}{\theta}\right]}\left[\frac{\widetilde{\theta}_{ij}}{\theta} - \frac{\theta_{im}\theta_{mj}}{\theta^2}\right].\end{aligned} \tag{4.35a}$$

where $\hat{\mathcal{T}} = \left(\theta - \theta^W\right)/\theta$. Equation (4.35) gives an expression for the entropy production rate at the wall in terms of moments, q_n, $\bar{\theta}_{nk}$, m_{nnn}, and $\widetilde{m}_{nij}$.

Similarly, one can obtain the wall entropy production rate for the linear R13

equations (LR13) as [103]

$$\Sigma_W^{\mathrm{LR13}} = -\frac{q_n}{\theta_0}\left[\frac{\theta-\theta^W}{\theta_0}+\frac{2}{5}\frac{\sigma_{nn}}{p_0}+\frac{1}{5}\frac{R_{nn}}{\theta_0 p_0}+\frac{1}{15}\frac{\Delta}{\theta_0 p_0}\right] - \frac{\bar{\sigma}_{nk}}{p_0}\left[\rho_0\mathcal{V}_k+\frac{2}{5}\frac{\bar{q}_k}{\theta_0}+\frac{\bar{m}_{nnk}}{\theta_0}\right]-\frac{3}{4}\frac{m_{nnn}}{\theta_0}\left[\frac{\sigma_{nn}}{p_0}\right]-\frac{1}{2}\frac{\widetilde{m}_{nij}}{\theta_0}\left[\frac{\widetilde{\sigma}_{ij}}{p_0}\right]-\frac{1}{5}\frac{\bar{R}_{nk}}{\theta_0 p_0}\left[\frac{\bar{q}_k}{\theta_0}\right]. \tag{4.36a}$$

We shall proceed further—by using (4.36)—to construct phenomenological boundary conditions for the linear R13 equations. Although, the phenomenological boundary conditions for the nonlinear R10 equations will not be presented, they may be constructed using the methodology presented next.

4.4.1 Phenomenological boundary conditions for the Linear R13 equations

To evaluate explicit boundary condition for the linear R13–moment equations, for convenience, we restrict ourself to the x–y plane where wall-normal points toward the $y-$direction. In this case, $\widetilde{m}_{nyy}=0$, $\tilde{m}_{nxx}=m_{xxy}+\frac{1}{2}m_{yyy}$, and equation (4.36) simplifies to

$$\Sigma_W^{\mathrm{LR13}} = -\frac{q_y}{\theta_0}\left[\frac{\theta-\theta^W}{\theta_0}+\frac{2}{5}\frac{\sigma_{yy}}{p_0}+\frac{1}{5}\frac{R_{yy}}{\theta_0 p_0}+\frac{1}{15}\frac{\Delta}{\theta_0 p_0}\right]-\frac{\sigma_{xy}}{p_0}\left[\rho_0\mathcal{V}_x+\frac{2}{5}\frac{q_x}{\theta_0}+\frac{m_{xyy}}{\theta_0}\right] - \frac{m_{yyy}}{\theta_0}\left[\frac{3\sigma_{yy}}{4p_0}\right]-\frac{\left(m_{xxy}+\frac{1}{2}m_{yyy}\right)}{\theta_0}\left[\frac{1}{2p_0}\left(\sigma_{xx}+\frac{1}{2}\sigma_{yy}\right)\right]-\frac{R_{xy}}{\theta_0 p_0}\left[\frac{q_x}{5\theta_0}\right]. \tag{4.37a}$$

Positive entropy production Σ_W^{LR13} can be achieved by writing the unknown boundary values for the moments proportional to their driving forces (the expressions in square brackets) [23, 48].

To generalize the procedure in [103], we consider the coupling between the cross terms of the same tensorial structure [48], i.e., scalars (q_n, m_{nnn}), vectors ($\bar{\sigma}_{nk}$, $\bar{R}_{nk}$) and tensor $\widetilde{m}_{nij}$. This allows us to obtain the following phenomenological boundary conditions for the linear R13–moment equations,

$$\sigma_{xy} = -\frac{\varsigma_0}{\sqrt{\theta_0}}\left(p_0\mathcal{V}_x + \left(\frac{2}{5} - \frac{1}{5}\varsigma_1\right)q_x + m_{xyy}\right), \tag{4.38a}$$

$$R_{xy} = \frac{\varsigma_0\varsigma_1}{\sqrt{\theta_0}}\left(p_0\theta_0\mathcal{V}_x + \left(\frac{2}{5} - \frac{13}{5}\frac{\varsigma_2}{\varsigma_1}\right)\theta_0 q_x + \theta_0 m_{xyy}\right), \tag{4.38b}$$

$$q_y = -\frac{\tau_0}{\sqrt{\theta_0}}\left(2p_0\left(\theta - \theta^W\right) + \left(\frac{4}{5} - \frac{3}{10}\tau_1\right)\theta_0\sigma_{yy} + \frac{2R_{yy}}{5} + \frac{2\Delta}{15}\right), \tag{4.38c}$$

$$m_{yyy} = \frac{\tau_1\tau_0}{\sqrt{\theta_0}}\left(\frac{2}{5}p_0\left(\theta - \theta^W\right) + \left(\frac{4}{25} - \frac{39}{25}\frac{\tau_2}{\tau_1}\right)\theta_0\sigma_{yy} + \frac{2R_{yy}}{25} + \frac{2\Delta}{75}\right), \tag{4.38d}$$

$$m_{xxy} = -\frac{\tau_1\tau_0}{\sqrt{\theta_0}}\left(\frac{1}{5}p_0\left(\theta - \theta^W\right) + \frac{\varpi_0}{\tau_1\tau_0}\theta_0\sigma_{xx} + \frac{1}{2}\left(\frac{4}{25} - \frac{39}{25}\frac{\tau_2}{\tau_1} + \frac{\varpi_0}{\tau_1\tau_0}\right)\theta_0\sigma_{yy} + \frac{1}{25}R_{yy} + \frac{1}{75}\Delta\right). \tag{4.38e}$$

Here, the matrices

$$\varsigma_{ij} = \begin{bmatrix} \varsigma_0 & -\varsigma_0\varsigma_1 \\ -\varsigma_0\varsigma_1 & 13\varsigma_0\varsigma_2 \end{bmatrix}, \quad \tau_{ij} = \begin{bmatrix} 2\tau_0 & -\frac{2}{5}\tau_1\tau_0 \\ -\frac{2}{5}\tau_1\tau_0 & \frac{52}{25}\tau_2\tau_0 \end{bmatrix} \tag{4.39}$$

are any arbitrary symmetric non-negative definite matrices of Onsager coefficients and ϖ_0 is an arbitrary non-negative coefficient. These coefficients must be determined from microscopic theories or measurements. For instance, comparison of (4.38) with the slip conditions (4.13) (after linearization) allows to identify $\varsigma_0 = \tau_0 = \frac{\chi}{2-\chi}\sqrt{\frac{2}{\pi}}$, $\varsigma_1 = \varsigma_2 = \tau_1 = \tau_2 = \varpi_0 = 1$. Moreover, Maxwell's accommodation model predicts different factors for m_{ijk}, R_{ij} and Δ terms in the boundary conditions. For example, in boundary conditions for σ_{xy}, Maxwell accommodation model gives a factor $1/2$ for m_{xyy}, whereas, the corresponding phenomenological theory predicts the factor 1.

Similarly, from (4.35) (after ignoring non-linear terms of order 3 or higher), one obtains the phenomenological boundary conditions for the linear R10 equations as (4.38).

$$\sigma_{xy} = -\frac{\varsigma_0}{\sqrt{\theta_0}}\left(p_0\mathcal{V}_x + \frac{2}{5}q_x + m_{xyy}\right) \tag{4.40a}$$

$$q_y = -\frac{\tau_0}{\sqrt{\theta_0}}\left(2p_0\left(\theta-\theta^W\right) + \left(\frac{4}{5} - \frac{3}{10}\tau_1\right)\theta_0\sigma_{yy}\right) \tag{4.40b}$$

$$m_{yyy} = \frac{\tau_1\tau_0}{\sqrt{\theta_0}}\left(\frac{2}{5}p_0\left(\theta-\theta^W\right) + \left(\frac{4}{25} - \frac{39}{25}\frac{\tau_2}{\tau_1}\right)\theta_0\sigma_{yy}\right) \tag{4.40c}$$

$$m_{xxy} = -\frac{\tau_1\tau_0}{\sqrt{\theta_0}}\left(\frac{1}{5}p_0\left(\theta-\theta^W\right) + \frac{\varpi_0}{\tau_1\tau_0}\theta_0\sigma_{xx} + \frac{1}{2}\left(\frac{4}{25} - \frac{39}{25}\frac{\tau_2}{\tau_1} + \frac{\varpi_0}{\tau_1\tau_0}\right)\theta_0\sigma_{yy}\right). \tag{4.40d}$$

A comparison of (4.40) with the slip condition given by the equation (4.14) shows that in (4.14), instead of the factor 1/5 for q_x the phenomenological theory predicts the factor 2/5.

Part II

SOLUTIONS OF BOUNDARY VALUE PROBLEMS

Chapter 5

Linear Theory

In this chapter, we discuss one-dimensional steady flows through the R13–moment equations, applied to viscous slip and temperature jump problems [89, 60, 59, 63]. The flow fields are assumed to be a small perturbation from the equilibrium so that the governing equations and boundary conditions can be linearized; this allows closed form analytic solutions for the R13 equations. We shall investigate the solutions of the R13 equations for the Knudsen layer corrections in slip and jump coefficients using phenomenological boundary conditions.

5.1 1D equations

In this section, the moment equations will be presented for one dimensional steady state, where velocity, temperature, and all other flow parameters depend only on the $y-$coordinate. The velocity component normal to the walls, v_y, is zero. The velocity, heat-flux and stress tensor, reduce to

$$\vec{v} = \{v_x(y),\ 0,\ 0\},\ \ \vec{q} = \{q_x(y),\ q_y(y),\ 0\}\ \text{ and}$$

$$\sigma_{ij} = \begin{bmatrix} \sigma_{xx}(y) & \sigma_{xy}(y) & 0 \\ \sigma_{xy}(y) & \sigma_{yy}(y) & 0 \\ 0 & 0 & -\sigma_{xx}(y) - \sigma_{yy}(y) \end{bmatrix}.$$

Based on the above assumptions, the mass balance equation (3.25a) is identically satisfied. Furthermore, the momentum and energy conservation equations (3.25b-

3.25c) reduce to

$$\begin{aligned} \sigma'_{xy} &= 0, && \text{(5.1a)} \\ p' + \sigma'_{yy} &= 0, && \text{(5.1b)} \\ q'_y + \sigma_{xy} v'_x &= 0. && \text{(5.1c)} \end{aligned}$$

Here, the prime denotes the differentiation with respect to y. The NSF theory imposes the following constitutive equations for stress tensor and heat flux vector

$$\sigma_{xx} = 0, \quad \sigma_{xy} = -\mu v'_x, \quad \sigma_{yy} = 0, \tag{5.2}$$

and

$$q_x = 0, \quad q_y = -\mu \frac{1}{\mathrm{Pr}} \frac{5}{2} \theta'. \tag{5.3}$$

In the R13 theory, however, the stress tensor and the heat flux are given by their respective balance equations, (3.26) and (3.27), which now read

$$\begin{aligned} \frac{4}{3}\sigma_{xy} v'_x - \frac{4}{15} q'_y + m'_{xxy} &= -\frac{p}{\mu}\sigma_{xx}, && \text{(5.4a)} \\ \left(p + \sigma_{yy}\right) v'_x + \frac{2}{5} q'_x + m'_{xyy} &= -\frac{p}{\mu}\sigma_{xy}, && \text{(5.4b)} \\ -\frac{2}{3}\sigma_{xy} v'_x + \frac{8}{15} q'_y + m'_{yyy} &= -\frac{p}{\mu}\sigma_{yy}, && \text{(5.4c)} \end{aligned}$$

and

$$\begin{aligned} -\theta \tfrac{\sigma_{xy}}{\rho} \rho' + \left(\tfrac{7}{5} q_y + m_{xxy}\right) v'_x + \tfrac{5}{2}\sigma_{xy}\theta' - \tfrac{\sigma_{xy}}{\rho}\sigma'_{yy} \\ + \left(\theta - \tfrac{\sigma_{xx}}{\rho}\right)\sigma'_{xy} + \tfrac{1}{2} R'_{xy} = -\,\mathrm{Pr}\, \tfrac{p}{\mu} q_x, \\ -\theta \tfrac{\sigma_{yy}}{\rho} \rho' + \left(\tfrac{2}{5} q_x + m_{xyy}\right) v'_x + \tfrac{5}{2}\left(p + \sigma_{yy}\right)\theta' \\ + \left(\theta - \tfrac{\sigma_{yy}}{\rho}\right)\sigma'_{yy} - \tfrac{\sigma_{xy}}{\rho}\sigma'_{xy} + \tfrac{1}{2}\left(R'_{yy} + \tfrac{1}{3}\Delta'\right) = -\,\mathrm{Pr}\, \tfrac{p}{\mu} q_y. \end{aligned} \tag{5.5}$$

The R13 constitutive relations for m_{ijk}, R_{ij}, and Δ in the above equations are obtained from (3.31), they read

$$\begin{aligned}
\mathrm{Pr_M}\frac{p}{\mu}m_{xxx} &= \frac{6}{5}\theta\left(\sigma'_{xy}-\frac{\sigma_{xy}}{p}p'\right), && (5.6a)\\
\mathrm{Pr_M}\frac{p}{\mu}m_{xxy} &= \theta\left(\frac{2}{5}\left(\sigma'_{yy}-\frac{\sigma_{yy}}{p}p'\right)-\left(\sigma'_{xx}-\frac{\sigma_{xx}}{p}p'\right)\right), && (5.6b)\\
\mathrm{Pr_M}\frac{p}{\mu}m_{xyy} &= -\frac{8}{5}\theta\left(\sigma'_{xy}-\frac{\sigma_{xy}}{p}p'\right), && (5.6c)\\
\mathrm{Pr_M}\frac{p}{\mu}m_{yyy} &= -\frac{9}{5}\theta\left(\sigma'_{yy}-\frac{\sigma_{yy}}{p}p'\right), && (5.6d)
\end{aligned}$$

and

$$\begin{aligned}
\mathrm{Pr_R}\frac{p}{\mu}R_{xx} &= -\frac{28}{15}\theta\left(-q'_{y}+\frac{q_y}{p}p'\right), && (5.7a)\\
\mathrm{Pr_R}\frac{p}{\mu}R_{xy} &= \frac{14}{5}\theta\left(-q'_{x}+\frac{q_x}{p}p'\right), && (5.7b)\\
\mathrm{Pr_R}\frac{p}{\mu}R_{yy} &= \frac{56}{15}\theta\left(-q'_{y}+\frac{q_y}{p}p'\right), && (5.7c)\\
\mathrm{Pr}_\Delta\frac{p}{\mu}\Delta &= -8\theta\left(q'_{y}-\frac{q_y}{p}\right). && (5.7d)
\end{aligned}$$

Here, for brevity and clarity, the nonlinear algebraic terms in the constitutive relations (3.31) are ignored; these terms will vanish in linearization.

5.1.1 Non-dimensionalization of the equations

Throughout this thesis, non-dimensional variables and equations are used. In order to non-dimensionalize the moment equations and related variables, we introduce reference quantities. Let L, ρ_0, θ_0 be reference length, density, and temperature, respectively, and let $v_0=\sqrt{\theta_0}$ be the reference velocity. Then the nondimensional variables are defined as

$$\begin{array}{llllll}
\hat{x}_i=\frac{x_i}{L}, & \hat{\rho}=\frac{\rho}{\rho_0}, & \hat{\theta}=\frac{\theta}{\theta_0}, & \hat{v}_i=\frac{v_i}{\sqrt{\theta_0}}, & \hat{t}=t\frac{L}{\sqrt{\theta_0}},\\
\hat{\sigma}_{ij}=\frac{\sigma_{ij}}{\rho_0\theta_0}, & \hat{q}_i=\frac{q_i}{\rho_0\sqrt{\theta_0}^3}, & \hat{m}_{ijk}=\frac{m_{ijk}}{\rho_0\sqrt{\theta_0}^3}, & \hat{R}_{ij}=\frac{R_{ij}}{\rho_o\theta_0^2}, & \hat{\Delta}=\frac{\Delta}{\rho_o\theta_0^2}.
\end{array}$$

The hat over quantities represents corresponding non-dimensional quantities. As a result of non-dimensionalization the Knudsen number appears in the governing

equations, as

$$\hat{\mu} = \frac{\mu}{\mu_0} = \frac{\mu}{\mathrm{Kn}\rho_0\sqrt{\theta_0}L}. \tag{5.8}$$

For brevity, the hats will be removed hereafter, and unless otherwise stated, all variables will be given in non-dimensional form.

5.1.2 Linearization of the equations

For flows with small deviations from the equilibrium state, linearization can be performed with respect to a reference equilibrium state, given by $\rho_0 = 1$, $\theta_0 = 1$ in the dimensionless formulation. These deviations are represented by

$$\bar{\rho} = \rho - 1, \quad \bar{\theta} = \theta - 1, \quad \bar{v}_i = v_i, \quad \bar{\sigma}_{ij} = \sigma_{ij}, \tag{5.9a}$$

$$\bar{q}_i = q_i, \quad \bar{R}_{ij} = R_{ij}, \quad \bar{m}_{ijk} = m_{ijk} \quad \text{and} \quad \bar{\Delta} = \Delta. \tag{5.9b}$$

The linearized equations are obtained by introducing the dimensionless quantities from equation (5.9) into the moment equations and keeping only the terms that are linear in the deviations. For example, the conservation laws in equations (5.1) simplify to

$$\bar{\sigma}'_{xy} = 0 \tag{5.10a}$$

$$\bar{\rho}' + \bar{\theta}' + \bar{\sigma}'_{yy} = 0 \tag{5.10b}$$

$$\bar{q}'_y = 0. \tag{5.10c}$$

Note that in the energy conservation law (5.1), the viscous heating term, $\sigma_{xy}v'_x$ is nonlinear, and therefore does not contribute in linearization. Viscous heating describes the coupling between velocity and temperature fields.

5.2 General solutions for linear equations

Owing to the assumptions made in the above, the linear equations can be solved analytically. Furthermore, as a result of linearization, the moment equations in 1D are decoupled into the velocity related equations and temperature related equations.

5.2.1 The velocity problem

In the Navier–Stokes–Fourier equations, the velocity is described by the $x-$momentum equation (5.10a) and the linearized constitutive equations for $\bar{\sigma}_{xy}$, i.e., $\bar{\sigma}'_{xy} = 0$, $\bar{\sigma}_{xy} = -\mathrm{Kn}\bar{v}'_x$, respectively. The solution for these equations follows by integrating as

$$\bar{\sigma}_{xy} = \mathbf{c}_2, \qquad \bar{v}_x = \mathbf{c}_1 - y\frac{\mathbf{c}_2}{\mathrm{Kn}}, \tag{5.11}$$

where $\mathbf{c}_1$ and $\mathbf{c}_2$ are the integrating constants, that need to be determined from appropriate boundary conditions. Note that for the linear case, the R10 equations reduce to the NSF equations.

The equations involved in the velocity problem from the linearized R13 moment system stem from Eq. (5.10a), Eq. (5.4b) and Eq. (5.5), as

$$\begin{aligned}
\bar{\sigma}'_{xy} &= 0, && (5.12a)\\
\bar{v}'_x + \frac{2}{5}\bar{q}'_x + \bar{m}'_{xyy} &= -\frac{1}{\mathrm{Kn}}\bar{\sigma}_{xy}, && (5.12b)\\
\bar{\sigma}'_{xy} + \frac{1}{2}\bar{R}'_{xy} &= -\Pr\frac{1}{\mathrm{Kn}}\bar{q}_x, && (5.12c)
\end{aligned}$$

respectively. Equations (5.12) are closed by the constitutive relations, obtained from (5.6c–5.7b), which are

$$\bar{m}_{xyy} = -\mathrm{Kn}\frac{1}{\mathrm{Pr_M}}\frac{8}{5}\bar{\sigma}'_{xy} \quad \text{and} \quad \bar{R}_{xy} = -\mathrm{Kn}\frac{1}{\mathrm{Pr_R}}\frac{14}{5}\bar{q}'_x. \tag{5.13}$$

Thus, the general solution for (5.12) and (5.13) reads

$$\begin{aligned}
\bar{\sigma}_{xy} &= \mathbf{c}_2 && (5.14a)\\
\bar{v}_x &= \mathbf{c}_1 - y\frac{\mathbf{c}_2}{\mathrm{Kn}} - \underline{\frac{2}{5}\left(\mathbf{c}_3 e^{-\frac{y\beta}{\mathrm{Kn}}} + \mathbf{c}_4 e^{\frac{y\beta}{\mathrm{Kn}}}\right)}, && (5.14b)\\
\bar{q}_x &= \underline{\left(\mathbf{c}_3 e^{-\frac{y\beta}{\mathrm{Kn}}} + \mathbf{c}_4 e^{\frac{y\beta}{\mathrm{Kn}}}\right)}, && (5.14c)\\
\bar{R}_{xy} &= \frac{2\Pr}{\beta}\underline{\left(\mathbf{c}_3 e^{-\frac{y\beta}{\mathrm{Kn}}} - \mathbf{c}_4 e^{\frac{y\beta}{\mathrm{Kn}}}\right)}, && (5.14d)\\
\bar{m}_{xyy} &= 0, && (5.14e)
\end{aligned}$$

where $\mathbf{c}_1$, $\mathbf{c}_2$, $\mathbf{c}_3$, $\mathbf{c}_4$ are constants of integration and $\beta = \sqrt{\frac{5}{7}\Pr\mathrm{Pr_R}}$.

5.2.2 The temperature problem

The temperature related variables, in the linear NSF theory, are obtained from equations (5.10c) and (5.3), as

$$\bar{q}_y' = 0, \quad \bar{q}_y = -\mathrm{Kn}\frac{1}{\mathrm{Pr}}\frac{5}{2}\bar{\theta}'.$$

The solution for the above equations read

$$\bar{q}_y = \mathbf{c}_1, \quad \text{and} \quad \bar{\theta} = \mathbf{c}_2 - y\frac{2\,\mathrm{Pr}}{5\mathrm{Kn}}\mathbf{c}_1. \tag{5.15}$$

Similarly, for the linear R13 equations, the following solution is obtained from Eqs. (5.10c), (5.5), (5.7c), (5.7d), (5.6d) and (5.4c), as

$$\begin{aligned}
\bar{q}_y &= \mathbf{c}_1, && (5.16a)\\
\bar{\theta} &= \mathbf{c}_2 - y\frac{2\,\mathrm{Pr}}{5\mathrm{Kn}}\mathbf{c}_1 - \underline{\frac{2}{5}\left(\mathbf{c}_3 e^{-\frac{y\gamma}{\mathrm{Kn}}} - \mathbf{c}_4 e^{\frac{y\gamma}{\mathrm{Kn}}}\right)}, && (5.16b)\\
\bar{\sigma}_{yy} &= \underline{\left(\mathbf{c}_3 e^{-\frac{\gamma y}{\mathrm{Kn}}} - \mathbf{c}_4 e^{\frac{\gamma y}{\mathrm{Kn}}}\right)}, && (5.16c)\\
\bar{m}_{yyy} &= \underline{\frac{1}{\gamma}\left(\mathbf{c}_3 e^{-\frac{\gamma y}{\mathrm{Kn}}} + \mathbf{c}_4 e^{\frac{\gamma y}{\mathrm{Kn}}}\right)}, && (5.16d)\\
\bar{R}_{yy} &= \underline{\bar{\Delta} = 0}. && (5.16e)
\end{aligned}$$

where $\mathbf{c}_1$, $\mathbf{c}_2$, $\mathbf{c}_3$, $\mathbf{c}_4$ are constants of integration and $\gamma = \frac{\sqrt{5\,\mathrm{Pr_M}}}{3}$. The exponential functions in Eqs. (5.14) and Eqs. (5.16) describe Knudsen layers, which are absent in the NSF solutions given by Eqs. (5.11) and (5.15).

In the solutions predicted by the R13–moment equations, the macroscopic quantities are superpositions of bulk solutions and Knudsen layers. For example, the solutions for $\bar{v}_x$ and $\bar{\theta}$ are summations of Knudsen layers (indicated by the underlined terms) and the bulk solutions, $\mathbf{c}_1 - y\frac{\mathbf{c}_2}{\mathrm{Kn}}$, $\mathbf{c}_2 - y\frac{2\,\mathrm{Pr}}{5\mathrm{Kn}}\mathbf{c}_1$, respectively. Note that $\bar{q}_x$, $\bar{R}_{xy}$, $\bar{\sigma}_{yy}$, and $\bar{m}_{yyy}$ are pure Knudsen layers, and thus are pure rarefaction effects.

A detailed examination of a simple kinetic equation shows that in higher order moment equations the Knudsen layers appear as superpositions of several exponential layers with different coefficients in their exponents [99]. The R13–moment equations, however, only have few layers for the superposition, and thus cannot match the full details of the Knudsen layers. In [36, 37], the authors have computed Kramers' problem with the R26–moment equations. The R26–moment equations have more moments,

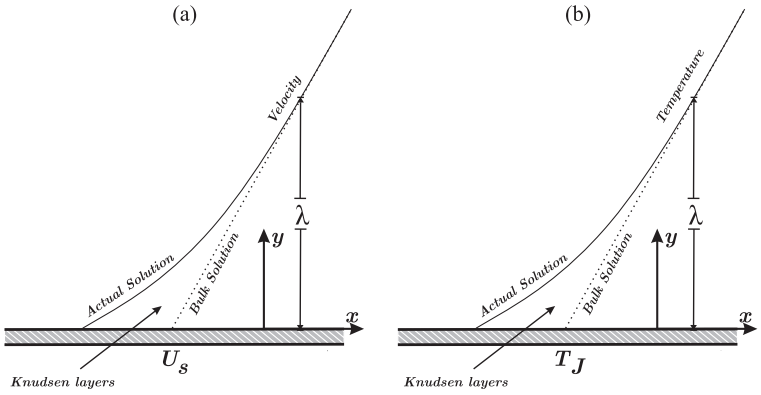

Figure 5.1: Schematic diagrams illustrating (a) the Kramers' problem and (b) temperature jump problem.

thus give more Knudsen layers. These additional layers lead to improvement over the R13–moment equations for Knudsen layer dominated problems. Nevertheless, it is important to emphasize that, with in an appropriate range of Knudsen numbers, the R13 equations can give results in good agreement to kinetic equations. In the following, the solutions obtained from linearized R13–moment equations will be compared to the numerical solutions of the Boltzmann equation.

5.3 Viscous slip problem

The viscous slip problem, also known as Kramers' problem, is one of the most classical boundary value problems to observe the effects of the Knudsen layers [89, 76, 60, 63]. In Kramers' problem, one considers the gas flow in the $y \geq 0$ half-space domain, with one wall located at $y = 0$, as demonstrated in Fig. 5.1(a). The wall is stationary and kept at an ambient temperature θ_0. The flow is parallel to the wall, in $x-$direction, and the temperature and density of the gas are constant, $\theta = \theta_0$ and $\rho = \rho_0$. Far from the wall, the velocity is a linear function of y and there is a constant velocity gradient normal to the wall in the y-direction, i.e., $\partial v_x/\partial y = a$. Hence, from Eqs. (5.14), $\mathbf{c}_2 = -a\mathrm{Kn}$. Moreover, the velocity should be a linear function as $y \to \infty$, we obtain $\mathbf{c}_4 = 0$. The integration constants $\mathbf{c}_1$ and $\mathbf{c}_3$ in Eqs. (5.14) can be determined from the kinetic boundary conditions Eq. (4.13b) and Eq. (4.13f), which in this case reduce

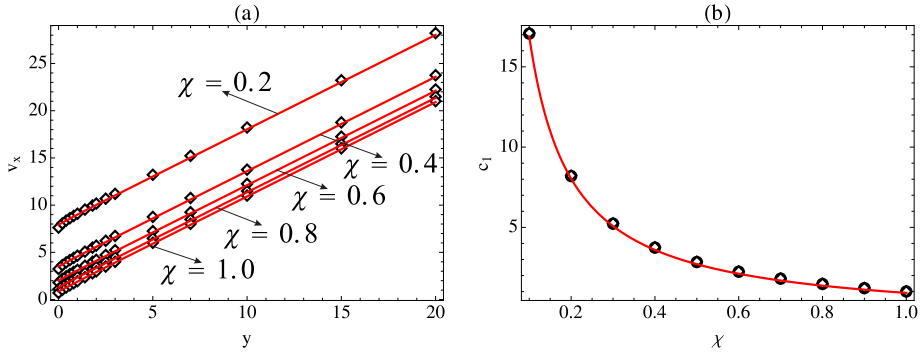

Figure 5.2: (a) Velocity profiles with respect to y, obtained for different accommodation coefficients χ. (b) Viscous slip velocity $\mathbf{c}_1$ with respect to the accommodation coefficient χ. Solutions for the linearized R13 equations (continuous line) are compared with the linearized BGK-Boltzmann solutions [60, 63] (symbols).

to

$$\bar{\sigma}_{xy} = -\frac{\chi}{2-\chi}\sqrt{\frac{2}{\pi}}\left(\bar{v}_x + \frac{1}{5}\bar{q}_x\right), \tag{5.17a}$$

$$\bar{R}_{xy} = \frac{\chi}{2-\chi}\sqrt{\frac{2}{\pi}}\left(\bar{v}_x - \frac{11}{5}\bar{q}_x\right). \tag{5.17b}$$

Substituting Eqs. (5.14) into the boundary conditions (5.17), the velocity $\bar{v}_x$ and the constants $\mathbf{c}_1$ and $\mathbf{c}_3$ are obtained as

$$\bar{v}_x = \mathbf{c}_1 + ay - \underbrace{\frac{2}{5}\left(\mathbf{c}_3 e^{-\frac{y\beta}{\mathrm{Kn}}}\right)}_{\text{Knudsen layers}}, \tag{5.18}$$

where

$$\mathbf{c}_1 = \frac{\sqrt{\frac{70\pi\,\mathrm{Pr}}{\mathrm{Pr_R}}} + 13\frac{\chi}{(2-\chi)}}{\sqrt{\frac{70\pi\,\mathrm{Pr}}{\mathrm{Pr_R}}} + 12\frac{\chi}{(2-\chi)}}\left(\mathrm{Kn}\sqrt{\frac{\pi}{2}}\frac{(2-\chi)}{\chi}a\right),$$

$$\mathbf{c}_3 = \frac{5}{\sqrt{\frac{70\pi\,\mathrm{Pr}}{\mathrm{Pr_R}}}\frac{(2-\chi)}{\chi} + 12}\left(\mathrm{Kn}\sqrt{\frac{\pi}{2}}\frac{(2-\chi)}{\chi}a\right).$$

The R13 solution given by equation (5.18) is shown in Fig. (5.2). In order to compare our results with the BGK Boltzmann equation [60, 63], we take $\mathrm{Pr} = \mathrm{Pr_R} = 1$. Figure (5.2 (a)) presents the R13 solutions for velocity in comparison with the BGK-

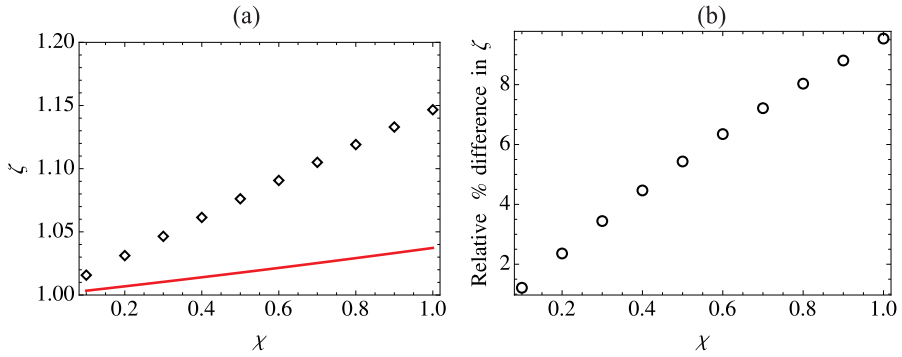

Figure 5.3: (a) Slip coefficient ζ with respect to the accommodation coefficient χ. Results obtained form the linearized R13 equations (continuous line) are compared with linearized BGK-Boltzamann equation (symbols) [60, 63]. (b) Relative % difference in both theories for different accommodation coefficients χ.

Boltzmann solutions [60, 63]. Results are presented for different accommodation coefficients $\chi = 0.2$, 0.4, 0.6, 0.8, and 1 with $\mathrm{Kn} = 1/\sqrt{2}$. Near the wall, we observe a small difference between the R13 and the BGK solutions as the curvature of Knudsen boundary layers for the R13 equations is smaller. Figure (5.2(b)) illustrates the variation in $\mathbf{c}_1$ as predicted by the linear R13–moment equations and BGK-Boltzmann equation [60, 63].

To assess the accuracy of R13–moment equations, we further consider the calculations discussed by Young [126] and Gu et al. [36, 37]. We define the slip coefficient ζ and a coefficient for Knudsen layers $\mathbf{c}_3^*$, as

$$\begin{aligned} \zeta &= \mathbf{c}_1 / \left(\mathrm{Kn} \sqrt{\frac{\pi}{2}} \frac{(2-\chi)}{\chi} a \right), \\ \mathbf{c}_3^* &= \mathbf{c}_3 / \left(\mathrm{Kn} \sqrt{\frac{\pi}{2}} \frac{(2-\chi)}{\chi} a \right). \end{aligned}$$

In Fig. (5.3), we show the slip coefficient ζ versus accommodation coefficient χ, where we compare our results with those from [63, 60]. The slip coefficient predicted by the R13–moment equations is less than the value obtained from BGK [63, 60], by about 10% for $\chi = 1$. The percentage difference between R13 and BGK equation is plotted (on right) in Fig. (5.3(b)). The same comparison was conducted in [36, 37] using the linear R26–moment equations. The value of ζ predicted by the R26 equations lies within about 2% of Boltzmann equation. Obviously, taking more moments gives better description of the process, however, the complexity of the equations also grows.

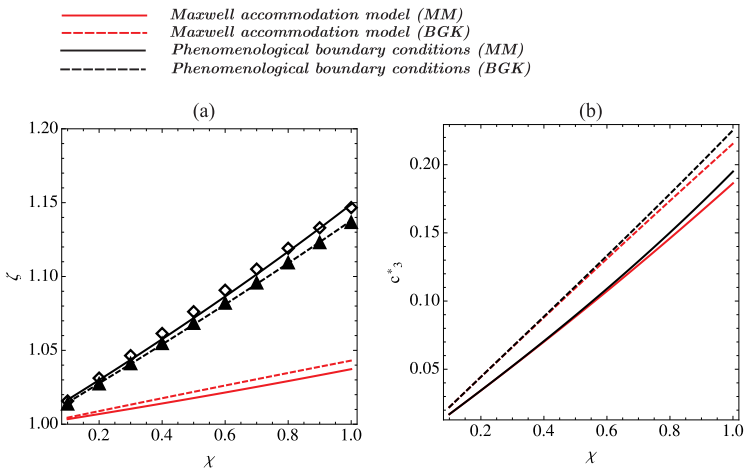

Figure 5.4: Results of the R13 equations obtained using phenomenological boundary conditions and Maxwell accommodation boundary conditions are compared with the solutions of the linear Boltzmann equation (denoted by symbols) for BGK and Maxwell molecules.

Similarly, substituting Eqs. (5.14) into the phenomenological boundary conditions (4.40), the constants $\mathbf{c}_1$ and $\mathbf{c}_3$ are obtained as

$$\mathbf{c}_1 = \frac{1}{\varsigma^*}\frac{\sqrt{70\pi}\sqrt{\frac{\mathrm{Pr}}{\mathrm{Pr_R}}}+13\varsigma^*\varsigma_2\frac{\chi}{2-\chi}}{\sqrt{70\pi}\sqrt{\frac{\mathrm{Pr}}{\mathrm{Pr_R}}}+\varsigma^*\left(13\varsigma_2-\varsigma_1^2\right)\frac{\chi}{2-\chi}}\left(a\mathrm{Kn}\sqrt{\frac{\pi}{2}}\frac{(2-\chi)}{\chi}\right),$$

$$\mathbf{c}_3 = \frac{5\varsigma_1}{\sqrt{70\pi}\sqrt{\frac{\mathrm{Pr}}{\mathrm{Pr_R}}}\frac{(2-\chi)}{\chi}+\varsigma^*\left(13\varsigma_2-\varsigma_1^2\right)}\left(a\mathrm{Kn}\sqrt{\frac{\pi}{2}}\frac{(2-\chi)}{\chi}\right),$$

where we have introduced $\varsigma_0 = \varsigma^*\frac{\chi}{2-\chi}\sqrt{\frac{2}{\pi}}$. Here, we wish to show that by choosing proper ς^*, we can obtain the correct value of the slip coefficient ζ. In Fig. (5.4), we show (a) the slip coefficient ζ and (b) $\mathbf{c}_3^*$ versus accommodation coefficient χ, for $\varsigma^* = 0.9966 - 0.0956\chi$ ($= 0.9982 - 0.0831\chi$ for Maxwell's molecules), $\varsigma_1 = 1$ and $\varsigma_2 = 1$. These expressions for ς^* are obtained by linear fitting.

5.4 Temperature jump problem

In the temperature jump problem, one considers the stationary heat transfer in a gas occupying $y \geq 0$ half-space domain with one wall located at $y = 0$, as demonstrated in Fig. 5.1(b). Far from the wall, the temperature is a linear function and there is a

constant temperature gradient in y-direction, i.e., $\partial\theta/\partial y = b$. Therefore, from (5.16) we get $\mathbf{c}_4 = 0$ and $\mathbf{c}_1 = -\frac{5\mathrm{Kn}}{2\,\mathrm{Pr}}$. To compute the integration constants $\mathbf{c}_3$ and $\mathbf{c}_4$, we substitute equations (5.16) into the linearized Maxwell accommodation boundary conditions from (4.13), i.e.,

$$\bar{q}_y = -\frac{\chi}{2-\chi}\sqrt{\frac{2}{\pi}}\left(2\bar{\theta}+\frac{1}{2}\bar{\sigma}_{yy}\right), \tag{5.19a}$$

$$\bar{m}_{yyy} = \frac{\chi}{2-\chi}\sqrt{\frac{2}{\pi}}\left(\frac{2}{5}\bar{\theta}-\frac{7}{5}\bar{\sigma}_{yy}\right), \tag{5.19b}$$

and find

$$\begin{aligned}
\mathbf{c}_2 &= \frac{5\sqrt{10\pi}+26\sqrt{\mathrm{Pr}_\mathrm{M}}\frac{\chi}{(2-\chi)}}{5\sqrt{10\pi}+25\sqrt{\mathrm{Pr}_\mathrm{M}}\frac{\chi}{(2-\chi)}}\left(\frac{5b}{4\,\mathrm{Pr}}\mathrm{Kn}\sqrt{\frac{\pi}{2}}\frac{(2-\chi)}{\chi}\right),\\
\mathbf{c}_3 &= \frac{4}{3}\frac{\sqrt{\mathrm{Pr}_\mathrm{M}}\frac{\chi}{(2-\chi)}}{\sqrt{10\pi}+5\sqrt{\mathrm{Pr}_\mathrm{M}}\frac{\chi}{(2-\chi)}}\left(\frac{5b}{4\,\mathrm{Pr}}\mathrm{Kn}\sqrt{\frac{\pi}{2}}\frac{(2-\chi)}{\chi}\right).
\end{aligned}$$

Accordingly, we can define the temperature jump coefficient $\zeta_\mathrm{TJ} = \mathbf{c}_2/\left(\frac{5b}{4\,\mathrm{Pr}}\mathrm{Kn}\sqrt{\frac{\pi}{2}}\frac{(2-\chi)}{\chi}\right)$. Note that the NSF theory with first order boundary conditions yields $\zeta_\mathrm{TJ} = 1$. By using phenomenological boundary conditions (4.38), we obtain

$$\begin{aligned}
\mathbf{c}_2 &= \frac{5\sqrt{10\pi}+26\sqrt{\mathrm{Pr}_\mathrm{M}}\tau^*\tau_2\frac{\chi}{(2-\chi)}}{\tau^*\left(5\sqrt{10\pi}+\tau^*\sqrt{\mathrm{Pr}_\mathrm{M}}\,(26\tau_2-\tau_1^2)\,\frac{\chi}{(-2+\chi)}\right)}\left(\sqrt{\frac{\pi}{2}}\frac{5b}{4\,\mathrm{Pr}}\mathrm{Kn}\frac{(2-\chi)}{\chi}\right),\\
\mathbf{c}_3 &= \frac{20\sqrt{\mathrm{Pr}_\mathrm{M}}\tau_1\frac{\chi}{(2-\chi)}}{15\sqrt{10\pi}+3\tau^*\sqrt{\mathrm{Pr}_\mathrm{M}}\,(26\tau_2-\tau_1^2)\,\frac{\chi}{(2-\chi)}}\left(\sqrt{\frac{\pi}{2}}\frac{5b}{4\,\mathrm{Pr}}\mathrm{Kn}\frac{(2-\chi)}{\chi}\right),
\end{aligned}$$

where, as before, we have introduced $\tau_0 = \tau^*\frac{\chi}{2-\chi}\sqrt{\frac{2}{\pi}}$. The results of temperature jump coefficient ζ_TJ for Maxwell's molecules are shown in Fig. (5.5). Here, we compare the temperature jump coefficient obtained from the Boltzmann equation with those obtained from the R13 equations with kinetic boundary conditions (5.19) and the phenomenological boundary conditions (4.38). As we can see from the figure, the R13 equations with kinetic boundary conditions yield about 10% smaller value for the ζ_TJ, which can be corrected by introducing a correction factor $\tau^* = 0.9960 - 0.1195\chi$. In conclusion, we can say that with the phenomenological corrections, the R13 equations indeed yield a good agreement with solutions of the Boltzmann equation. However,

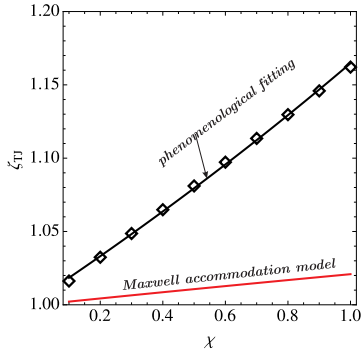

Figure 5.5: Comparison of temperature jump coefficient ζ_{TJ} for Maxwell molecules, Boltzmann solutions [59] (denoted by symbols), R13 equations with Maxwell accommodation boundary conditions and R13 equations with phenomenological boundary conditions.

this fitting of τ^* is only possible in simple cases, and for linear problems. For the remainder of this thesis, unless otherwise specified, we shall only consider Maxwell accommodation boundary conditions.

Chapter 6

Nonlinear 1D problems

For most practical situations the differential equations do not have analytic solutions, so numerical schemes must be used to find approximate solutions. Many basic numerical solution schemes for partial differential equations can be found in the literature [22, 20, 110, 54].

The R13 equations in 1D geometry has been presented in Sec. 5.1. In this chapter, these equations are employed to investigate rarefaction effects in parallel flow geometries. The numerical results obtained will be compared with the direct simulation Monte Carlo simulations. The simulation results in this chapter are based on a finite difference numerical scheme for the R13 equations, as formulated in [118]. More sophisticated variations and extensions of the numerical schemes will be presented later.

6.1 Numerical method

The R13–moment equations given by Eqs. (5.1), and Eqs. (5.4a)–(5.7d) include fourteen variables $U = \{\rho\,,\, v_x,\, \theta,\, \sigma_{xy},\, \sigma_{xx},\, \sigma_{yy},\, q_x,\, q_y,\, m_{xxy},\, m_{xyy},\, m_{yyy},\, R_{xy},\, R_{yy},\, \Delta\}$, all vary only with respect to $y \in [a,\ b]$. The boundary conditions (4.13) are prescribed at the boundaries. Moreover, the steady flow setting gives rise to one additional condition. In total, the mass between the walls should equate to a given value M_0, i.e.,

$$\int_a^b \rho dy = M_0. \tag{6.1}$$

As further reduction, the density gradient in (5.4a)–(5.7d) is replaced using the y-momentum equation (5.1b). Thus, ρ can be removed from the variables list U. The

resulting equations, after straightforward manipulations, can be written as a system of first order differential equations of the form [118]

$$\mathcal{A}(U)\frac{\partial U}{\partial y} = -\mathcal{P}(U)U + g. \tag{6.2}$$

On a computational domain $y \in [a,\ b]$, at which the solution is to be approximated, $U : \mathbb{R} \longmapsto \mathbb{R}^{13}$ is the dependent variable vector, $\mathcal{A} : \mathbb{R}^{13} \longmapsto \mathbb{R}^{13} \times \mathbb{R}^{13}$ and $\mathcal{P} : \mathbb{R}^{13} \longmapsto \mathbb{R}^{13} \times \mathbb{R}^{13}$ are the matrices of coefficients. The boundary conditions (4.13) can also be written in matrix form, as [118]

$$U|_{y=a} = \mathcal{Y}U|_{y=a} + \mathcal{Y}^w|_{y=a}, \text{ and} \quad U|_{y=b} = \mathcal{Y}U|_{y=b} + \mathcal{Y}^w|_{y=b}\ , \tag{6.3}$$

where $\mathcal{Y} : \mathbb{R}^{13} \longmapsto \mathbb{R}^{13} \times \mathbb{R}^{13}$, $\mathcal{Y} : \mathbb{R}^{13} \longmapsto \mathbb{R}^{13}$ and the vector $\mathcal{Y}^w$ in (6.3) contains the boundary properties, v^w, θ^w, χ.

In order to effect a finite difference approximation to this boundary value problem, one begins by introducing a uniform mesh consisting of N nodes

$$y_i = a + i\Delta y \quad \text{with} \quad \Delta y = \frac{b-a}{N+1},$$

where $a = y_0$ and $b = y_{N+1}$.

By employing the central difference approximation to the derivative appearing in the differential equation (6.2), one obtains

$$\mathcal{A}_i\frac{U_{i+1} - U_{i-1}}{2\Delta y} = -\mathcal{P}_iU_i + g \quad \text{for} \quad 1 \le i \le N, \tag{6.4}$$

where the error in the approximation is proportional to $\mathcal{O}(\Delta y^2)$. The boundary conditions can be implemented based on (6.3), using the values extrapolated from the interior points, as

$$U_0 = \mathcal{Y}U_0^* + \mathcal{Y}^w, \tag{6.5}$$

$$U_{N+1} = \mathcal{Y}U_{N+1}^* + \mathcal{Y}^w, \tag{6.6}$$

where

$$U_0^* = 3U_1 - 3U_2 - U_3, \text{ and} \quad U_{N+1}^* = 3U_N - 3U_{N-1} - U_{N-2}.$$

Replacing U_0 and U_{N+1} in the equation (6.4) from (6.5−6.6), and rearranging terms,

we get

$$
\begin{aligned}
&-\tfrac{1}{2}\mathcal{A}_i U_{i-1} + \Delta y \mathcal{P}_i U_i + \tfrac{1}{2}\mathcal{A}_i U_{i+1} = \Delta y g && : 2 \le i \le N-1, \\
&\text{and} \\
&\left[\Delta y \mathcal{P}_1 - \tfrac{3}{2}\mathcal{A}_1 \mathcal{Y}\right] U_1 \quad + \tfrac{1}{2}\left[\mathcal{A}_1 \mathcal{Y}\right] U_3 \\
&\qquad + \left[\tfrac{1}{2}\mathcal{A}_1 + \tfrac{3}{2}\mathcal{A}_1 \mathcal{Y}\right] U_2 \qquad = \Delta y g + \tfrac{1}{2}\mathcal{A}_1 \mathcal{Y}^w && : i = 1, \\
&\left[\Delta y \mathcal{P}_N + \tfrac{3}{2}\mathcal{A}_N \mathcal{Y}\right] U_N - \tfrac{1}{2}\left[\mathcal{A}_N \mathcal{Y}\right] U_{N-2} \\
&\qquad - \left[\tfrac{1}{2}\mathcal{A}_N + \tfrac{3}{2}\mathcal{A}_N \mathcal{Y}\right] U_{N-1} = \Delta y g - \tfrac{1}{2}\mathcal{A}_N \mathcal{Y}^w && : i = N.
\end{aligned}
$$

Combining all U_i into the vector $X = \{U_i\}_{1 \le i \le N}$, we can write the above equations in a compact matrix form,

$$\mathbf{M}(X)\, X = \mathbf{b}. \tag{6.7}$$

Equation (6.7) is non-linear in the discretized variable vector X and therefore an iterative scheme must be used to solve it, for this we used a quasi-minimal-residual (QMR) algorithm in Matlab.

The nonlinear terms and ρ were substituted successively with their updated values. Note that the density appears in the matrix $\mathbf{M}$ as a parameter and has to be recomputed in each iteration from the integrated momentum balance equation (5.1b) as

$$\rho = \frac{C_1 - \sigma_{yy}}{\theta},$$

where C_1 is the constant of integration obtained from equation (6.1).

The linear R13 system is solved in first iteration by choosing the reference equilibrium state as the starting value. The solution was considered to be fully converged when the maximum absolute values of the dependent variables at any node from iteration to iteration are smaller than a prescribed value, chosen as 10^{-7}. This numerical scheme (in 2D) will be presented in the next chapter with more details.

In next few sections, numerical solutions for the one dimensional non-linear R13 and the NSF equations are investigated. Flows in planar Couette geometry will be considered first; we compare the accuracy of the R13 equations with available DSMC data in the literature.

6.2 Planar Couette flow

We consider steady state flow confined between two infinite planar parallel plates at constant distance L from each other, see Fig. (6.1). The walls are located on $y = \pm L/2$, move with velocities $v^W(\pm L/2) = \pm v_w$, and are maintained at constant temperatures $\theta^W(\pm L/2) = \theta_0$. Furthermore, velocity, temperature, and all other flow parameters are assumed to be independent of the flow direction x.

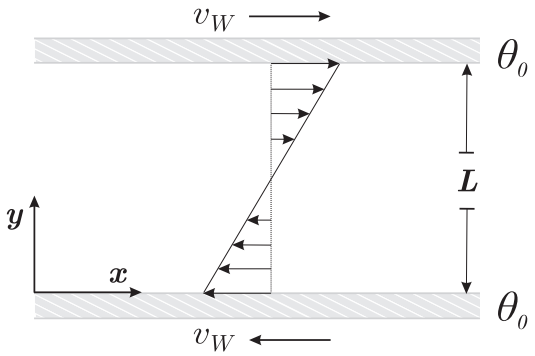

Figure 6.1: Schematic of planar Couette flow configuration.

In [108], the authors obtained solutions of the semi-linearized R13 equations in planar geometry, with semi-linearized boundary conditions. The linearized equations lead to analytical solutions for Couette and Poiseuille flows. However, their approach was limited to small velocities $v_w \approx 0.4$. Torrilhon and Struchtrup [118] solved the non-linear R13 equations for higher velocities. To achieve this, a transformation (similar to the transformation discussed earlier in Sec. 3.2.3) of non-linear equations was proposed, where pressure gradients in (3.30) were replaced by means of the steady state 1D momentum balance equations. The results obtained demonstrated the usefulness of their approach in the 1D case, however, extension of their transformation in more general settings remained unclear. In subsequent sections, we shall show the solutions of the R13–moment equations derived in Sec. 3.2.3; these equations are valid for arbitrary geometries.

Before providing the numerical solutions for the planar Couette flow, we shall show the accuracy and order of convergence for the numerical scheme.

6.2.1 Convergence and grid independency test

The accuracy of the numerical results depends on the mesh size Δy. Ideally, we would like a solution that does not change significantly when more grid points are introduced. It is done formally by successively refining the mesh until the numerical solution does not change perceptibly. More precisely, we define the $L^{\infty}-$error as

$$E_2(\psi) = \max_i |\psi_i^{(\Delta y)} - \psi_i^{(ref)}| \ , \tag{6.8}$$

where ψ is the quantity of interest, $\psi_i^{(\Delta y)}$ is the solution obtained using a mesh of size Δy, and $\psi_i^{(ref)}$ is the exact solution. However, as the exact solution is unknown, we shall compare the obtained results with the simulations performed on very fine grids. We use the discretization at $N = 400$ as the reference solution.

Figure 6.2 illustrates the convergence of the numerical scheme for given values of Kn = 0.05, 0.5 in velocity v_x, shear stress σ_{xy} and temperature θ, for small wall velocity $v_w = 0.4195$. The quantities plotted are the errors, $E_2(v_x)$, $E_2(\sigma_{xy})$, and $E_2(\theta)$ as described in (6.8), for Kn = 0.05 (Fig. 6.2 (a)) and 0.5 (Fig. 6.2 (b)). The scheme exhibits an approximately second-order convergence rate in the L^{∞}-norm. The convergence rate reduces as the Knudsen number increases. Nevertheless, for the range of the Knudsen number considered, $10^{-2} \leq \text{Kn} \leq 1$, the numerical scheme shows an average convergence rate between 1.87 to 2.1. Figure 6.3 shows the convergence

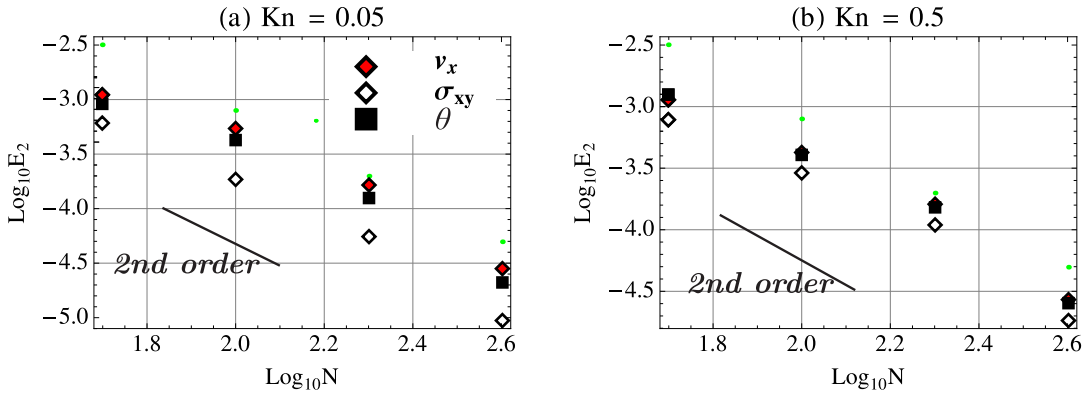

Figure 6.2: Empirical convergence of the numerical scheme: $\log_{10} - \log_{10}$ plots of the error estimates for velocity $E_2(v_x)$, shear stress $E_2(\sigma_{xy})$ and temperature $E_2(\theta)$, with respect to the number of grid points N. Wall velocity $v_w = 0.4195$ and Kn = 0.05 (left), 0.5 (right).

for a relatively high wall velocity $v_w = 1.2586$. In this case, the numerical scheme

shows an average convergence rate of 1.83 and 1.91 for Kn 0.05 and 0.5, respectively.

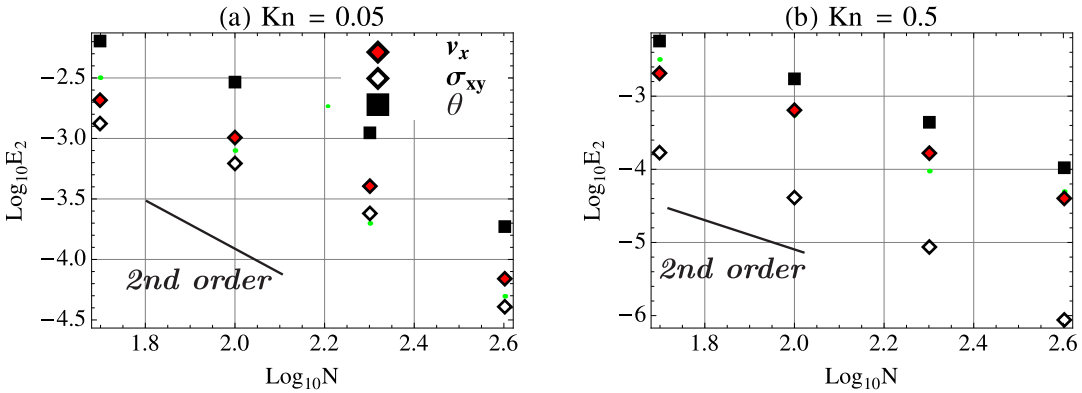

Figure 6.3: Empirical convergence of the numerical scheme: $\log_{10} - \log_{10}$ plots of the error estimates for velocity $E_2(v_x)$, shear stress $E_2(\sigma_{xy})$ and temperature $E_2(\theta)$, with respect to the number of grid points N. Wall velocity $v_w = 1.2586$ and Kn $= 0.05$ (left), 0.5 (right).

6.2.2 Results and discussions

Figure 6.4 presents the results obtained from the R13, NSF and R10 equations for velocity, temperature, shear stress, normal stress, tangential heat flux, and normal heat flux at Kn $= 0.025$ and $v_w\,(\pm 0.5) = \pm 0.4195$. The walls are considered to be fully diffusive, therefore, $\chi = 1$. Results obtained using the R13 equations (orange curves), R10 equations (dashed dotted curve) and NSF equations (blue thin curve) are compared with DSMC (symbols) solutions [83]. As illustrated, at this value of the Knudsen number, for hydrodynamic variables, i.e., velocity v_x, temperature θ, shear stress σ_{xy}, and normal heat flux q_x, all macroscopic models give similar results, within 2% of DSMC predictions. However, among all three models, R13 equations give comparatively better results. The normal stress σ_{yy}, and the tangential heat flux q_x, are non-hydrodynamic quantities and they both vanish in the NSF theory. Thus their non-zero values in Fig. 6.4 (d) and Fig. (6.4 (e)), as predicted by the R13 and R10, are non-linear plus the Knudsen layers effects. The R10 equations have no Knudsen layers, thus non-zero values for these quantities in the R10 solutions are solely due to non-linear contributions. The Navier-Stokes-Fourier equations, on the other hand, can neither describe the Knudsen boundary layers nor the nonlinear effects in σ_{yy} and q_x.

For Knudsen numbers 0.1, as shown in Fig. 6.5 (d) and Fig. 6.5 (e), the Knudsen layers

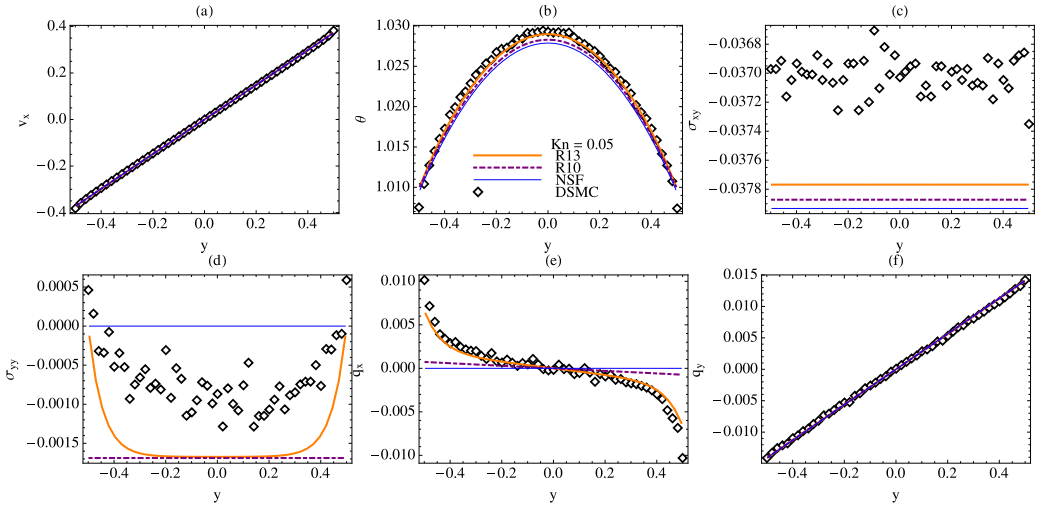

Figure 6.4: Variation of the (a) velocity v_x, (b) temperature θ, (c) shear stress σ_{xy}, (d) normal stress σ_{yy}, (e) tangential heat flux q_x, and (f) normal heat flux q_y along $y-$direction for Kn $= 0.05$ and $v^w(\pm) = \pm 100 m/s$. Results obtained using the R13 equations, R10 equations and NSF equations are compared with DSMC solutions.

become more pronounced. The R13 theory gives satisfying description of Knudsen layers, which the Navier-Stokes-Fourier equations are not able to capture. The effects of the Knudsen layers on velocity and temperature are also visible in Fig. 6.5 (a) and Fig. 6.5 (b), respectively, where curves show a small curvature near the boundaries. Furthermore, the shear stress σ_{xy}, in Fig. 6.5 (c), as predicted by DSMC simulations is higher than NSF, R10 and R13 equations by about 4.2%, 3.7%, 3%, respectively. Although not shown here, in the linear case the correction in slip and jump coefficients using phenomenological boundary conditions discussed in the last chapter, brings curves closer to DSMC solutions.

Figure 6.6 shows the variation of the velocity v_x, temperature θ, shear stress σ_{xy}, normal stress σ_{yy}, tangential heat flux q_x and normal heat flux q_y for Knudsen number Kn $= 0.1$ and wall velocities $v^w(\pm) = \pm 1.2586$. Again, results obtained using the R13 equations, R10 equations and NSF equations are compared with DSMC solutions. Interestingly, in this case the shear stress given by R10 equations is in excellent match with DSMC, however for other fields, among these three sets of equations, the R13 equations give the best results followed by the R10 equations. The quality of the R13 results must be addressed to its third–order accuracy and the contribution of the Knudsen layers.

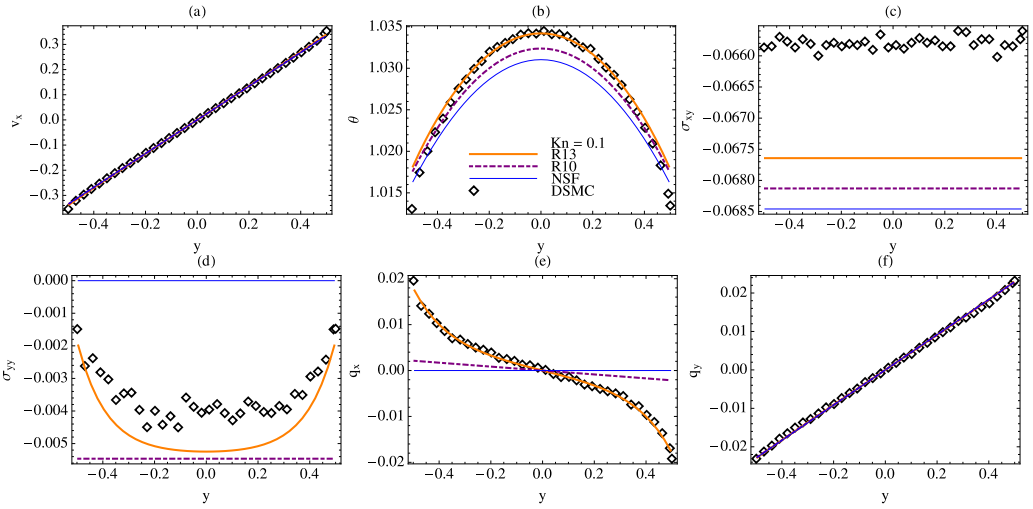

Figure 6.5: Variation of the (a) velocity v_x, (b) temperature θ, (c) shear stress σ_{xy}, (d) normal stress σ_{yy}, (e) tangential heat flux q_x, and (f) normal heat flux q_y along $y-$direction for Kn $= 0.1$ and $v^w(\pm) = \pm 100 m/s$. Results obtained using the R13 equations, R10 equations and NSF equations are compared with DSMC solutions.

6.3 Cylindrical Couette flow

Next, we consider a rarefied gas confined between two coaxial cylinders with radii R_1 and R_2 where the axes of the cylinders coincide with the $z-$axis. The temperatures of the cylinders are the same and equal to $\theta_0 = 1$. The inner cylinder is rotating around the z-axis with a constant wall velocity $v_\phi = 1/\sqrt{2}$, whereas the outer cylinder is at rest, see Fig. (6.7).

Microscale cylindrical Couette flows are frequently encountered in many engineering applications, for example in miniaturized turbomachinery designs where work transfer between the rotor assembly of a microturbine and the fluid is desired [25]. Rarefied gas flows in cylindrical geometries have been vastly investigated using different methods [86, 87, 3, 91, 92, 109, 127], and many more. In Refs. [12, 107], using linearized equations, the authors show that the R13–moment equations predict a circumferential non–Fourier heat flow and non–Newtonian stress components which are pure rarefaction effects.

The transformation of the R13 equations to a cylindrical geometry and a detailed linear analysis on cylindrical Couette flows can be found in [12, 107]. Here, we shall investigate the behavior of the gas numerically on the basis of the NSF equations and the R13–moment equations, and compare our results with DSMC.

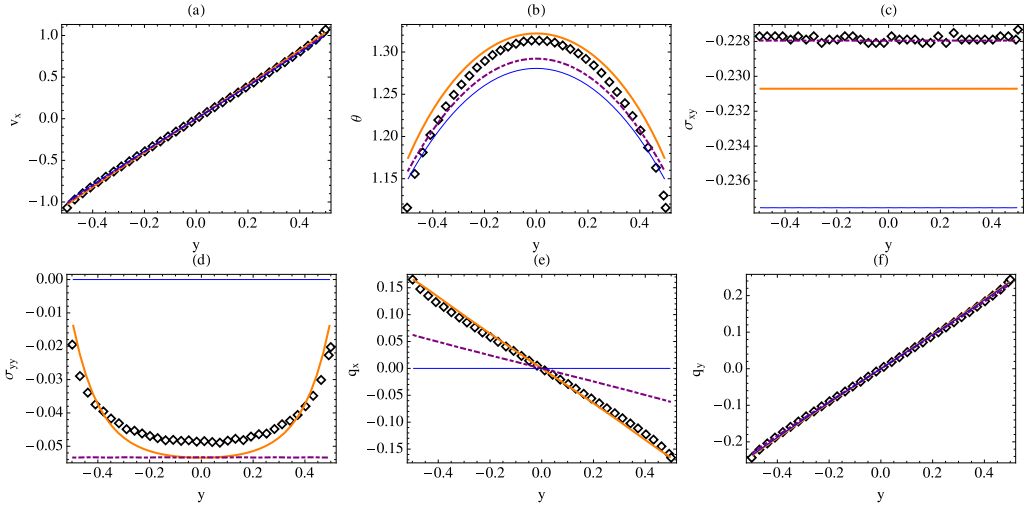

Figure 6.6: Variation of the (a) velocity v_x, (b) temperature θ, (c) shear stress σ_{xy} , (d) normal stress σ_{yy}, (e) tangential heat flux q_x, and (f) normal heat flux q_y along $y-$direction for Kn $= 0.1$ and $v^w(\pm) = \pm 600 m/s$. Results obtained using the R13 equations, R10 equations and NSF equations are compared with DSMC solutions.

For these simulations, the radius of the inner cylinder is taken as the reference length scale, i.e., the length is made dimensionless based on the radius of the inner cylinder R_1, and $R_2 = 2R_1$. We shall compare our results with those given in [3],

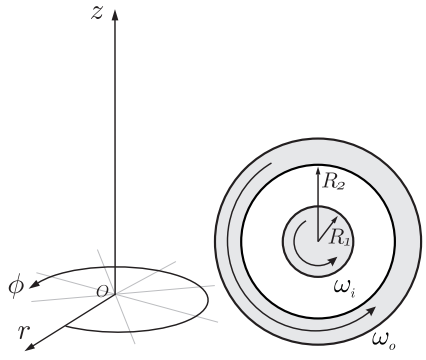

Figure 6.7: Schematic diagram of a cylindrical Couette flow.

where data used in this comparison are digitized from FIG. 2 of [3].

6.3.1 Results and discussions

In Fig. 6.8 the radial velocity v_ϕ is shown for various values of the accommodation coefficient χ and Kn = 0.016, 0.039 and 0.078. Note that the Knudsen numbers indicated in Fig. 6.8 correspond to the Knudsen number $\widetilde{\mathrm{Kn}}$ used in [3], which is related to our definition by $\mathrm{Kn} = \widetilde{\mathrm{Kn}} 5\sqrt{2\pi}/16$. We are comparing the results obtained from the R13 equations (orange curve) and the NSF equations (blue curve) with DSMC data from [3].

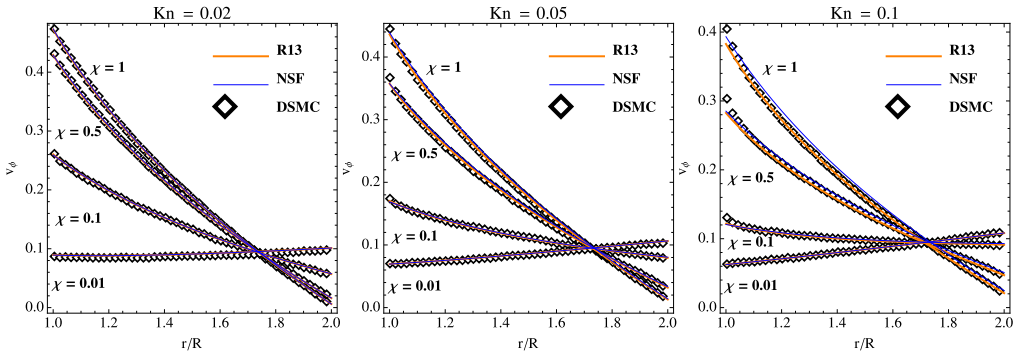

Figure 6.8: Radial velocity profiles are shown for various values of accommodation coefficient χ and for $\widetilde{\mathrm{Kn}} = 0.02$, 0.05, and 0.1. Symbols are DSMC data and lines are the results from the macroscopic models. The DSMC data are digitized from Aoki et al. [3].

For the smaller Knudsen number, Kn = 0.016, there is no visible difference between all theories. For Kn = 0.078, where the rarefaction effects are comparatively stronger, some difference to the DSMC results is observed, especially near the boundaries, where Knudsen layers take effects. Therefore, the R13 equations give a better description and provide more curvature near the walls. Furthermore, in comparison to the linear study done in [12], the nonlinear results presented here give better agreement with the DSMC solutions.

In Fig. 6.8, it is interesting to note that as χ becomes smaller the velocity profiles become inverted, i.e., the velocity of the gas near the stationary cylinder wall becomes larger than the gas near the rotating wall. This nonintuitive behavior has been studied in the literature, for example in Einzel et al. [28], Tibbs et al. [109], Aoki et al. [3]. This phenomenon is the effect of curvature on the slip length [28], hence it is not observed in planar Couette flows.

Profiles for stress tensor σ_{xy}, tangential heat flux q_ϕ, and radial heat flux q_r are

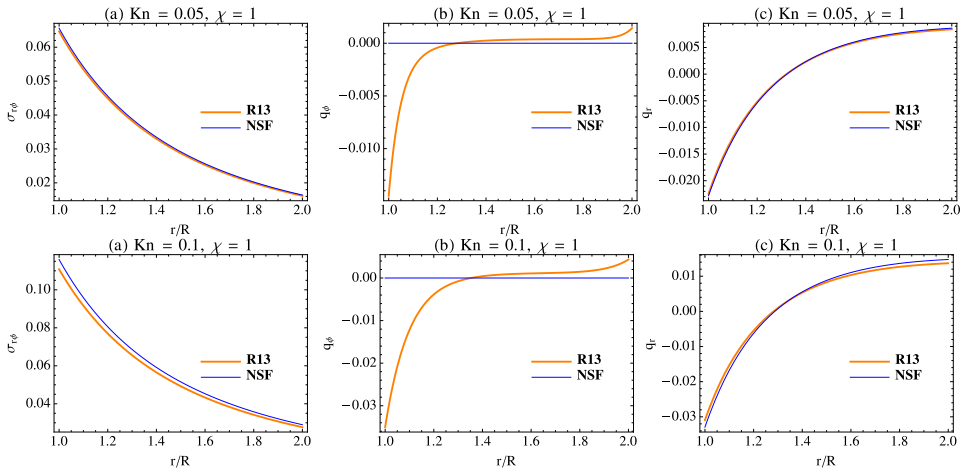

Figure 6.9: Profiles of (a) stress tensor σ_{xy}, (b) tangential heat flux q_ϕ, and (c) radial heat flux q_r. Blue lines represent NSF results and continuous orange line represents R13 results.

shown in Fig. 6.9 (a), (b) and (c), respectively. The results obtained from NSF (blue curve) and R13 equations (orange curve) are compared, for fully diffusive walls $\chi = 1$ and Kn $= 0.05$ (top row) and 0.1 (bottom row). Both R13 and NSF theories predicts very close shear stress and radial heat fluxes, however, the tangential heat flux q_ϕ predicted by NSF is zero, as there is no temperature gradient in $\phi-$direction.

6.4 Heat transfer between parallel heated plates

In the last two sections we considered the shear driven flows. In the present section we consider the heat transfer between two parallel plates of infinite lengths. The plates are stationary and the temperatures of lower and upper plates are $\theta_0 - \Delta\theta$ and $\theta_0 + \Delta\theta$, respectively. Here only purely diffuse boundary conditions ($\chi = 1$) are applied for both plates.

6.4.1 Results and discussions

The temperature profiles, predicted from R13, R10, NSF, and R21[1] [67] equations, at different Knudsen numbers are shown in Fig. 6.10 in comparison with the DSMC data [30]. The calculations are carried out for Knudsen numbers Kn $= 0.0379, 0.1262$

[1]see Appendix C for the R21 equations and the boundary conditions

and 0.3786, calculated at the reference temperature $\theta_0 = 273$K and different reference pressures $p_0 = 133.3$, 40, 13.33 Pa, respectively. The temperature difference between the plates is $\Delta\theta = 10/273$. The agreement between numerical results given

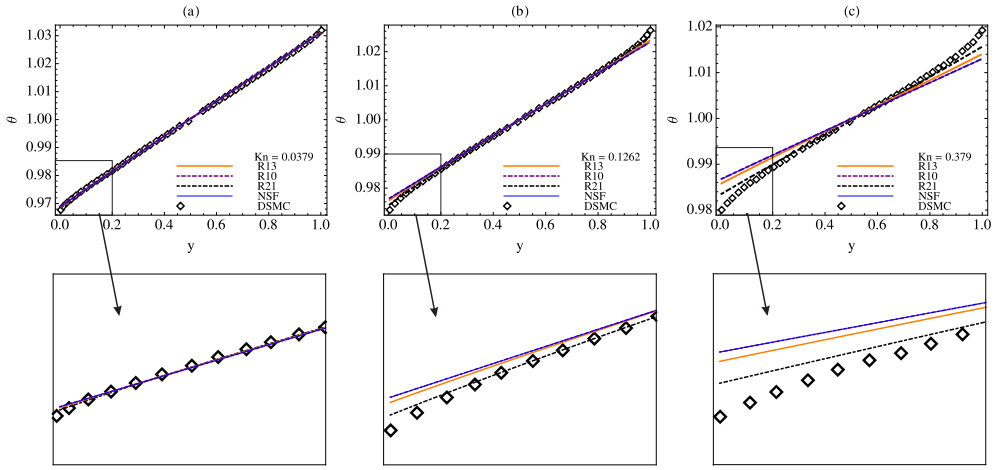

Figure 6.10: Temperature distribution for stationary heat transfer between two plates: comparison between the NSF, R10, R13, R21 and DSMC theories for a small temperature difference $\Delta\theta = 0.0366$. The insets in figures are the magnification of the region close to left boundary, where the effects of Knudsen layers are observed.

by extended thermodynamic model, including NSF, is good for Kn = 0.0379, but when the Kn number increases the discrepancy between the numerical results and the DSMC increases, especially near the walls. As the Knudsen number increases to Kn = 0.3786, and rarefaction effects dominate, all tested models fail, which can be attributed to their inability to properly describe Knudsen layers. However, among these macroscopic models, the R21–moment equations provide best results followed by R13–moment equations. The calculations of the heat flux are also carried out and plotted in Fig. (6.11) for $\Delta\theta = 0.14$ and the accommodation coefficient $\chi = 0.826$. The plotted results are for normalized heat flux, defined as $\hat{q}_y = q_y/q_{\rm FM}$; where $q_{\rm FM}$ is the normal heat flux in the free molecular regime given as [34]

$$q_{\rm FM} = -\frac{\chi}{2-\chi}\frac{2\Delta\theta}{\sqrt{\pi}}.$$

In Fig. (6.11), we compare our results with test case considered in [34]. We observe that predictions for the normalized heat flux of the R13 equations are less than 5% of one predicted by HS and ES-BGK models [34]. The results computed from the R21

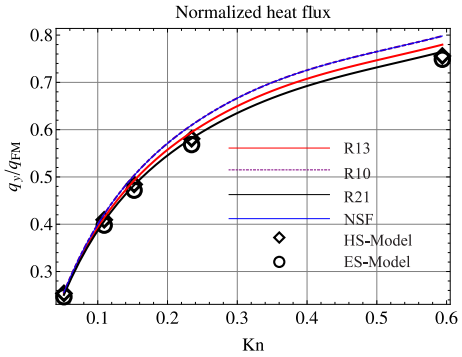

Figure 6.11: Normalized heat flux q_y/q_{FM}: comparison among different models.

equations are a little better than those of the R13 equations.

Chapter 7

Flow in a lid driven cavity

The lid driven cavity is a classical benchmark problem in fluid mechanics, that, in spite of its simple geometry, exhibits most of the features of more complicated process described by the Boltzmann equation. Many researchers have investigated the rarefied gas flows in the isothermal lid driven cavity by solving kinetic equation using direct methods [74, 121], the DSMC methods [45, 82], among others. This problem was also considered in [67, 45] using variants of the regularized moment method.

Below we shall introduce, and use, a numerical simulation method for the two dimensional R13 equations which is computationally economical and provides reliable solutions in good agreement to solutions of the Boltzmann equation. The numerical method is based on the finite difference method described in the last chapter by using a straightforward extension to two dimensions. The proposed finite difference scheme allows efficient solutions for 2D boundary value problems (BVP) of the R13 equations. Special care is taken to incorporate the non-standard boundary condition and total mass constraint. The lid-driven cavity problem will serve as two-dimensional test case.

We shall compare numerical solutions of the driven cavity problem for rarefied gases based on the R13 equations and the NSF equations with slip and jump boundary conditions to kinetic theory solutions. The purpose here is to investigate the effectiveness of the R13–moment equations at moderate Knudsen numbers. Two cases of the lid driven cavity problem are investigated: (1) classic case of the isothermal cavity (2) lid driven cavity with mixed (adiabatic-isothermal) boundary conditions.

7.1 Lid driven cavity with isothermal walls

We consider a monatomic rarefied gas contained in a square enclosure with length L, see Fig. (7.1). The boundaries at $x = 0$, $x = 1$, and $y = 0$ are stationary, while the upper boundary at $y = 1$ is in motion with a constant horizontal velocity v_{lid}. All walls are considered isothermal with a temperature $T_0 = 273\,\mathrm{K}$. Boundary conditions at each wall are described by the Maxwell accommodation model with full accommodation, i.e., $\chi = 1$, as described earlier in Sec. 4.1. The lid-velocity is chosen such that $v_{lid}/\sqrt{RT_0} \ll 1$ and the domain is considered as unbounded in the z-direction and the effects in that direction are neglected.

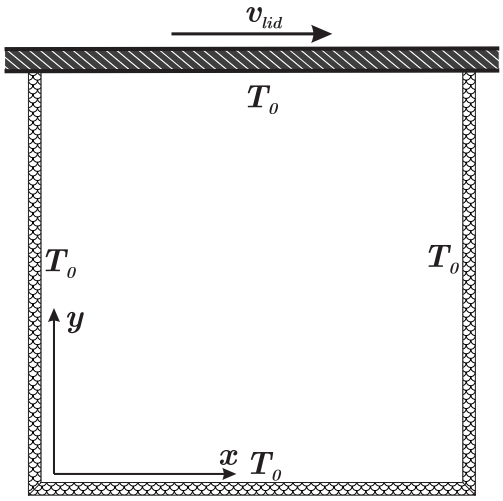

Figure 7.1: Schematic of the isothermal lid driven cavity.

For this problem Sharipov and co-workers solved kinetic equation for various values of the rarefaction parameter $\delta = \sqrt{\frac{1}{2}}\frac{1}{\mathrm{Kn}}$ [121]. The DSMC solutions to this problem are presented in [45]. These results will serve us for comparison.

7.2 Numerical Method

For preparation we write the dimensionless partial differential equations (3.25–3.27) and (3.31) as a first order system,

$$\mathcal{A}(U)\frac{\partial U}{\partial x} + \mathcal{B}(U)\frac{\partial U}{\partial y} + \frac{1}{\mathrm{Kn}}P(U)\,U = 0. \tag{7.1}$$

Here,

$$U = [\rho, v_x, v_y, \theta, q_x, q_y, \sigma_{xx}, \sigma_{xy}, \sigma_{yy}, R_{xx}, R_{xy}, R_{yy}, m_{xxx}, m_{xyy}, m_{xxy}, m_{yyy}, \Delta]\,,$$

is the vector of field variables, and $\mathcal{A}(U)$ and $\mathcal{B}(U)$ are the coefficient matrices in x and y-directions, respectively. The matrix $P(U)$ is the production matrix. Since we only consider steady state flow, $\frac{\partial}{\partial t} \equiv 0$ in equations (3.25–3.27). The matrices $\mathcal{A}(U)$, $\mathcal{B}(U)$ and $P(U)$ are presented in Appendix A.

We discretize the spatial domain using $N \times M$ grid points as $x_i = i\Delta x$ and $y_j = j\Delta y$, where $i = 0, N+1$ and $j = 0, M+1$ are the boundary nodes. Using this discretization, equation (7.1) assumes the form

$$\mathcal{A}_{i,j}\frac{\partial U_{i,j}}{\partial x} + \mathcal{B}_{i,j}\frac{\partial U_{i,j}}{\partial y} + \frac{1}{\mathrm{Kn}}P_{i,j}U_{i,j} = 0 \quad \forall \quad (i,j) \in [1,N] \times [1,M]\,, \tag{7.2}$$

where $U_{i,j} = U(x_i, y_j)$, $\mathcal{A}_{i,j} = \mathcal{A}(U_{i,j})$ etc.

The boundary conditions (4.13a-4.13f) are incorporated in matrix form, and linear extrapolation is used for boundary nodes to obtain

$$U_{0,j} = \mathcal{X}^{+}_{1,j}\ (2U_{1,j} - U_{2,j}) + \mathcal{X}^{d+}_{1,j}, \tag{7.3a}$$

$$U_{N+1,j} = \mathcal{X}^{-}_{N,j}\ (2U_{N,j} - U_{N-1,j}) + \mathcal{X}^{d-}_{N,j}, \quad \forall\ j \in [1,M]\,, \tag{7.3b}$$

$$U_{i,0} = \mathcal{Y}^{+}_{i,1}\ (2U_{i,1} - U_{i,2}) + \mathcal{Y}^{d+}_{i,1}, \tag{7.4a}$$

$$U_{i,M+1} = \mathcal{Y}^{-}_{i,j_{m+1}}\ (2U_{i,M} - U_{i,M-1}) + \mathcal{Y}^{d-}_{i,M}, \quad \forall\ i \in [1,N]\,, \tag{7.4b}$$

for x-walls (wall normal pointing in the x direction) and y-walls (wall normal pointing in the y direction), respectively. Here, the matrix $\mathcal{X}_{1j}$ (or $\mathcal{Y}_{1j}$), is the corresponding coefficient matrix of field variables U in (4.13a-4.13f) for x-walls (or y-walls), and the vector $\mathcal{X}^{d}_{1j}$ (or $\mathcal{Y}^{d}_{1j}$) consists of inhomogenities due to wall properties $\left(\theta^W, v^W\right)$ on x–walls (or y–walls), refer to the Appendix A for the explicit expressions of $\mathcal{X}^{\pm}_{1,j}$. The superscripts " $+$ " and " $-$ ", denote the positive and negative directions of the wall normal, i.e., $n_x = \pm 1$ (or $n_y = \pm 1$), respectively. In the boundary matrices, $\mathcal{X}^{\pm}_{1,j}$, only the rows for the odd variables give boundary conditions, while the other rows give identities. For example, in x-direction, v_x , q_x , σ_{xy} , R_{xy} , m_{xxx} , m_{xyy} are given by their respective boundary conditions.

By replacing the derivatives in equation (7.2) by a central difference scheme, we

get

$$\mathcal{A}_{ij}\frac{U_{i+1,j}}{2\Delta x}-\mathcal{A}_{ij}\frac{U_{i-1,,j}}{2\Delta x}+\mathcal{B}_{ij}\frac{U_{i,,j+1}}{2\Delta y}-\mathcal{B}_{ij}\frac{U_{i,j-1}}{2\Delta y}+\frac{1}{\mathrm{Kn}}P_{i,j}U_{i,j}=0$$
$$\forall\ (i,j)\in[2,N-1]\times[2,M-1]\,. \quad (7.5)$$

Combining Eq. (7.5) with Eq. (7.3a), we obtain the equation for the left wall ($i=1$):

$$\left(\frac{1}{\mathrm{Kn}}P_{1,j}-\frac{1}{\Delta x}\mathcal{A}_{1,j}\mathcal{X}^{+}_{1,j}\right)U_{1,j}+\frac{1}{2\Delta x}\mathcal{A}_{1,j}\left(I+\mathcal{X}^{+}_{1j}\right)U_{2,j}+$$
$$+\mathcal{B}_{1,j}\frac{U_{1,j+1}}{2\Delta y}-\mathcal{B}_{1,j}\frac{U_{1,j-1}}{2\Delta y}=\frac{1}{2\Delta x}\mathcal{A}_{1,j}\mathcal{X}^{+d}_{1j}\quad\forall\ j\in[2,M-1]\,. \quad (7.6)$$

Correspondingly, for the right wall ($i=N$), we combine the Eq. (7.5) with Eq. (7.3b), to get

$$\left(\frac{1}{\mathrm{Kn}}P_{N,j}+\frac{1}{\Delta x}\mathcal{A}_{N,j}\mathcal{X}^{-}_{N,j}\right)U_{N,j}-\frac{1}{2\Delta x}\mathcal{A}_{N,j}\left(I+\mathcal{X}^{-}_{N,j}\right)U_{N-1,j}+$$
$$+\mathcal{B}_{N,j}\frac{U_{N,j+1}}{2\Delta y}-\mathcal{B}_{N,j}\frac{U_{N,j-1}}{2\Delta y}=-\frac{1}{2\Delta x}\mathcal{A}_{N,j}\mathcal{X}^{-d}_{N,j}\quad\forall\ j\in[2,M-1]\,. \quad (7.7)$$

A similar treatment is used for the lower ($j=0$) and the upper wall ($j=M$). For the lower-left corner ($i=1$, $j=1$), we have

$$\left(\frac{1}{\mathrm{Kn}}P_{11}-\frac{1}{\Delta x}\mathcal{A}_{11}\mathcal{X}^{+}_{11}-\frac{1}{\Delta y}\mathcal{B}_{11}\mathcal{Y}^{+}_{11}\right)U_{1,1}+\frac{1}{2\Delta x}\mathcal{A}_{11}\left(I+\mathcal{X}^{+}_{11}\right)U_{2,1}+$$
$$+\frac{1}{2\Delta y}\mathcal{B}_{11}\left(I+\mathcal{Y}^{+}_{11}\right)U_{1,2}=\frac{1}{2\Delta x}\mathcal{A}_{11}\ \mathcal{X}^{+d}_{11}+\frac{1}{2\Delta y}\mathcal{B}_{11}\ \mathcal{Y}^{+d}_{11}. \quad (7.8)$$

The other corners are dealt analogously.

Combining all discrete values into the vector $X=\{U_{i,j}\}_{(i,j)\in[1,N]\times[1,M]}$, we can write the above equations in compact matrix form:

$$\mathcal{M}\,(X)\ \ X=\mathfrak{b}(X). \quad (7.9)$$

7.2.1 Non-local boundary condition

The total mass inside the cavity is conserved during the process. This gives one additional non-local boundary condition,

$$\int_{x=0}^{L}\int_{y=0}^{L} \varrho\,(x,y)\,dydx = M_0. \tag{7.10}$$

Problems involving non-local boundary conditions have been studied in many papers, see e. g., [24]. Here, we present an alternative approach.

Equation (7.9) is non-linear in the discretized variable vector X and therefore an iterative scheme can be used to solve it. To ensure the total mass constraint (7.10) at each iteration, the following strategy is proposed.

A detailed inspection of the matrix $\mathcal{M}\,(X)$ shows that it has a unique ($\forall\ X$) right null space of one dimension spanned by X^R, i.e., $\mathcal{M}\,(X)\,X^R = 0$. Existence of a null space implies that if X^p is some particular solution of Eq. (7.9), so is $X^p + \alpha X^R\ \forall \alpha \in \mathbb{R}$.

Computation (using Mathematica) of the null vector X^R shows that it has non-zero elements only for the local densities $\rho_{i,j}$. Therefore, the density ρ can only be computed up to a constant α, which needs to be determined using the total mass constraint (7.10).

The total mass constraint can be written in discrete form using the trapezoidal rule as

$$\sum_{r=1}^{N\cdot M} w_r X_r = M_0, \tag{7.11}$$

where w_r are the corresponding weight functions. Equation (7.11) allows to recast the system (7.9) as

$$\tilde{\mathcal{M}}\,(X)\,\tilde{X} = \tilde{\mathfrak{b}}(X), \tag{7.12}$$

where

$$\tilde{\mathcal{M}}\,(X) = \begin{bmatrix} 0 & \mathbf{w}^T \\ X^L & \mathcal{M}\,(X) \end{bmatrix}, \quad \tilde{X} = \begin{bmatrix} \alpha \\ X \end{bmatrix}, \quad \tilde{\mathfrak{b}}(X) = \begin{bmatrix} M_0 \\ \mathfrak{b}(X) \end{bmatrix}, \tag{7.13}$$

and X^L is the left null space of the matrix $\mathcal{M}\,(X)$.

It is obvious from the first row of the system (7.12) that any solution of (7.12) also satisfies the total mass constraint (7.11).

The following discussion will lead to the understanding of the second row. Let us assume that the system (7.9) has at least one solution. Then for all solutions X,

$$X^L \ \mathfrak{b}(X) = 0. \tag{7.14}$$

Further, any solution of (7.12) will also be a solution of (7.9), as shown below.

The second block of the system (7.12) reads

$$\alpha \, X^L + \mathcal{M}\,(X)\, X = \mathfrak{b}(X); \tag{7.15}$$

multiplication with the left null vector X^L gives

$$\alpha \, X^L \cdot X^L + X^L \cdot \mathcal{M}\,(X)\, X = X^L \ \mathfrak{b}(X). \tag{7.16}$$

Since X^L is a null vector of $\mathcal{M}$, this reduces to

$$\alpha \, X^L \cdot X^L = X^L \mathfrak{b}(X)\ .$$

With the solvability condition (7.14) and $X^L \cdot X^L \neq 0$, we find $\alpha = 0$, and thus (7.15) reduces to (7.9).

The non linear system (7.12) is solved for $\tilde{X} = (\alpha, X)$ by fixed point iterative scheme, where in each iteration the linear system of equations is solved using a quasi minimal residual (QMR) iterative scheme. As a starting value for the iteration, a global equilibrium state is used. Therefore, the linear R13 (or NSF) equations are solved in the initial iteration.

7.2.2 Algorithm

The solution of the system (7.12) is obtained iteratively in the following steps:

- Step 1:

  The values of the variables at all grid points are initialized as a global equilibrium state at rest, with global density $\rho_0 = p_0/\theta_0$ and global temperature θ_0; initially the values of all other fields are zero, thus

$$X^{(0)}_{i,j} = U^{(0)}_{i,j} = \Big[\rho_0 \quad 0 \quad 0 \quad \theta_0 \quad \mathbf{0} \in \mathbb{R}^{13}\Big]\,.$$

- Step 2:

  Equation (7.12) is solved with the iterative QMR solver, which solves: $\tilde{\mathcal{M}}\left(X^{(k)}\right)\tilde{X}^{(k+1)} = \tilde{\mathfrak{b}}(X^{(k)})$ for $\tilde{X}^{(k+1)}$.

- Step 3:

  If $\left\|X^{k+1} - X^{k}\right\|_1 \leq \epsilon$ holds, the computation is stopped, else Step 2 is performed again. We used $\epsilon = 10^{-6}$ $[\sim \mathcal{O}(\Delta x^3, \Delta y^3)]$. The discretization in the computational domain has been progressively refined to ensure the grid independence of the results.

7.2.3 Empirical order of convergence

The numerical error in the method can be estimated using the empirical order of convergence. The L_1-norm is used to calculate the error, which is defined as

$$||(\varrho^{Exact} - \varrho^{Num})||_1 = \Delta x \Delta y \sum_{i=1}^{N}\sum_{j=1}^{M} |\varrho_{ij}^{Exact} - \varrho_{ij}^{Num}|, \tag{7.17}$$

where the exact solution is approximated on a very refined mesh with 500×500 cells.

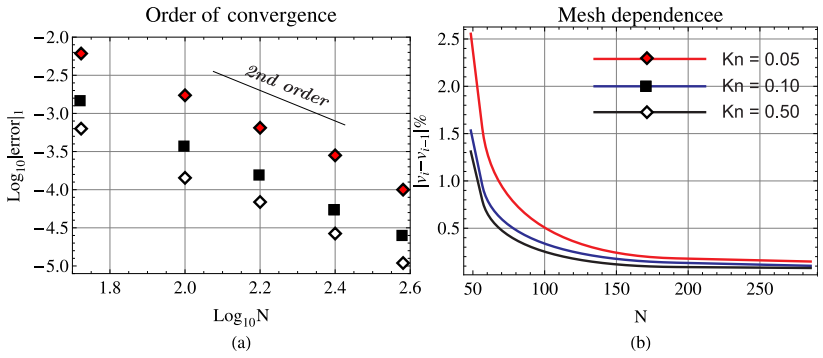

Figure 7.2: (a) Empirical order of convergence for velocity v_x, and (b) mesh dependence of the numerical solution for v_x along the lid, for Knudsen numbers Kn = 0.5 (black curves), 0.1 (blue curves), 0.05 (red curves).

Figure 7.2(a) shows the $\log_{10}$-$\log_{10}$ plots of the error estimates for dimensionless velocity with respect to the mesh size N, for Knudsen numbers Kn = 0.5, 0.1, and 0.05. These results were computed for the driven cavity with $v_{lid} = 50m/s$ on the

computational domain $[0,1] \times [0,1]$. Figure 7.2(a) shows an approximately second order convergence at all Knudsen numbers.

For determining an appropriate mesh configuration a grid independence test is conducted as well, where different meshes of size $N_i = 40$, 50, 75, 100, 200, 400 are tested. Relative percentage difference in dimensionless velocity ($\hat{v}_x = v_x/v_{lid}$) along the moving wall was monitored as the grid was refined successively. The results are plotted in Fig. 7.2(b), for Knudsen numbers Kn=0.5, 0.1 and 0.05. It is evident from Fig. 7.2(b) that the relative percentage change in dimensionless velocity between two successive grid sizes is less then 1% as the grid is refined beyond 75×75.

With our un-optimized Matlab code used on a standard quad core PC with a 75×75 grid, the solution of the non-linear R13 equations requires about 15 minutes, while the solution based upon the DSMC method takes days for a similar problem.

7.3 Results and discussion

In this section, numerical solutions for the isothermal lid-driven cavity are presented for the R13 equations and the NSF equations with first and second order boundary conditions, and compared with more accurate solutions obtained using DSMC [45][67] and IMM [121]. Most of the material presented here was published in [80].

7.3.1 One-dimensional profiles

The left and right parts of Fig. (7.3) show the profiles of the dimensionless vertical component of the velocity, v_y/v_{lid}, along the vertical centerline of the cavity, and the dimensionless horizontal component of the velocity, v_x/v_{lid}, along the horizontal line crossing the centre of the vortex, respectively, at different values of the Knudsen number Kn.

For small Knudsen numbers (1st and 2nd row of Fig. (7.3)) all models—the R13 equations and the NSF equations with first order boundary conditions (Section 4.1.3) and the second order boundary conditions (Section 4.1.4)—exhibit a good agreement with DSMC.

For the larger Knudsen number Kn = 0.4, the results are shown in the third row of Fig. (7.3). The NSF equations with first and second order boundary conditions have lost their validity completely, as they fail not only to describe the slip and the Knudsen layer at the wall, but also cannot match the velocity in the bulk. The R13

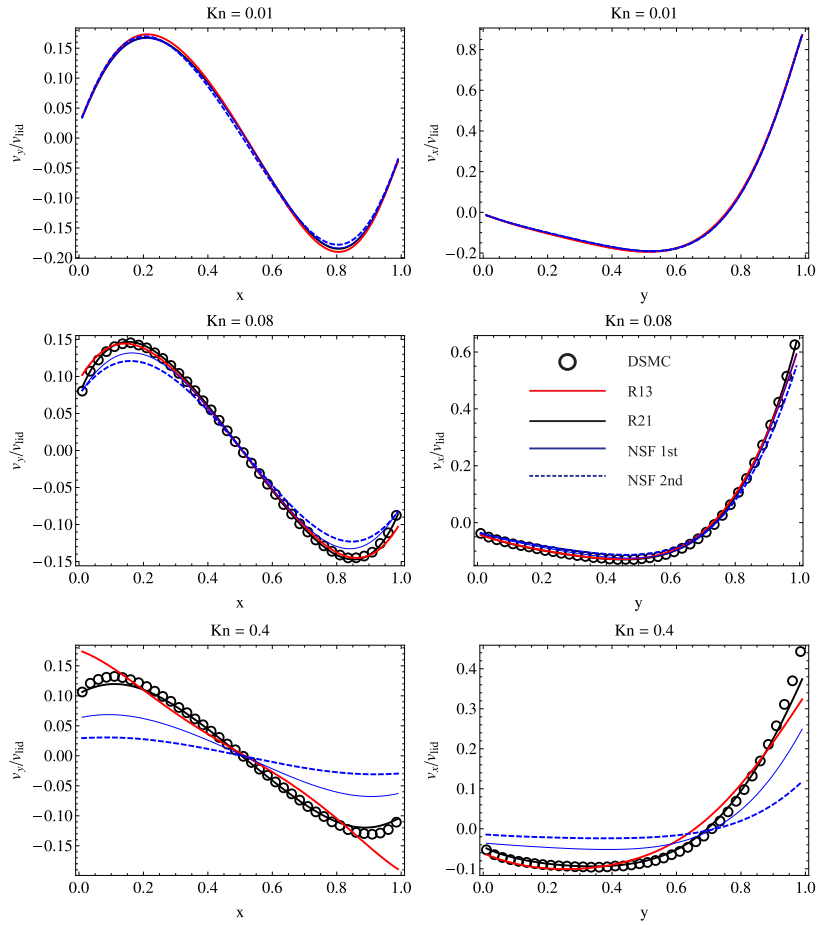

Figure 7.3: Isothermal lid driven cavity: (left) Profiles of the y-component of the velocity v_y/v_{lid}, on a horizontal plane crossing the center of the main vortex and (right) the profiles of the x-component of the velocity v_x/v_{lid}, on a vertical plane crossing the center of the cavity, for various values of Kn and for $v_{lid} = 50\ m/s$.

equations, on the other hand, reproduce the velocity profiles in the bulk with rather good accuracy. Near the wall, where Knudsen layers dominate the flow, we observe some discrepancy which is due to the R13 equations' insufficient resolution of the Knudsen layers [104].

In Fig. (7.4), we compare the temperature profile along a vertical plane crossing the center of the cavity, for Kn = 0.08 and 0.4. Due to the relatively low lid velocity frictional heating is rather weak so that the temperature deviates only slightly from the wall temperature of 273K. In this case the NSF equations with first order boundary conditions do well for the smaller Knudsen number, but for the larger value they underpredict the temperature near the moving wall. The NSF equations with

second order boundary conditions substantially overpredict the temperature in both the cases. The R13 equations, on the other hand, predict the thermal behavior of the flow with reasonable accuracy for both the Knudsen numbers.

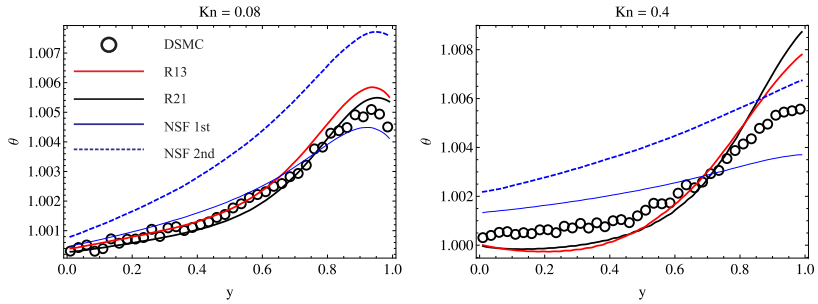

Figure 7.4: Isothermal lid driven cavity: comparison of the temperature profile along a vertical plane crossing the center of the cavity.

7.3.2 Knudsen Layers

Moment equations with few moments have only few layers for the superposition, and thus cannot match the details of the Knudsen layers. The results indicate that boundary jumps compensate for the lack of accuracy of the Knudsen layers such that the bulk flow is described well. This, indeed is what we observe in Fig. (7.3), where the R13 wall slip and Knudsen layer both differ from the exact solution, but the bulk result match closely.

As an indicator for this, we show our own calculations for the R21–moment equations into Fig. (7.3) and Fig. (7.4). We implemented the R21 equations as given in [67] with the proper boundary conditions into our numerical scheme; the R21 moment–equations can also be derived from R26–moment equations in [35]. As can be seen from Fig. (7.3) and Fig. (7.4), the addition of more moments leads to a better description of the velocity profile close to the wall—we attribute this to the additional Knudsen layer contribution in the sense of [99] that is present in the R21 equations. Detailed examinations of higher order moment equations is beyond the scope of this thesis.

Interestingly, for the two dimensional NSF case, when we use second order jump and slip conditions, the discrepancy to the exact solution is larger than that with first order boundary conditions. This stands in contrast to the simulation of Poiseuille flow where the second order velocity slip boundary conditions yield marked improvement

over the first order conditions, in particular, the prediction of the Knudsen minimum, and the overall flow rate [104]. This behavior of NSF equations with second order boundary conditions is consistent with the findings of [70], where it has been shown that these boundary conditions are not necessarily useful in more general situations.

7.3.3 Global Flow Properties

Most often, one will not be interested in the very details of a process, but in some meaningful *global* flow properties. For the driven cavity, these are the drag coefficient on the moving wall D and the dimensionless flow rate of the main vortex G defined as [121]

$$D = \int_0^1 \frac{\sigma_{ij}}{p_0}(x,1)dx, \text{ and } \quad G = \int_0^1 \frac{|v_x(1/2,y)|}{v_{lid}}dy \ . \tag{7.18}$$

Results of R13 and NSF models together with the IMM data of Sharipov et. al. [121] are presented in Tables 7.1 and 7.2 for D and G, respectively, with different values of the rarefaction parameter $\delta = \sqrt{\frac{1}{2}}\frac{1}{\mathrm{Kn}}$.

Kn	δ	D [121]	D (R13)	D (NSF1)	D (NSF2)
0.010	70.7	—	0.1585	0.1476	0.1416
0.071	10	$0.415 - 0.417$	0.4271	0.4967	0.4000
0.141	5	$0.502 - 0.507$	0.5084	0.6613	0.4474
0.354	2	$0.580 - 0.592$	0.5644	0.8554	0.3717
0.707	1	$0.620 - 0.631$	0.5722	0.9619	0.2533

Table 7.1: Isothermal lid driven cavity: dimensionless drag coefficient D on the moving wall vs Knudsen number for the R13 and NSF equations with first-order boundary conditions (NSF1) and second-order boundary conditions (NSF2).

We could not find DSMC and IMM results for Knudsen numbers below 0.07. For small Knudsen number $\mathrm{Kn} = 0.01$, R13 and NSF already show a relative difference of 7%. While lack of an exact solution does not permit us to judge whether R13 or NSF is more accurate at this small Knudsen number, the results for higher Knudsen numbers indicate the advantage of using R13: as the Knudsen number grows, NSF and R13 results differ more and more, where R13 agrees well with the exact solution (IMM) for Knudsen numbers up to 0.5, while NSF already has an error of more than 19% at $\mathrm{Kn} = 0.07$. This behavior is a reflection of the order of the respective equations. NSF with slip and jump boundary conditions is of first order in the Knudsen number, and

Kn	δ	G [121]	G (R13)	G (NSF1)	G (NSF2)
0.010	70.7	—	0.1893	0.1878	0.1878
0.071	10	$0.143 - 0.145$	0.1428	0.1389	0.1298
0.141	5	$0.127 - 0.128$	0.1216	0.1077	0.0860
0.354	2	$0.111 - 0.112$	0.1044	0.0653	0.0323
0.707	1	$0.104 - 0.106$	0.1003	0.0397	0.0113

Table 7.2: Isothermal lid driven cavity: gimensionless flow rate G vs Knudsen number for the R13 and NSF equations with first-order boundary conditions (NSF1) and second-order boundary conditions (NSF2).

cannot be expected to give reliable results above Kn = 0.05. R13, on the other hand, is of third order in Kn, and should give meaningful results up to Kn $\simeq \sqrt[3]{0.05} = 0.38$. For Kn = 0.707, R13 gives an error of less then 10%, while NSF with first and second order boundary conditions give an error of almost 50% and 60%, respectively. Clearly, both the theories are outside their range of validity, but R13 still gives a reasonable estimate that should have value as an engineering perspective.

7.3.4 Field Plots

Figures (7.5) and (7.6) show flow details for Kn = 0.08. Results computed with DSMC [45], R13, and NSF with first and second order boundary conditions are compared.

Figure (7.5) shows velocity streamlines superimposed on viscous shear stress contours. While the differences between the simulations are not marked, one can nevertheless see the differences in the details. DSMC (Fig. 7.5(a)) and R13 (Fig. 7.5(b)) show relatively similar stress contours, which differ from the NSF contours Fig. 7.5(c and d). In particular, DSMC and R13 show more uniform stress fields at the upper and lower walls whereas the NSF solutions show more variation along these walls.

7.3.5 Anti-Fourier Heat Flux

The most notable difference between DSMC (Fig. 7.6(a)) and NSF (Fig. 7.6(c and d)), is the reverse direction of the heat flux. In the NSF results, Fourier's law forces the heat flux to point from hot to cold, along the negative temperature gradient.

In the DSMC results, the direction is inverted, that is heat is transferred from cold to warm. In a DSMC solution, as in any numerical solution of the Boltzmann equation, this is an outcome of the simulation which cannot be further analyzed to

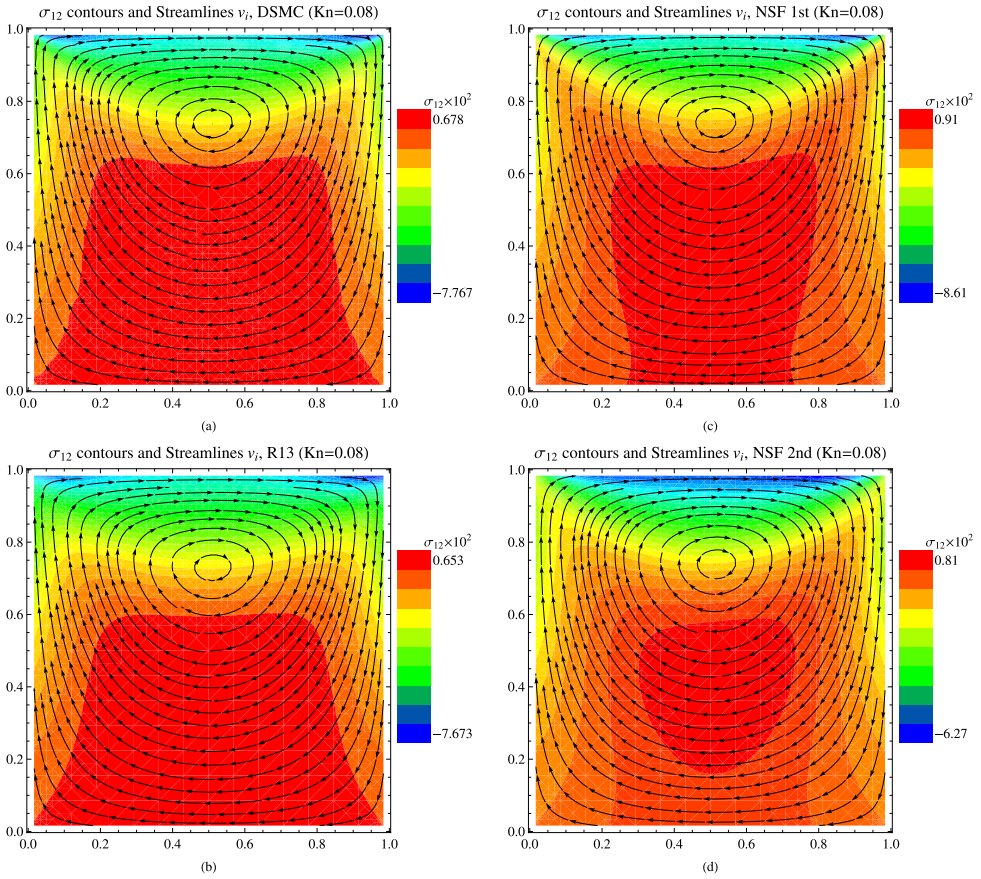

Figure 7.5: Isothermal lid driven cavity: streamlines superimposed on viscous shear stress σ_{xy} contours with Kn $= 0.08$, $v_{lid} = 50m/s$.

increase understanding of the interaction of flow properties. This is different for the R13 equations, which show the same behavior as the DSMC results, i.e., a heat flux vector pointing from cold to warm.

The heat flux is given by Eq. (3.27) and the question is which of the many terms lead to the inverted heat flow. We proceed with a discussion of the equation in terms of the process at hand, in order to isolate the most important terms. The first reduction comes from the observation that the driving force (the velocity of the lid) is relatively small, which implies that non-linear effects should only play a minor role, and linear terms dominate. That is, it suffices to look at the linearization of (3.27), which after use of (3.31) assumes the form

$$\theta\frac{\partial\sigma_{ik}}{\partial x_k}+\frac{5}{2}p\frac{\partial\theta}{\partial x_i}=-\frac{2}{3}\frac{p}{\mu}q_i+\frac{12}{5}\frac{\mu}{p}\theta\left[\frac{\partial^2 q_i}{\partial x_k\partial x_k}+\frac{\partial^2 q_k}{\partial x_i\partial x_k}\right]. \tag{7.19}$$

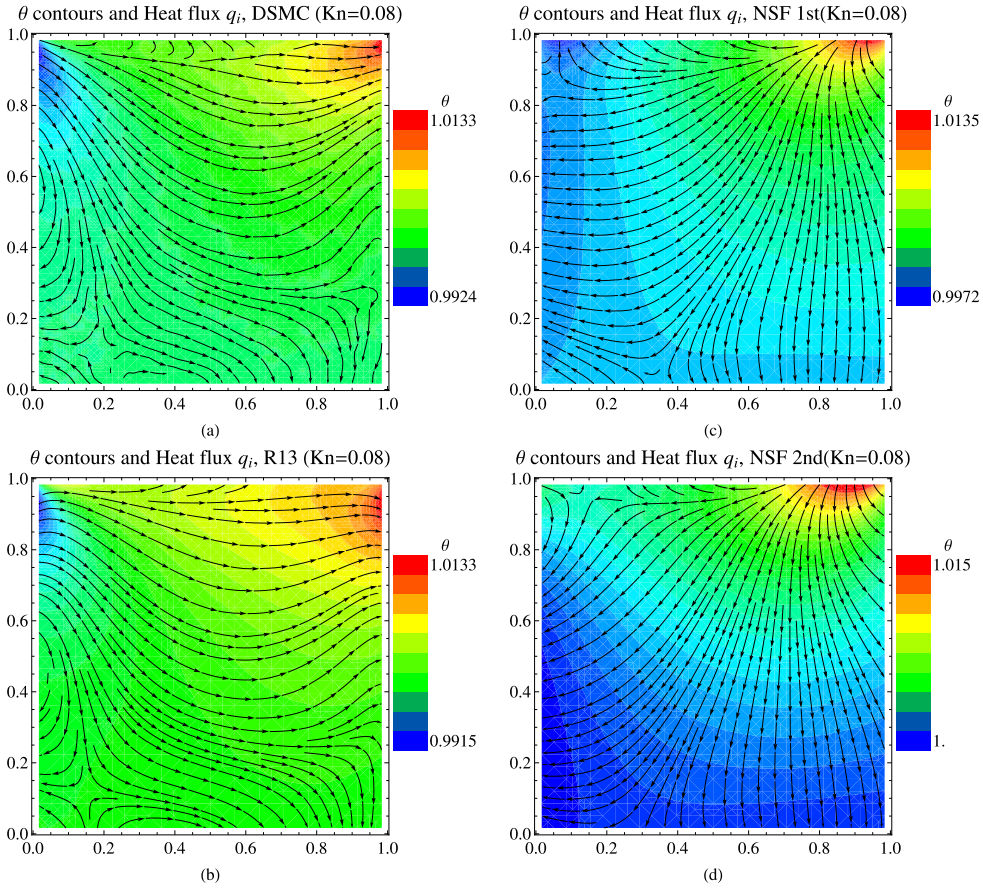

Figure 7.6: Isothermal lid driven cavity: heat flux superimposed on temperature θ contours with Kn $= 0.08$, $v_{lid} = 50m/s$.

As can be seen from the detailed discussion in, e.g., Refs. [104][118][97] and also from our discussion in Chapter 5, the derivative terms on the right hand side produce Knudsen layers. The results shown are for a relatively small Knudsen number Kn $=$ 0.08, where the Knudsen layers are restricted to the regions close to the walls. Hence, for the explanation of the inverted heat flux, these terms are not relevant, and the heat flux in the bulk can be written as

$$q_i = -\frac{15}{4}\mu\frac{\partial\theta}{\partial x_i} - \frac{3}{2}\frac{\mu}{p}\theta\frac{\partial\sigma_{ik}}{\partial x_k}. \tag{7.20}$$

Here, the first term is the well-known Fourier contribution to heat flux, which is of first order in the Knudsen number (first order in viscosity μ in dimensional form). The second term is a second order correction to the heat flux, which relates this to

the gradient in stress. When one replaces the stress by means of the Navier-Stokes law (3.19), one finds terms with the second derivative of velocity which are well-known from the Burnett equations [97]. Close to the lid, the heat flux is mainly in x-direction, therefore we can have a look at q_x, which can be further written as

$$q_x = -\frac{15}{4}\mu\frac{\partial\theta}{\partial x} - \frac{3}{2}\frac{\mu}{p}\theta\frac{\partial\sigma_{xx}}{\partial x} - \frac{3}{2}\frac{\mu}{p}\theta\frac{\partial\sigma_{xy}}{\partial y}. \tag{7.21}$$

In the dimensionless quantities plotted in Figs. (7.5) and (7.6), the above equation after linearization, reads

$$q_x = -\frac{15}{4}\mathrm{Kn}\left[\frac{\partial\theta}{\partial x} + \frac{2}{5}\frac{\partial\sigma_{xx}}{\partial x} + \frac{2}{5}\frac{\partial\sigma_{xy}}{\partial y}\right]. \tag{7.22}$$

Our results indicate that the term $\frac{\partial\sigma_{xx}}{\partial x}$ is significantly smaller than the other two terms. Thus, the sign of q_x depends on the relative size of $\frac{\partial\theta}{\partial x}$ and $\frac{2}{5}\frac{\partial\sigma_{xy}}{\partial y}$. Estimates for these gradients can be read directly from the figures: looking at the top row of Fig. 7.6(a), we estimate $\frac{\partial\theta}{\partial x} \simeq 0.021$, and looking at the centerline of Fig. 7.5(a), we estimate $\frac{\partial\sigma_{xy}}{\partial y} \simeq -0.084$ and hence $\frac{2}{5}\frac{\partial\sigma_{xy}}{\partial y} \simeq -0.034$. Thus, for these flow conditions, the stress gradient dominates and as a result the heat flux points from cold to warm.

7.4 Lid driven cavity with adiabatic walls

Similar to the case considered earlier, we consider a rarefied gas contained in a square square cavity where the upper boundary (lid) is in motion with a constant horizontal velocity v_{lid}, see Fig. (7.7). The lid of the cavity is considered to be an isothermal wall kept at a reference temperature θ_0. The Maxwell accommodation boundary conditions (Section 4.1), with complete accommodation ($\chi = 1$) are prescribed on the upper wall. The other three walls are assumed to be adiabatic walls, and the process on these walls is described by the isotropic scattering model (Section 4.2).

To obtain the DSMC solution for this problem, an existing DSMC scheme of Roohi and co-workers [82, 69, 68, 70] was modified, which allows us to model a gas of Maxwell molecules as well as for the isotropic scattering at the wall. The details of implementation of DSMC is beyond the scope of this dissertation, we shall only show the results obtained. These results will serve us for comparison.

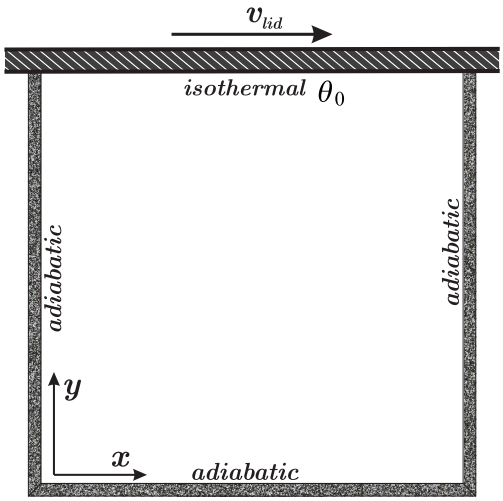

Figure 7.7: Schematic of the lid driven cavity with the imposed boundary conditions.

7.5 Results and discussions

In Fig. 7.8, we show the velocity streamlines superimposed on the viscous shear stress contours, resulting from (a) the R13–moment equations, (b) DSMC method, and (c) the Navier-Stokes-Fourier equations with first order boundary conditions, respectively, when Kn = 0.05 and $v_{lid} = 100m/s$. Similar to the isothermal wall cavity case, the differences between the simulations are not marked. DSMC Fig. 7.8(b) and R13 Fig. 7.8(a) show relatively similar stress contours, which differ from the NSF contours (Fig. 7.8(c)). The DSMC and R13 show more uniform stress fields at the upper and lower walls, whereas the NSF solutions show more variation along these walls.

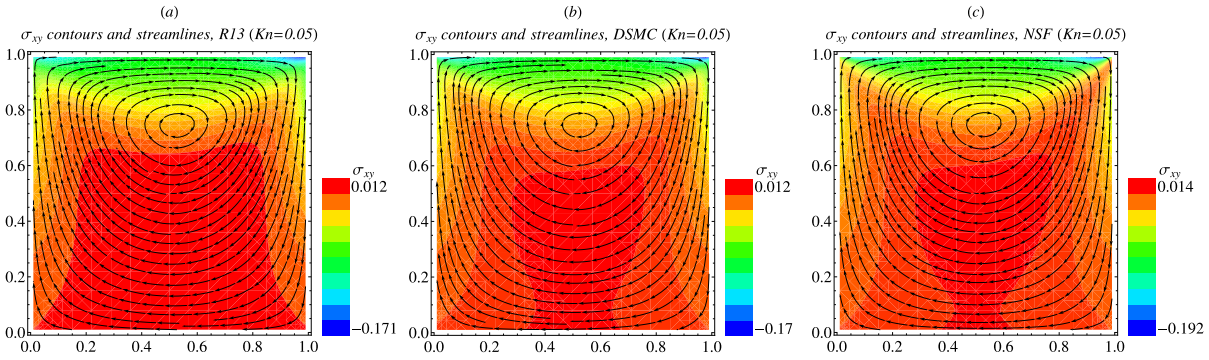

Figure 7.8: Adiabatic lid driven cavity: streamlines superimposed on viscous shear stress σ_{xy} contours with Kn = 0.05, $v_{lid} = 100m/s$.

In Fig. 7.9, we show the profiles of the dimensionless vertical component of the velocity, v_y/v_{lid}, along the vertical centerline of the cavity, and the dimensionless horizontal component of the velocity, v_x/v_{lid}, along the horizontal line crossing the centre of the vortex, respectively. For the given value of the Knudsen number all models exhibit a good agreement with DSMC.

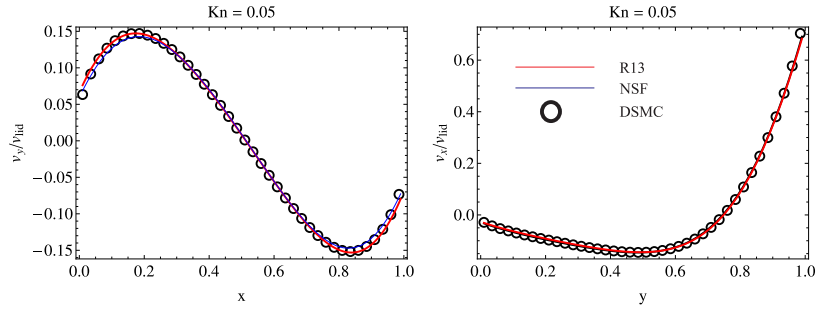

Figure 7.9: Adiabatic lid driven cavity: (left) profiles of the y-component of the velocity v_y/v_{lid}, on a horizontal plane crossing the center of the main vortex and (right) the profiles of the x-component of the velocity v_x/v_{lid}, on a vertical plane crossing the center of the adiabatic cavity.

Figure 7.10 illustrates the heat flux lines inside the cavity for (a) the R13 equations, (b) DSMC method and (c) NSF equations (c), when Kn = 0.05 and $v_{lid} = 100m/s$. Similar to the isothermal wall cavity, the "cold-to-warm" heat transfer is observed in the flow-field which is accurately captured by the R13–moment equations. A closer look into the DSMC and R13 results in the right hand side of the flow-field reveals that the associated curvature in the heat lines are properly captured by the continuum method. However, the curvature of the heat lines predicted by the R13–moment equations is slightly different in the left hand side of the domain.

Interestingly, in the DSMC results, the heat lines close to the side walls are not parallel to the walls. In the DSMC results, as we can see from Fig. 7.10(b), the heat lines have a perpendicular component to the side walls.

The friction between the gas and the boundary generates heat flux, which cannot escape from an adiabatic wall, and consequently, is directed toward the middle of the cavity. However, the R13 and NSF results, in Fig. 7.10(a and c), show that the heat lines close to the adiabatic boundaries are parallel to the walls. We attribute this difference to the linearity in the boundary conditions for the adiabatic wall, given by Eqs. (4.23).

Let us recall from Section 4.2 that—while obtaining boundary conditions for an

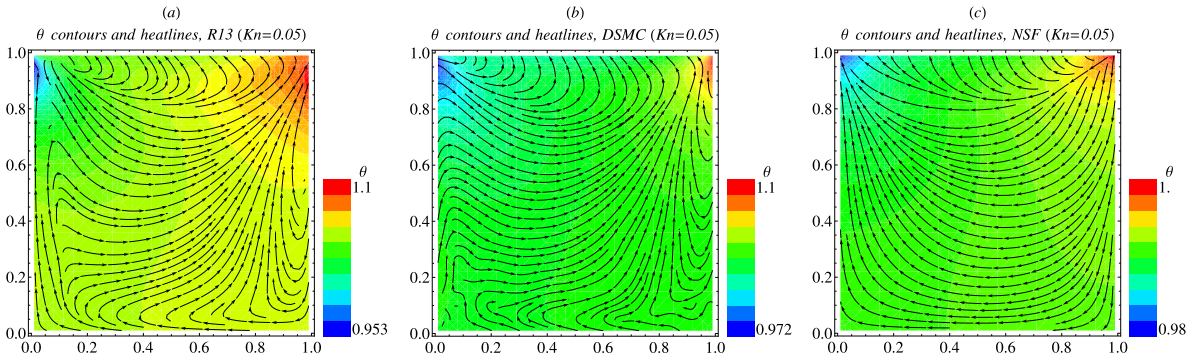

Figure 7.10: Adiabatic lid driven cavity: heat flux superimposed on temperature θ contours with Kn $= 0.05$, $v_{lid} = 100m/s$.

adiabatic wall—we assumed linearity of the process. Linear boundary conditions can not describe the non-linear viscous heating on the boundary, and one must consider a non-linear adiabatic wall model to capture this phenomenon.

To further investigate the accuracy of the employed methods, in Fig. 7.11, we illustrate the shear stress σ_{xy} (left) along the driven lid of cavity and the horizontal component of the heat flux q_x (right) along the vertical centerline of the cavity, for Kn $= 0.05$.

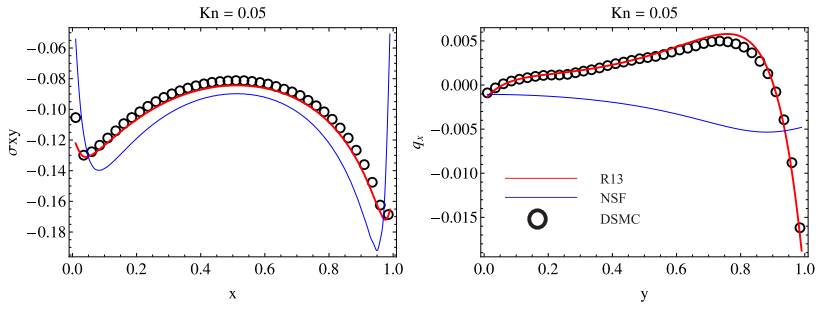

Figure 7.11: Adiabatic lid driven cavity: shear stress σ_{xy} (left) along the driven lid of cavity and the horizontal component of the heat flux q_x (right) along the vertical centerline of the cavity, for Kn $= 0.05$ and $v_{lid} = 100m/s$.

It can be observed from Fig. 7.11, that the R13 equations provide very accurate results for the magnitude of the shear stress in the vicinity of the driven lid. Also for the given value of Knudsen number, the heat flux along the vertical centerline the R13 theory gives very good agreement with DSMC, whereas the NSF theory fails already.

7.5.1 Drag coefficient

Finally, we compare the average drag coefficient on the driven lid of the cavity obtained from the three approaches, for three different values of the Knudsen number and for $v_{lid} = 100m/s$. The drag coefficient on the driven lid is obtained by:

$$D = \int_0^1 \frac{\sigma_{ij}}{p_0}(x, 1)dx$$

Table (7.3) shows the the drag coefficient for $v_{lid} = 50m/s$, and Table (7.4) shows the variation of the drag coefficient with for $v_{lid} = 100m/s$.

Kn	D (DSMC)	D (R13)	D (NSF)
0.05	0.04575	0.04674	0.04870
0.1	0.06088	0.06209	0.06889
0.3	0.08003	0.07756	0.09892

Table 7.3: Adiabatic lid driven cavity: dimensionless drag coefficient, D on the moving wall vs Knudsen number obtained from the DSMC method, R13 equations and the NSF equations with first order boundary conditions, for $v_{lid} = 50m/s$.

Kn	D (DSMC)	D (R13)	D (NSF)
0.05	0.09303	0.09568	0.09875
0.1	0.12424	0.12575	0.13877

Table 7.4: Adiabatic lid driven cavity: dimensionless drag coefficient, D on the moving wall vs Knudsen number obtained from the DSMC method, R13 equations and the NSF equations with first order boundary conditions, for $v_{lid} = 100m/s$.

Comparison of the R13 results with the DSMC data demonstrates that the R13 equations can accurately predict the drag coefficient up to Kn = 0.3.

Chapter 8

Heat transfer in a micro cavity

In the present chapter, the flow behavior and heat transfer characteristics of a rarefied gas confined in a bottom heated square cavity [15, 90]. The simulations are performed using the R13 equations and NSF equations with first order slip and jump boundary conditions (see Section 4.1.3) and the results are compared to DSMC solutions.

The R13 theory gives satisfying results—including flow patterns in fair agreement with DSMC—in the transition regime, which the NSF equations are not able to capture. We perform an analysis of the heat flux and the shear stress distribution and show that the classical hydrodynamic does not take into account the non-equilibrium shear stress caused by the heat flux gradients. Preliminary results for this problem were published in [119].

8.1 Problem Formulation

We consider the steady heat transfer through argon gas in a two-dimensional square cavity of side length L. The bottom surface of the cavity is kept at temperature T_H, and the other sides are maintained at temperature T_C, as shown in Fig. (8.1). The walls of the cavity are assumed to be fully diffusive, i.e., $\chi = 1$. The third dimension of the cavity is assumed to be large enough so that the fluid flow can be considered as two-dimensional. Moreover, the effects of radiation and gravity are assumed to be negligible.

In the present study, the distance L between the plates is taken to be 1 μm and the average density, ρ_0, is varied to change the Knudsen number. The wall temperatures are fixed at $T_C = 300$K and $T_H = 600$K. This large temperature difference is

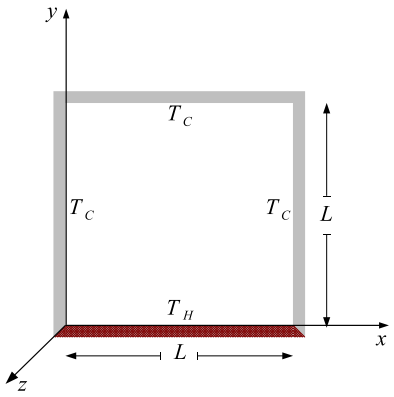

Figure 8.1: Schematic of the problem with the imposed thermal conditions.

used since for smaller temperature differences, the DSMC method converges—in the Knudsen number range considered—very slowly. The reference viscosity of the Argon gas at reference temperature $T_0 = 273$K, according to [7], is $\mu_0 = 1.9552 \times 10^{-5}$ Ns/m^2. Temperature dependence of the viscosity $\hat{\mu}$ is given from equation (2.19), with the temperature exponent $\omega = 1$, for Maxwell molecules.

The simulations were conducted using a two-dimensional grid with 120×120 uniformly spaced grid points. A grid independence test was conducted with different meshes of size $N = 17$, 35, 70, 140, 280. For various mesh sizes, Fig. 8.2(a) shows the relative change in the net dimensionless heat transfer from the bottom surface

$$Q_y = \frac{1}{N} \sum_{i=1}^{N} (q_y)_{i,1}$$

and the average temperature along the heated surface

$$\bar{\theta} = \frac{1}{N} \sum_{i=1}^{N} \theta_{i,1}.$$

The maximum deviations observed in terms of Q_y and $\bar{\theta}$ remain within 0.61% and 0.41%, respectively, when the grid of 120×120 is considered. This justifies the selected grid size 120×120 as a reasonable compromise between computational effort and desired accuracy. A typical simulation with the R13 equations (as well as NSF), when a grid of size 120×120 are considered, takes about 20 min on a single quad core desktop PC. Whereas, depending on the flow parameters and the value of the Knudsen number, DSMC simulation takes up to 70 hours of the computational time.

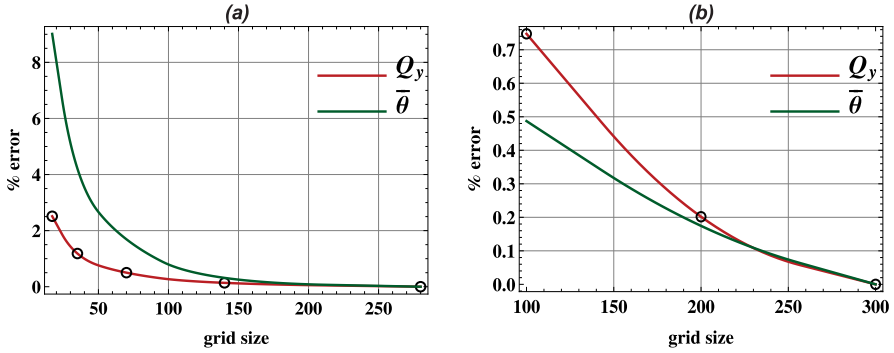

Figure 8.2: Grid independence test of the numerical solution in terms of Q_y and $\bar{\theta}$ for Kn = 0.13. (a) R13 solution and (b) DSMC method.

The DSMC method used in this chapter follows the scheme given in [82, 69, 68, 70]. In the current study Maxwell argon particles with $m = 6.63 \times 10^{-26}$kg and reference viscosity of $\mu_0 = 1.9549 \times 10^{-5}$Pa.s are considered. The particle diameter, d, is related to the reference viscosity by the relation [7]

$$d^2 = \frac{5\,(\alpha+1)\,(\alpha+2)\,\sqrt{mkT_0/\pi}}{4\alpha\,(5-2\omega)\,(7-2\omega)\,\mu_0},$$

with $\alpha = 2.13986$ and $\omega = 1$ for Maxwell molecules [7] and k is the Boltzmann constant. The Knudsen number according to [7] then reads,

$$Kn_b = \frac{1}{L}\frac{1}{\sqrt{2}\pi d^2 n_0}.$$

This definition of the Knudsen number is related to the one used in the preceding chapters by the relation Kn $\cong 1.27\, Kn_b$. To avoid any confusion, all results presented in this chapter are given in terms of the Knudsen number Kn defined in Chapter 5.

For gas solid interaction Maxwell's accommodation model is employed. The accommodation coefficient χ is assigned the value of unity; i.e. fully diffusive reflection has been assumed for all computations. In order to perform the grid independency test for DSMC, we considered four grids composed of 50×50, 100×100, 200×200, and 300×300 cells. Relative percentage changes in the net dimensionless heat transfer and the average temperature along the heated surface are plotted in Fig. 8.2(b). It is seen that the results are numerically equivalent for 200×200 and 300×300 grids, with the relative errors less than 0.2% for both Q_y as well as $\bar{\theta}$. Therefore, the grid

containing 200×200 cells is selected for the reported results of the DSMC method in this study.

8.2 Results and discussion

8.2.1 Analysis of Streamlines and Isotherms

Figure 8.3 shows the velocity streamlines superimposed on the temperature contours resulting from the Navier-Stokes-Fourier, DSMC, and the R13 theory, respectively, at Kn = 0.05. The NSF results show two counter circulating primary vortices, symmetrical with respect to the center of the cavity. The flow velocity is relatively small indicating a rather slow convective motion ($v \approx 0.1m/s$). The formation of the pri-

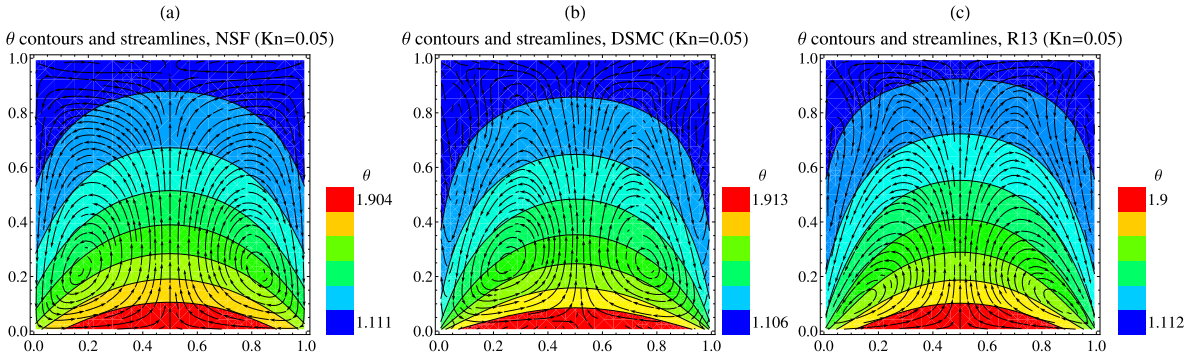

Figure 8.3: Streamlines and temperature contours for Kn = 0.05. (a) NSF solutions, (b) DSMC solutions, and (c) R13 solutions.

mary vortices is due to the sharp temperature gradients in the corners between the heated and cooled walls, which induce thermal transpiration. As can be seen from the figures, the isotherms near the corners are visibly denser, which indicates higher temperature gradients in this region.

Interestingly, in addition to the primary vortices, the R13 equations and DSMC both predict two secondary counter-circulating vortices located along the vertical cold surfaces. The formation of the secondary vortices can be explained by the different terms in the slip boundary condition (4.13b), which reads

$$-v_y \approx \frac{1}{\mathcal{P}}\left(\sqrt{\frac{\pi\theta}{2}}\sigma_{xy} + \frac{1}{5}q_y\right) = v_y^{vis} + v_y^{tra}. \tag{8.1}$$

Variations of the viscous velocity, $v_y^{vis} = \frac{1}{\mathcal{P}}\sqrt{\frac{\pi\theta}{2}}\sigma_{xy}$, and the transpirational velocity, $v_y^{tra} = \frac{1}{\mathcal{P}}\frac{1}{5}q_y$, evaluated along $x = 0$, are presented in Fig. 8.4, for NSF, DSMC, and R13 solutions.

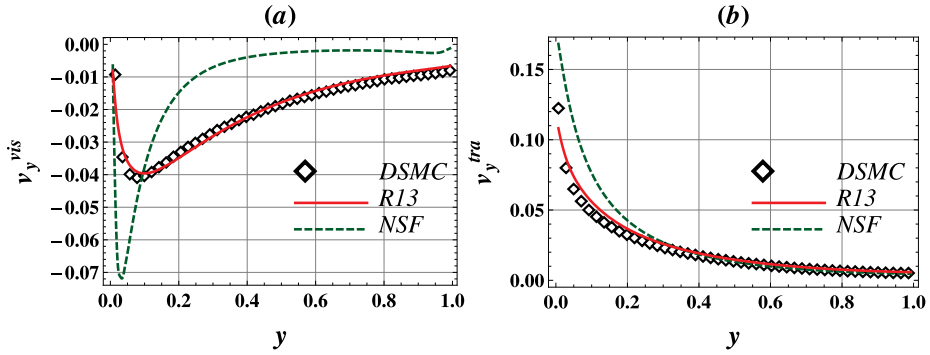

Figure 8.4: Variations of the viscous velocity and the transpirational velocity for Kn = 0.05. (a) viscous and (b) transpirational contribution to the slip velocity.

Along the vertical surface, $x = 0$, the viscous velocity is negative, thus inducing a flow in the upward direction.

On the other hand, the transpirational velocity is positive (heat flows upwards, from hot to cold), inducing consequently a flow in downward direction, from the colder to hotter region. Hence, both terms induce flows in opposite direction. The respective magnitudes of these terms determine the actual local direction of the flow along $x = 0$.

For DSMC, the viscous contribution is larger than the transpiration term, hence the secondary vortices appear. The NSF equations are unable to produce the secondary vortices since for them the transpirational velocity along the vertical wall dominates the viscous velocity. The R13 equations, however, give a better description of stress and heat flux and capture the formation of secondary whirls.

By increasing the Knudsen number to 0.13 (Fig. 8.5), the fluid circulation becomes more intense. The flow structure for NSF remains bicellular, whereas R13 as well as DSMC predict the appearance of two additional small vortices located near the upper surface of the cavity. For the NSF equations, the isotherms exhibit smaller curvature near the vertical sidewalls. A further increase in Knudsen number to Kn = 0.3 leads to significant changes in the flow fields, as can be observed in Fig. 8.6. For the DSMC simulation, the secondary vortices span most of the cavity area, whereas for R13 the secondary eddies extend only about the upper half of the domain.

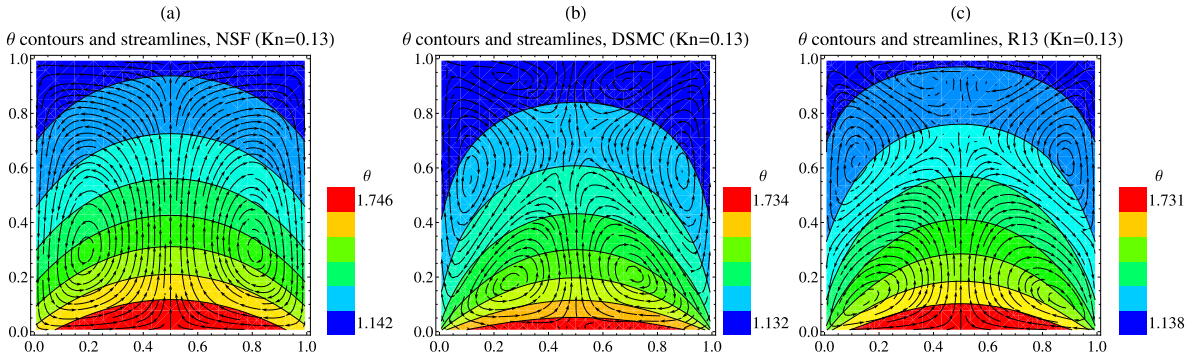

Figure 8.5: Streamlines and temperature contours for Kn = 0.13. (a) NSF solutions, (b) DSMC solutions, and (c) R13 solutions.

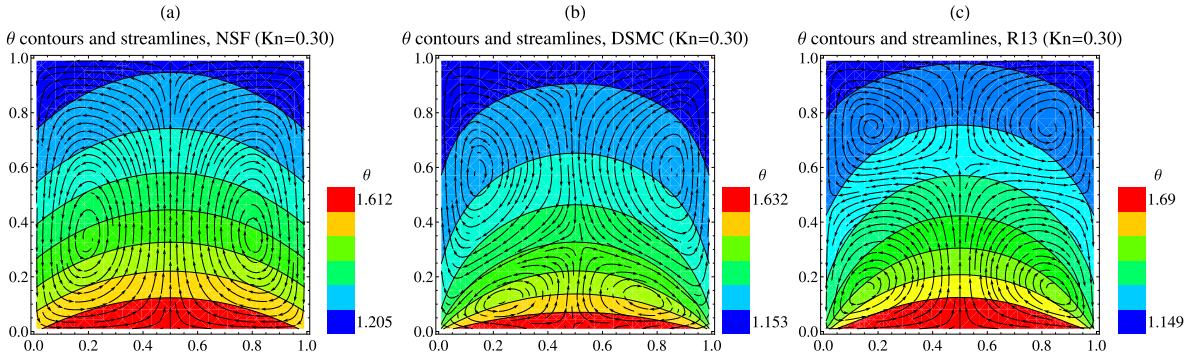

Figure 8.6: Streamlines and temperature contours for Kn = 0.30. (a) NSF solutions, (b) DSMC solutions, and (c) R13 solutions.

From the differences to the DSMC results, it becomes obvious that this Knudsen number is outside of the range of applicability of both the R13 and NSF theories. However, the qualitative description given by the R13 equations is comparable with DSMC, while the NSF equations cannot describe the flow features.

8.2.2 Analysis of heat flux lines and shear stress distribution

Figure 8.7 shows heat flux lines superimposed on viscous shear stress contours (σ_{xy}) for Kn = 0.05, computed with NSF, DSMC, and R13, respectively. The distribution of heat flux lines is similar for the NSF, R13 and the DSMC solutions indicating a dominating Fourier heat transfer contribution, but, as will be seen in the next section, the actual values for heat transfer differ markedly.

As far as the shear stresses are concerned, DSMC (Fig. 8.7(b)) and R13 (Fig. 8.7(c))

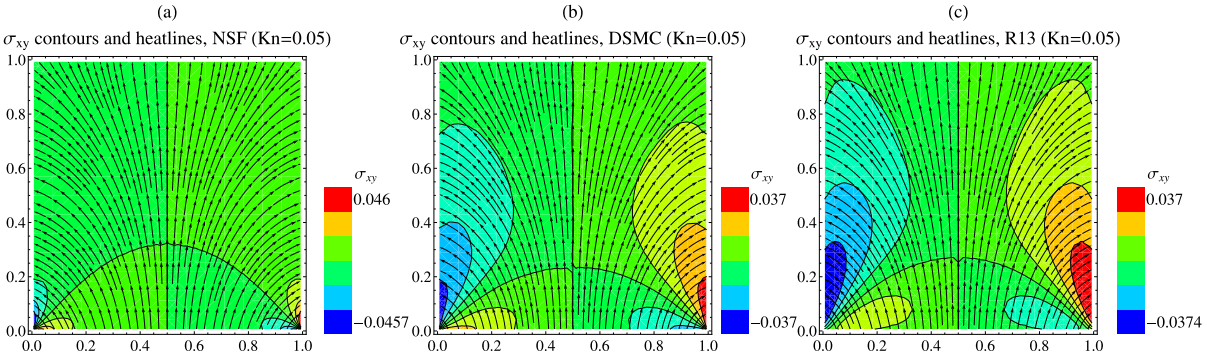

Figure 8.7: Heat flux lines and shear stress contours for Kn = 0.05. (a) NSF solutions, (b) DSMC solutions, and (c) R13 solutions.

show relatively similar shear stress contours, which differ from the NSF contours (Fig. 8.7(a)) already at Kn = 0.05. The DSMC and R13 solutions show more uniform stress fields in the vicinity of the corners between the heated and cooled walls, whereas the NSF solutions show the stress localized to the lower corners.

With increase to Kn = 0.13, shown in Fig. 8.8, the corresponding heat flux lines exhibit relatively small divergence toward the vertical sidewalls indicating a weaker heat exchange between the bottom surface and the vertical surfaces.

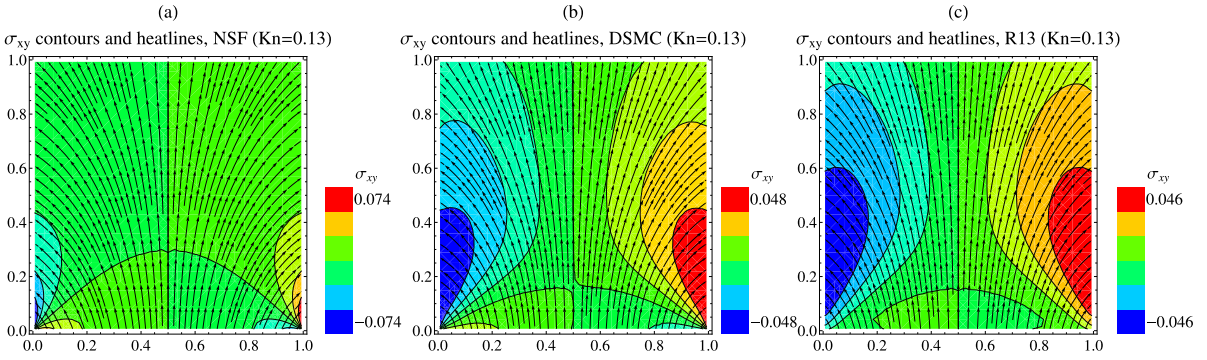

Figure 8.8: Heat flux lines and shear stress contours for Kn = 0.13. (a) NSF solutions, (b) DSMC solutions, and (c) R13 solutions.

8.2.3 Effect of Knudsen number on heat flux

Figure 8.9 illustrates the variation of the normal heat flux, q_y, along the bottom plate, obtained by solving R13 (solid curve), NSF (dashed curves) and DSMC (sym-

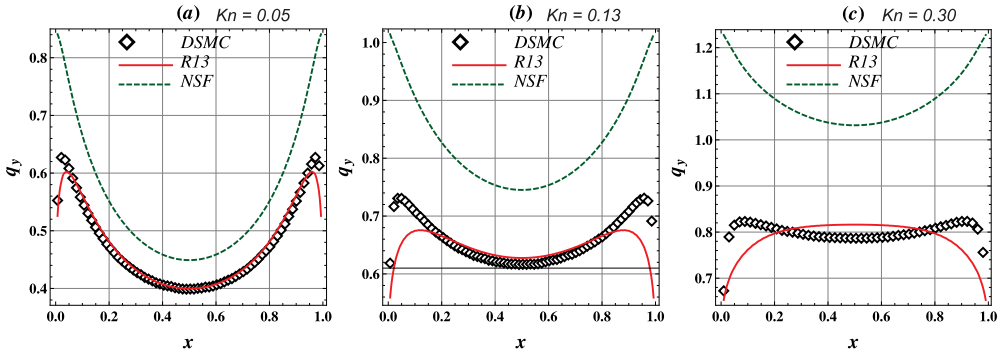

Figure 8.9: Normal heat flux, q_y, along the bottom plate, obtained by solving R13 (solid curve), NSF (dashed curves) and DSMC (symbols). (a) Kn = 0.05, (b) Kn = 0.13 and (c) Kn = 0.3.

bols). The results show that the normal heat flux calculated by the R13 equations agrees with the DSMC solution at smaller Knudsen numbers (Figs. 8.9 (a,b)). At larger Knudsen number, Kn = 0.3 in Fig. 8.9(c), the R13 equations underpredict the normal heat flux by 5%. The Navier-Stokes-Fourier's equations, however, predict approximately 15% higher normal heat flux than DSMC, already at small Knudsen number of 0.05. By increasing the Knudsen number value to 0.13 and 0.3, the NSF equations overpredict the normal heat flux by as much as 25% and 35%, respectively.

Higher Knudsen numbers show stronger non-equilibrium as indicated by larger magnitudes of q_y. Interestingly, the normal heat flux along the bottom plate, predicted by DSMC shows a bimodal behavior. This can also be observed in the results of the R13-system in Fig. 8.9, while the NSF system fails to capture this.

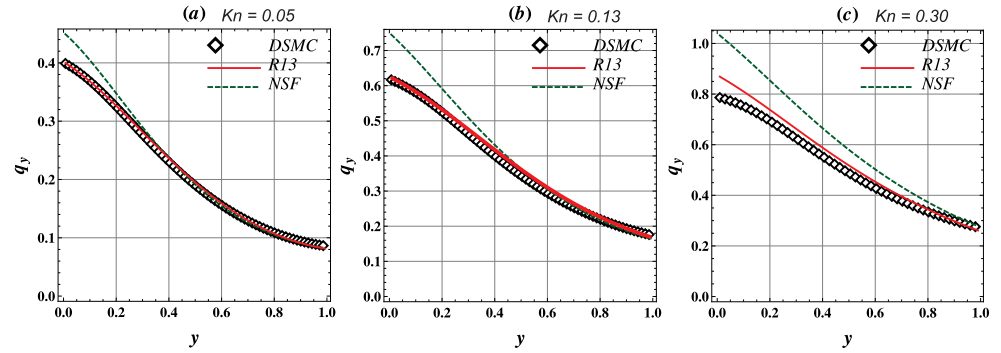

Figure 8.10: Normal heat flux, q_y, along the centerline of the cavity, obtained by solving R13 (solid curve), NSF (dashed green curves) and DSMC (symbols). (a) Kn = 0.05, (b) Kn = 0.13 and (c) Kn = 0.3.

The simulation results for the normal heat flux along the centerline of the cavity at Kn $= 0.05, 0.13, 0.3$ are shown in Fig. 8.10. As before, the simulation results of DSMC are compared with the NSF and R13 predictions. The R13 theory follows the DSMC result fairly accurate as long as Kn $\lesssim 0.3$.

The average dimensionless heat transfer along the heated element, defined as

$$Q_y = \int_0^1 q_y\,(x, 0)\,dx, \tag{8.2}$$

is shown in Fig. 8.11 for Knudsen numbers below 0.4.

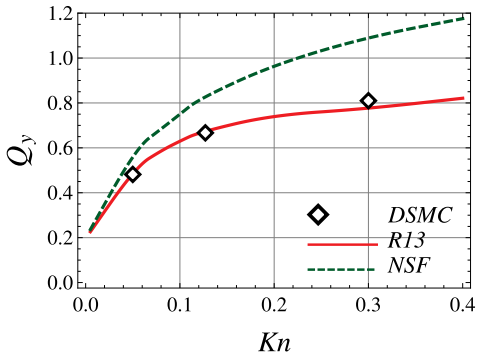

Figure 8.11: The average dimensionless heat transfer along the heated element, Q_y, for various Kn.

The figure shows a monotonous increase in Q_y with Kn for all three theories. It can be seen that the rate of increase in heat transfer is larger for the NSF model than that corresponding to DSMC and R13.

8.2.4 Influence of temperature ratio

In Fig. 8.12, numerical results for the dimensionless effective heat conductivity, defined as

$$\kappa = \frac{Q_y}{\frac{15}{4}\mathrm{Kn}\,(\theta_H - \theta_C)}, \tag{8.3}$$

are shown for temperature ratios $1.1 \leq T_H/T_C \leq 2$, for various values of the Knudsen number. Results on the dimensionless effective heat conductivity, based on the R13 and NSF theories, are presented in Fig. 8.12(a) and Fig. 8.12(b), respectively, for $T_C = T_0 = 273$ K. It is seen from Fig. 8.12 that the conductivity is decreased as Kn is increased. This behavior is expected since increasing the Knudsen number

diminishes the intermolecular collisions in the gas, and consequently the effective heat conductivity is decreased. Furthermore, as the temperature ratio, T_H/T_C, is increased, the effective heat conductivity is also increased. For all cases, NSF predicts a larger effective heat conductivity than R13. This matches our earlier observation that NSF drastically overpredicts the heat transfer (see Fig. 8.9).

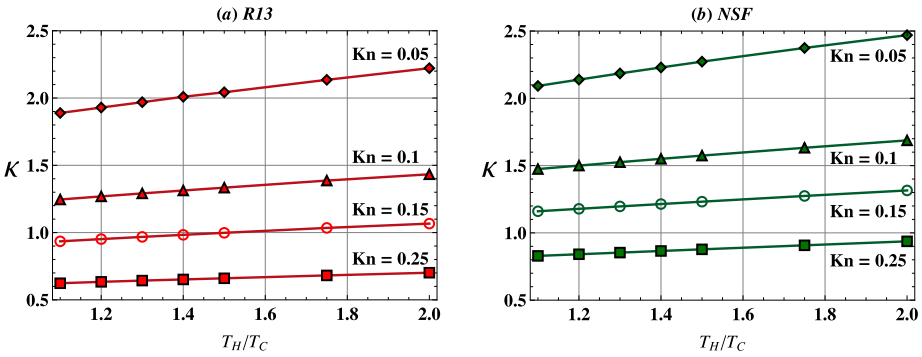

Figure 8.12: The dimensionless effective heat conductivity, κ, in terms of T_H/T_C for various values of Kn. (a) R13, (b) NSF.

The combined effects of the temperature ratio, T_H/T_C, and the Knudsen number, Kn, on the flow structure will be examined next. Results are reported in terms of isotherms and streamlines. These observations are shown by the plots in Fig. 8.13 (Kn = 0.05) and Fig. 8.14 (Kn = 0.1).

Figures 8.13 (a), (b), and (c) illustrate the results obtained from the R13 equations for the temperature ratio T_H/T_C = 1.1, 1.5, and 2, respectively, for the Knudsen number 0.05. The streamlines indicate that the secondary vortices grow along the vertical cold surfaces as the temperature ratio is increased.

The flow field for Kn = 0.1, shown in Figs. 8.14, show hardly visible secondary cells at low temperature ratio. These grow as the temperature ratio is increased, and an additional-cell flow pattern develops as T_H/T_C reaches 2.

8.2.5 Effects of convection on effective heat conductivity

In order to evaluate the influence of convection upon the effective heat conductivity, defined in eq. (8.3), we compare results for the R13 equations in the moving gas with those for a gas at rest. For this, we solve the R13 equations with zero velocity throughout, $v_i = 0$. The results are shown in Fig. 8.15(a), where the dashed curves are for the gas at rest, and the continuous curves are for the moving gas. The corresponding

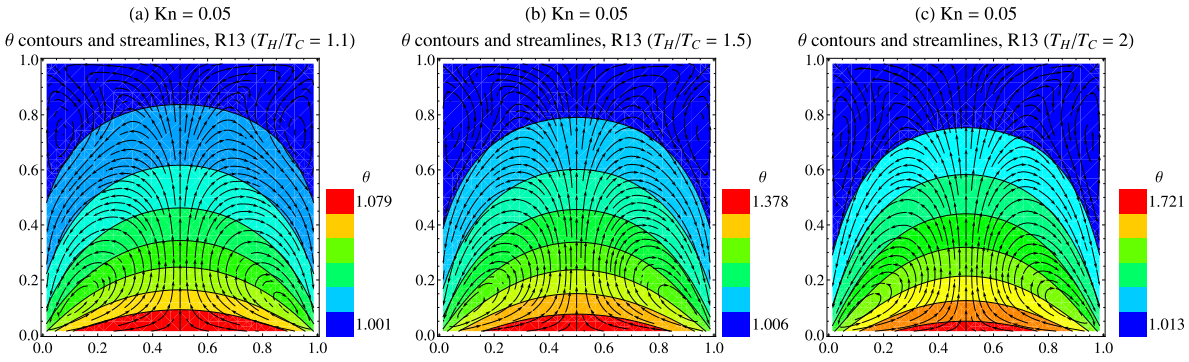

Figure 8.13: Streamlines and temperature contours for Kn = 0.05 for the R13 equations at various values of the temperature ratio, T_H/T_C. (a) $T_H/T_C = 1.1$, (b) $T_H/T_C = 1.5$, and (c) $T_H/T_C = 2$.

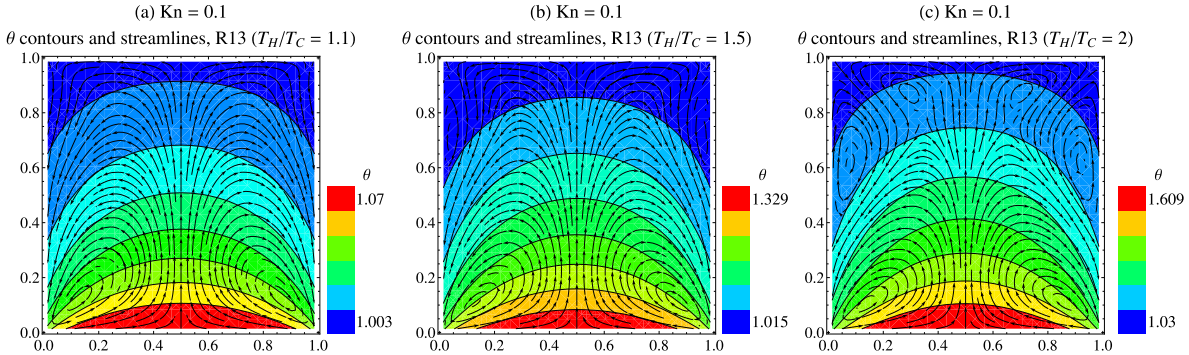

Figure 8.14: Streamlines and temperature contours for Kn = 0.1 for R13 equations at various values of the temperature ratio, T_H/T_C. (a) $T_H/T_C = 1.1$, (b) $T_H/T_C = 1.5$, and (c) $T_H/T_C = 2$.

results computed with the NSF equations are presented in Fig. 8.15(b). As we see from Fig. 8.15, for both continuum models the effective heat conductivity in the pure heat conduction case ($v_i = 0$) is slightly higher than the effective heat conductivity in the moving gas; hence the heat transfer is slightly weakened by convection. At small temperature ratios, NSF and R13 both show a very small difference (less then 2%) between the heat conductivity in a moving gas and in stationary gas. At temperature ratio 2 this difference increases slightly up to 3-4%. We note that a comparable test is not possible in the classical DSMC method, since there the macroscopic gas velocity v_i cannot be controlled.

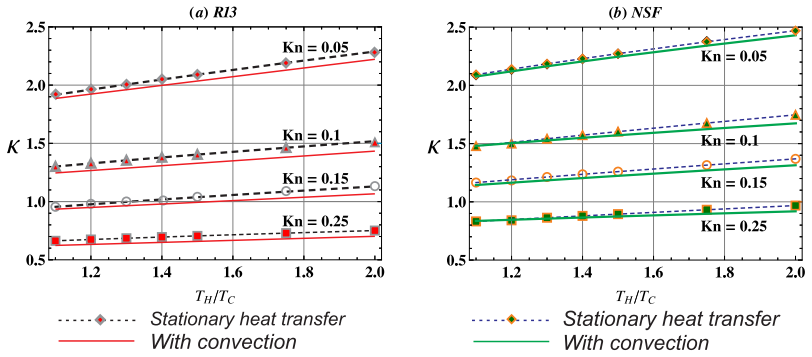

Figure 8.15: The effective heat conductivity is compared between a stationary gas (dashed curves) against the effective heat conductivity (continuous curves) in a moving gas, in terms of T_H/T_C for various values of Kn. (a) R13, (b) NSF.

Chapter 9

Initial boundary value problems in 1D

The focus of this chapter is on unsteady solutions of 1D problems; the extension to 2D can be achieved with some minor adjustments to the proposed numerical method. The finite volume based numerical scheme is derived for the R13, R10 and NSF equations. Particular attention has been paid regarding the implementation of the boundary conditions. Shock-tube verification test cases are given to check the good behavior of the numerical scheme and validation cases in planar and oscillatory Couette flows are presented to illustrate the accuracy of the numerical scheme.

9.1 Finite volume method

The finite volume method (FVM) is an increasingly popular method for the numerical solution of partial differential equations. In comparison to the finite difference method, FVM may be used on arbitrary geometries, using structured or unstructured meshes [54][110][20]. Additionally, the solution of a set of partial differential equations may lose regularity and the gradients may blow up in finite time. Consequently, the finite difference method may be expected to break down near discontinuities in the solution where the differential equations do not hold. In the FVM formulation, on the other hand, equations are used in integral form. This makes the FVM quite attractive when modelling problems for which dependent variables are not differentiable.

We are interested in the numerical solution for a system of partial differential

equations in the form

$$\frac{\partial U}{\partial t} + \frac{\partial F}{\partial y} + \frac{\partial F^{\nu}}{\partial y} = \frac{1}{\mathrm{Kn}} \mathcal{S}\left(U\right), \tag{9.1}$$

where $U\left(y,t\right)$ is the vector of conservative variables, $F(U)$, $F^{\nu}(U, \partial_y U)$ denote the convective and viscous fluxes, respectively, in the y-direction, and $\mathcal{S}\left(U\right)$ is the relaxational source term. The system is quasi-linear hyperbolic-parabolic with relaxation. The R13, NSF and R10 equations can be written in the conservative form (9.1) [13, 65, 111]. The R13 equations in the form of (9.1) are presented in [111], and also shown in Appendix B.

9.1.1 Spatial discretization

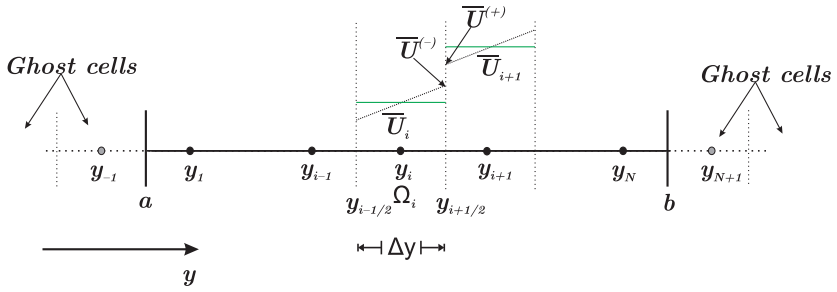

Figure 9.1: 1D finite volume mesh.

In order to perform a space finite volume discretization of (9.1), we divide the computational domain $\Omega = \left[y_{1/2}, y_{N+1/2}\right]$ into uniform cells of constant size $\Delta y = y_{i+1/2} - y_{i-1/2}$, $i \in \mathbb{Z}$, see Fig. (9.1).

The cell-centered finite volume method is derived, as usual, by integrating (9.1) on each cell $\Omega_i \in \left[y_{i-1/2},\ y_{i+1/2}\right]$, and then using the Gauss-Green divergence theorem. This yields a set of semi-discrete ordinary differential equations,

$$\frac{d\overline{U}_i}{dt} + \frac{1}{\Delta y}\left(F_{i+1/2} - F_{i-1/2}\right) + \frac{1}{\Delta y}\left(F^{\nu}_{i+1/2} - F^{\nu}_{i-1/2}\right) = \frac{1}{\mathrm{Kn}}\overline{\mathcal{S}}_i. \tag{9.2}$$

Here, $\overline{U}_i = \int_{\Omega_i} U dy$ is the cell average value of U on Ω_i, and

$$\overline{\mathcal{S}}_i = \int_{\Omega_i} \mathcal{S}\left(U\right) dy = \mathcal{S}\left(\overline{U}_i\right) + \mathcal{O}\left(\Delta y^2\right).$$

Due to the discontinuous nature of the numerical solution $\bar{U}_i$, the normal flux

$F_{i+1/2} = F(U_{i+1/2})$ is not defined on the cell interface $\partial\Omega_{i+1/2}$. The usual strategy is to define the flux on the cell interface in terms of a numerical flux $F_{i+1/2} = \mathcal{F}_{i+1/2}$.

9.1.2 Numerical fluxes

The numerical flux function $\mathcal{F}_{i+1/2}$ at the cell interfaces is obtained by solving a local Riemann problem with initial data $\overline{U}_i$, $\overline{U}_{i+1}$, given by the adjacent cells [54][110]. However, solving the exact Riemann problem is computationally expensive, therefore in most cases, approximate Riemann solvers are used.

Roe solver

Roe [81] introduced an approximate Riemann solver, which resolves jump discontinuities solely in terms of shock waves. In the standard Roe flux, the numerical flux is defined as [54][110]

$$\mathcal{F}_{i+1/2} = \frac{1}{2}\left[F\left(\overline{U}^{(-)}_{i+1/2}\right) + F\left(\overline{U}^{(+)}_{i+1/2}\right)\right] - \frac{1}{2}\mathcal{F}_{\mathcal{D}},$$

where $\overline{U}^{(-)}_{i+1/2}$ and $\overline{U}^{(+)}_{i+1/2}$ are the left and right limits of U on the neighboring element sharing the boundary $\partial\Omega_{i+1/2}$ and the numerical dissipation term $\mathcal{F}_{\mathcal{D}}$ is given by

$$\mathcal{F}_{\mathcal{D}} = |\tilde{A}|\left(\overline{U}^{(+)}_{i+1/2} - \overline{U}^{(-)}_{i+1/2}\right) = T|\Lambda|T^{-1}\left(\overline{U}^{(+)}_{i+1/2} - \overline{U}^{(-)}_{i+1/2}\right). \tag{9.3}$$

Here, $\tilde{A}$ is the flux Jacobian evaluated by Roe's average state, which is the average of $\overline{U}^{(-)}_{i+1/2}$ and $\overline{U}^{(+)}_{i+1/2}$. The calculation of Roe's averaged quantities and the various properties that it satisfies are outlined in detail in [13]. Furthermore, $|\Lambda|$ in (9.3) is the diagonal matrix consisting of the absolute eigenvalues is $\tilde{A}$, and T is the matrix of corresponding eigenvectors.

In the Roe type of flux, the dissipative term depends on the eigenvalue decomposition of the flux Jacobian. For more complex problems (e. g., higher order moment equations), the computation of the eigenvectors can be very tedious. In those cases, some approximations to the upwind scheme must be used.

Krylov–Riemann solver

Torrilhon [115] developed a Krylov–Riemann solver to approximate the upwind Riemann solver for the non-linear flux functions. The Krylov–Riemann numerical flux

relies on the successive approximations for the dissipation vector $\mathcal{F}_{\mathcal{D}}$ by projecting it on a Krylov subspace generated by the flux Jacobian matrix $\tilde{A}$ and the vector $\left(\overline{U}^{(+)}_{i+1/2} - \overline{U}^{(-)}_{i+1/2}\right)$. This approximate Riemann solver does not require a direct computation of full eigenvalue decomposition of the flux Jacobian. Thus, it is particularly suited for the large and complex systems such as higher order moment equations.

Kinetic Flux Vector Splitting scheme

The Kinetic Flux Vector Splitting (KFVS) schemes [2] provide an alternative route to construct the numerical flux function $\mathcal{F}_{i+1/2}$ at the cell interfaces. These schemes use the microscopic kinetic background of the physical equations to derive macroscopic numerical methods. This is done by representing the unknowns U as the average of a microscopic distribution function f.

Variants of the kinetic schemes are proposed in literature, for example, in [125] Xu et al. used a BGK-like model to construct solutions for the Navier-Stokes equations. We consider the scheme proposed in [95]. In this KFVS scheme, we first construct the particle distribution function on the cell interface $f_{i+1/2}$ as

$$f_{i+1/2} = \begin{cases} f^{(-)}_{i+1/2}\left(c_i, x_i, t\right), & c_y \geqslant 0 \\ f^{(+)}_{i+1/2}\left(c_i, x_i, t\right) & c_y \leqslant 0. \end{cases}$$

The numerical flux across the cell interface is then constructed by taking suitable moments, as

$$\mathcal{F}^{\mathrm{KFVS}} = \int \Psi c_y f_{i+1/2} d\mathbf{c} = \int_{c_y \geqslant 0} \Psi c_y f^{(-)}_{i+1/2} d\mathbf{c} + \int_{c_y \leqslant 0} \Psi c_y f^{(+)}_{i+1/2} d\mathbf{c}, \tag{9.4}$$

where $f^{(-)}_{i+1/2}$ and $f^{(+)}_{i+1/2}$ are the distribution functions of particles passing through the cell interface from left and right, respectively, i.e.

$$f^{(\pm)}_{i+1/2} = f_g\left(\overline{U}^{(\pm)}_{i+1/2}\right).$$

Here, f_g is the velocity distribution function of the gas. Furthermore, the velocity function $\Psi\left(c_i\right)$ must be selected such that integrals in (9.4) yield the convective flux F.

To evaluate integrations in Eq. (9.4), a specific model for the distribution function f_g, and the velocity function Ψ are required. For the 13 moment system, for instance

R13 or Grad 13, it suffices to set $f_g = f_{\mathrm{G13}}$ from equation (3.5), and

$$\Psi = \left\{1, c_x, c_y, \frac{1}{2}c^2, c_x c_x, c_x c_y, c_y c_y, c^2 c_x, c^2 c_y\right\}.$$

Accordingly, for the NSF and R10 models, the Maxwellian distribution and the Gaussian distribution (3.32), respectively, are the proper choices for f_g.

9.1.3 Spatial reconstruction procedure

The calculation of the numerical fluxes $\mathcal{F}_{i+1/2}$ with high-order accuracy requires the knowledge of the face averages of $\overline{U}^{(-)}_{i+1/2}$ and $\overline{U}^{(+)}_{i+1/2}$. For a first-order scheme, it is sufficient to set the cell interface values equal to the cell value, i.e.,

$$\bar{U}^{(-)}_{i+1/2} = \bar{U}_i \quad \text{, and} \quad \bar{U}^{(+)}_{i+1/2} = \bar{U}_{i+1}.$$

In higher order finite volume method, however, these are computed using the cell values interpolated from the neighboring cells. For a second order accuracy in space, we use a linear reconstruction of the cell interface values $\bar{U}^{(-)}_{i+1/2}$and $\bar{U}^{(+)}_{i+1/2}$, defined as

$$\bar{U}^{(-)}_{i+1/2} = \left(\frac{4\overline{U}_i + \overline{U}_{i+1} - \overline{U}_{i-1}}{4}\right), \quad \bar{U}^{(+)}_{i+1/2} = \left(\frac{4\overline{U}_{i+1} - \overline{U}_{i+2} + \overline{U}_i}{4}\right). \tag{9.5}$$

It is well known that the polynomial reconstruction does not respect the Total Variation Diminishing (TVD) property and can therefore lead to oscillations near discontinuities [54, 110]. Limiters have therefore been developed to recover the TVD property and avoid the spurious oscillations near shocks or discontinuities.

In this work, we mainly used minmod and van-Leer limiters . We refer to [54, 110] for more details and [14] for an exhaustive analysis of reconstruction schemes.

9.1.4 Discretization of the viscous fluxes

Incorporating the viscous fluxes $F^{\nu}_{i+1/2}$ into the semi-discrete equation (9.2) requires the evaluation of the spatial derivatives at the cell interfaces. Here, for the sake of implementational simplicity, we use a second-order central difference to approximate

the spatial derivatives on the cell interface $\partial\Omega_{i+1/2}$,

$$F^{\nu}_{i+1/2}\left(U_{i+1/2},\, \partial_y U_{i+1/2}\right) = F^{\nu}_{i+1/2}\left(\frac{\overline{U}_i + \overline{U}_{i+1}}{2}, \frac{\overline{U}_{i+1} - \overline{U}_i}{\Delta y}\right) + \mathcal{O}\left(\Delta y^2\right).$$

9.1.5 Boundary Conditions

The boundary conditions are implemented using the ghost cell approach [54] in which a virtual cell is created next to the boundary face, as illustrated in Fig. (9.1). To impose certain boundary conditions, the values of the dependent variables at the ghost points must be specified. For example, the normal component of the flow velocity at a solid boundary is zero. This condition is implemented by taking the normal component of velocity at the ghost cells as

$$v_y|_{-1} = -v_y|_1, \text{ and } \quad v_y|_{N+1} = -v_y|_N.$$

The implementation of the boundary conditions is performed in two steps. In the first step, the variables at ghost points are determined from inner nodes using an extrapolation,

$$\overline{U}_{-1} = 3\overline{U}_1 - 3\overline{U}_2 + \overline{U}_3, \text{ and } \quad \overline{U}_{N+1} = 3\overline{U}_N - 3\overline{U}_{N-1} + \overline{U}_{N-2},$$

such that

$$\begin{aligned} \frac{\overline{U}_1 + \overline{U}_{-1}}{2} &= \overline{U}_{1/2} + \mathcal{O}\left(\Delta y^2\right), \quad \frac{\overline{U}_{N+1} + \overline{U}_N}{2} = \overline{U}_{N+1/2} + \mathcal{O}\left(\Delta y^2\right), \text{ and} \\ \frac{\overline{U}_1 - \overline{U}_{-1}}{\Delta y} &= \partial_y \overline{U}_{1/2} + \mathcal{O}\left(\Delta y^2\right), \quad \frac{\overline{U}_{N+1} - \overline{U}_N}{\Delta y} = \partial_y \overline{U}_{N+1/2} + \mathcal{O}\left(\Delta y^2\right). \end{aligned}$$

In the second step, the odd fluxes in the y-direction (e.g., v_y, σ_{xy}, q_y), are replaced with the boundary conditions (4.13a)–(4.13b). Similarly, for the diffusive fluxes on the boundary, the odd fluxes (e.g., m_{xxy}, m_{yyy}, and R_{xy}) for the y-direction, are replaced by the appropriate boundary conditions (4.13c)–(4.13f), whereas even fluxes, such as m_{xxx}, m_{xyy}, R_{xx}, and R_{yy}, are determined from the inner nodes from the last time step.

9.1.6 Time Discretization

The simplest time discretization that can be employed in (9.2) is by the Euler scheme

$$\overline{U}_i^{n+1} = \overline{U}_i^n - \frac{\Delta t}{\Delta y}\left(\mathcal{F}_{i+1/2}^n - \mathcal{F}_{i-1/2}^n\right) - \frac{\Delta t}{\Delta y}\left(F_{i+1/2}^{n\ \nu} - F_{i-1/2}^{n\ \nu}\right) + \frac{\Delta t}{\mathrm{Kn}}\overline{\mathcal{S}}_i,$$

where $\Delta t = t^{n+1} - t^n$ for all $n \in \mathbb{N}$, is the time discretization step size. The discretization step size Δt is chosen in such a way that the CFL condition is satisfied [111], i.e.,

$$\Delta t = \frac{1}{2}\frac{\Delta y^2}{(\mathrm{c}_{\max}\Delta y + 2\mathrm{Kn})}. \tag{9.6}$$

Here, $\mathrm{c}_{\max}$ is the maximum eigenvalue of the flux Jacobian matrix $\tilde{A} = \frac{\partial F}{\partial U}$. For the R13–moment equations the explicit form of $\mathrm{c}_{\max}$ is unavailable. Therefore, for the R13–moment equations, $\mathrm{c}_{\max}$ is approximated by $1.3\mathrm{c}_{\max}^{'}$, where $\mathrm{c}_{\max}^{'}$ is the maximum eigenvalue for the Levermore 10 moment equations, evaluated explicitly in [13].

On the other hand, Heun's method uses an Euler method to make an intermediate prediction for the solution to the PDE and then uses a trapezoidal method to correct this intermediate value in order to obtain second order in Δt accuracy, i.e.,

$$\begin{aligned}
\overline{U}_i^{*} &= \overline{U}_i^n - \frac{\Delta t}{\Delta y}\left(\mathcal{F}_{i+1/2}^n - \mathcal{F}_{i-1/2}^n\right) - \frac{\Delta t}{\Delta y}\left(F_{i+1/2}^{n\ \nu} - F_{i-1/2}^{n\ \nu}\right) + \frac{\Delta t}{\mathrm{Kn}}\overline{\mathcal{S}}_i^n, \\
\overline{U}_i^{n+1} &= \frac{1}{2}\left[\overline{U}_i^n + \overline{U}_i^{*} - \frac{\Delta t}{\Delta y}\left(\mathcal{F}_{i+1/2}^{*} - \mathcal{F}_{i-1/2}^{*}\right) - \frac{\Delta t}{\Delta y}\left(F_{i+1/2}^{*\ \nu} - F_{i-1/2}^{*\ \nu}\right) + \frac{\Delta t}{\mathrm{Kn}}\overline{\mathcal{S}}_i^{*}\right]
\end{aligned}$$

In this study, we shall use Heun's method for the time discretization in (9.2).

9.2 Numerical test problems

In this section we present several numerical results that demonstrate the performance of the scheme constructed above.

9.2.1 1D Sod Shock Tube

In this test case, we apply KFVS scheme to the linear G13 and R13 equations, and compare with the upwind scheme [54]. To access such an issue, a classical Sod shock

tube problem is solved using the initial condition

$$\rho_0 = \begin{cases} 2 & : -1/4 < x < 1/4 \\ 1 & : \text{otherwise} \end{cases} \tag{9.7a}$$

$$\theta_0 = 1, \quad v_0 = 0. \tag{9.7b}$$

Figure (9.2) illustrates the density ρ (left) and temperature θ (right), computed

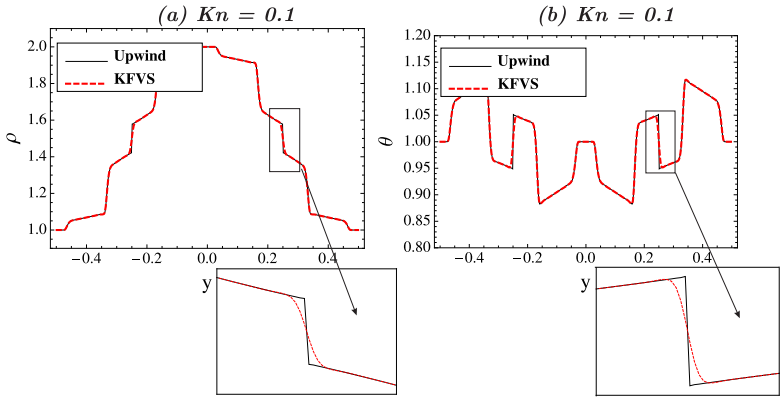

Figure 9.2: Linear G13 equations: comparison of the numerical diffusion. in (a) density ρ and (b) temperature θ. Approximation obtained by the upwind solver and KFVS.

via the upwind and KFVS schemes, for Kn $= 0.1$, $\Delta x = 0.0025$, $\Delta t = 7.7 \times 10^{-7}$ at $t = 0.1$, where the van-Leer limiter [54] was used for the reconstruction. In the insets of Fig. (9.2), we show the magnified density and temperature profiles. One observes that the details of the shock are not captured with the KFVS scheme, due to the numerical dissipation. Although not shown here, applications with minmod limiter functions lead to similar conclusions and no spurious oscillations is visually observed for both schemes, either with the minmod limiter function or with the van-Leer limiter function. This is due to the hyperbolic nature of the Grad 13 equations, which produce shocks.

On the other hand, if the KFVS and upwind methods are applied to the R13 equations, we obtain the results shown in Fig. 9.3, where, (a) the density and (b) the temperature are compared for KFVS (dashed red) against the upwind solution (solid lines). The solutions obtained with the two schemes are compared, at $t = 0.1$, for Kn $= 0.1$, $\Delta x = 0.0025$, $\Delta t = 7.7 \times 10^{-7}$.

As one can observe, in Figure (9.3), the KFVS scheme gives results which are in

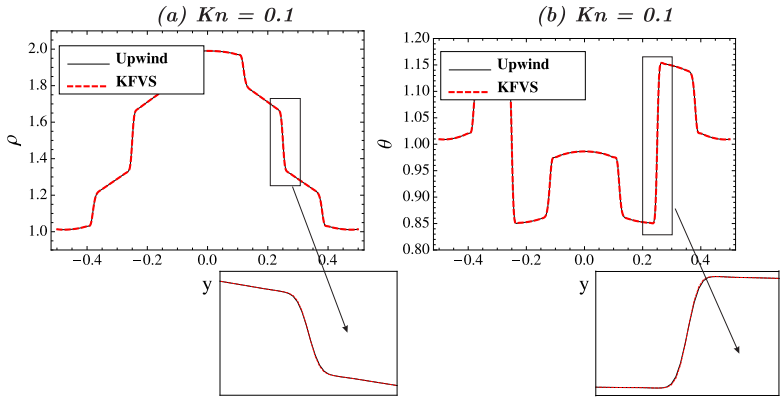

Figure 9.3: Linear R13 equations: comparison of the numerical diffusion. in (a) density ρ and (b) temperature θ. Approximation obtained by the upwind solver and KFVS.

good agreement with the upwind solver. The linear R13 equations are parabolic in nature, thus, they produce smooth solutions.

9.2.2 Convergence test (linear)

The aim of this section is to test the convergence rate of the proposed scheme when applied to the linear R13 equations for the Couette flow problem, as described in Section 6.2. More precisely, we define L^1-errors as

$$E_2(\psi) = \Delta y \sum_{i=1}^{N} |\psi_i^{(\Delta y)} - \psi_i^{(exact)}|, \tag{9.8}$$

where ψ is the quantity of interest, $\psi_i^{(\Delta y)}$ is the solution obtained using a mesh of size Δy, and $\psi_i^{(exact)}$ is the exact solution.

Errors in the tangential velocity v_x, tangential heat flux q_x and shear stress σ_{xy}, computed via the upwind and KFVS schemes are shown in Fig. 9.4(a) and Fig. 9.4(b), respectively, for the Couette flow at a given value of Kn $= 0.1$ and $v_w = 0.4195$.

As one can observe, both the schemes show approximately second order convergence. Our studies revealed that the convergence behavior is independent of Kn, as long as Kn $\gtrsim 0.01$. However, the convergence behavior suffers from the phenomenon of order reduction in the stiff regime (Kn $\lesssim 0.01$). Pareschi and Russo [77] suggested to employ the implicit-explicit (IMEX) Runge-Kutta scheme for systems with stiff relaxation. They utilize explicit discretization for the non-stiff part and an im-

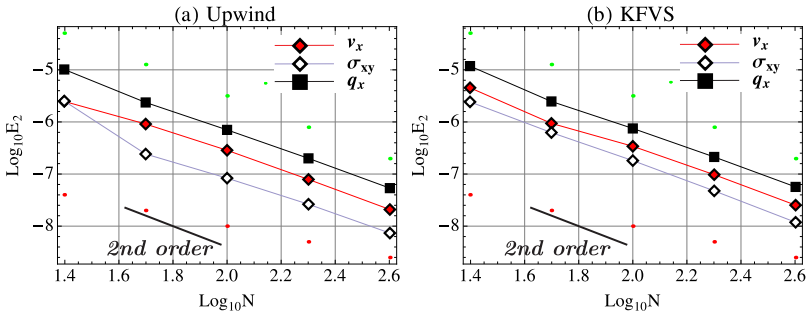

Figure 9.4: Convergence rates in tangential velocity, shear stress and the tangential heat flux, achieved with Kn= 0.1 for linear R13 equations: upwind (left) and KFVS (right) scheme.

plicit discretization for the stiff relaxation part. For the scope of this thesis, we shall compute solutions for Kn $\gtrsim$ 0.01 only, and therefore use Heun's fully explicit time discretization system.

9.2.3 Convergence test (non-linear)

Next, we present some numerical results for the non-linear Couette problem based on the discretization of the non-linear R13 equations. Note that, as no analytic solutions are known for the nonlinear R13 system, we shall compare the obtained results with simulations performed on very fine grids. We use the discretization at $N = 400$ as reference solution.

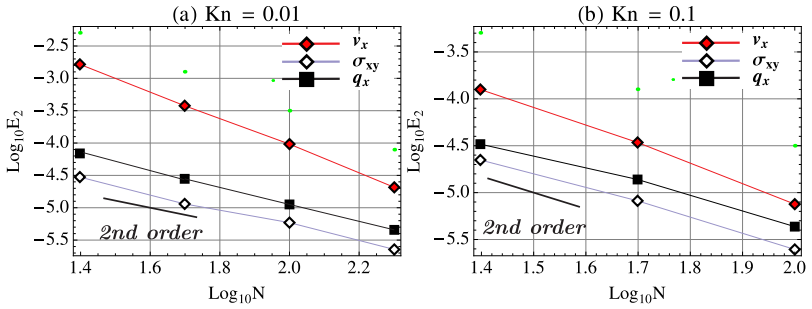

Figure 9.5: Convergence rates for tangential velocity, shear stress and the tangential heat flux, achieved with KFVS scheme for non linear R13 equations: Kn= 0.01 (left) and Kn= 0.1 (right).

Again, for the steady Couette flow with $v_w = 1.2586$, we show in Fig. 9.5 the errors for the tangential velocity v_x, tangential heat flux q_x and shear stress σ_{xy}, computed

using the KFVS scheme, for (a) Kn = 0.01 and (b) Kn = 0.1. In both the cases convergence rates between 1.63 and 1.91 are observed.

9.2.4 The planar Couette flow

Now, we present some numerical results performed for the non-linear R13 equations using FVM framework, and compare them against the finite difference (FD) discretization described in Chapter 6. We consider a gas between two parallel plates, see Fig. 6.1. Initially, the gas is at rest and all macroscopic quantities are uniform, with $\rho_0 = 1$, $\theta_0 = 1$ and the remaining quantities equal to zero. The temperature of both the plates is at reference temperature and full accommodation is assumed ($\chi = 1$).

For $t > 0$, both plates start moving in opposite direction with $v_w(\pm 0.5) = \pm 0.4195$. The transient behaviors of the macroscopic quantities are presented in Fig. 9.6, for Kn = 0.01. The profiles of (a) velocity v_x, (b) temperature θ, (c) shear stress σ_{xy}, (d) normal stress σ_{yy}, (e) tangential heat flux q_x and (f) normal heat flux q_y, are shown in Fig. 9.6, at different times, up to the steady state condition.

The steady state solution obtained from the FD approximation in Chapter 6, where no time stepping was required, is represented by the symbols. The temperature profiles in Fig. 9.6(b) indicate that the temperature increases monotonically until the steady state is reached at about $t = 22$. It should be noted that every macroscopic quantity relaxes towards steady state with different relaxation time.

Figure 9.7 shows the time evolution of (a) velocity v_x, (b) temperature θ, (c) shear stress σ_{xy}, (d) normal stress σ_{yy}, (e) tangential heat flux q_x and (f) normal heat flux q_y distributions for Kn = 0.1. The corresponding steady state solution obtained from FD approximation is represented by the symbols and the solid lines mark the results obtained from FVM method.

The steady state is reached at $t = 6.5$, where in all cases the dark red line denotes the steady state limit. It follows that a good agreement is obtained between both the methods.

At time $t = 0.5$, due to the friction created at the boundary, the temperature near the boundary is higher and temperature profile is concave, as we can see in Fig. 9.7(b). As time progresses, the temperature is redistributed due to the normal heat flux, see Fig. 9.7(c), and eventually takes a steady state convex profile.

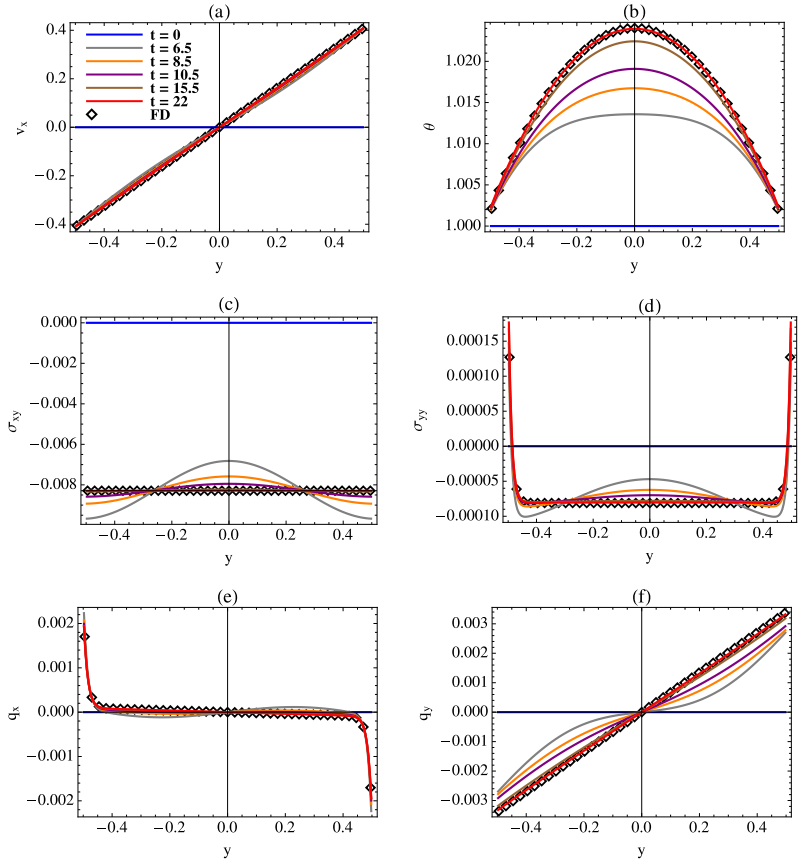

Figure 9.6: Time evolution of (a) velocity v_x, (b) temperature θ, (c) shear stress σ_{xy}, (d) normal stress σ_{yy}, (e) tangential heat flux q_x and (f) normal heat flux q_y, at Kn $= 0.01$ for non-linear R13 equations. The corresponding steady-state solutions obtained from FD approximation are represented by the symbols.

9.3 Oscillatory Couette flow

In oscillatory Couette flow, one considers a gas confined between two infinite parallel plates, where the upper plate oscillates along the x-direction, and the other plate is stationary [78, 40, 84], see Fig. (9.8). Initially, the gas is at rest and at $t > 0$ the upper plate starts oscillating with velocity $v^w(t) = U_0 \sin(\omega t)$, where ω and U_0 are the dimensionless frequency and amplitude of the oscillations, respectively. The plates are assumed to be isothermal at temperature $\theta_0 = 1$ and the gas molecules are diffusely reflected on the plates. The flow is characterized by the Knudsen number Kn and the oscillation frequency ω. In addition, we can also use the Stokes number $\mathrm{St} = \sqrt{\omega/\mathrm{Kn}}$ to investigate the transient behavior.

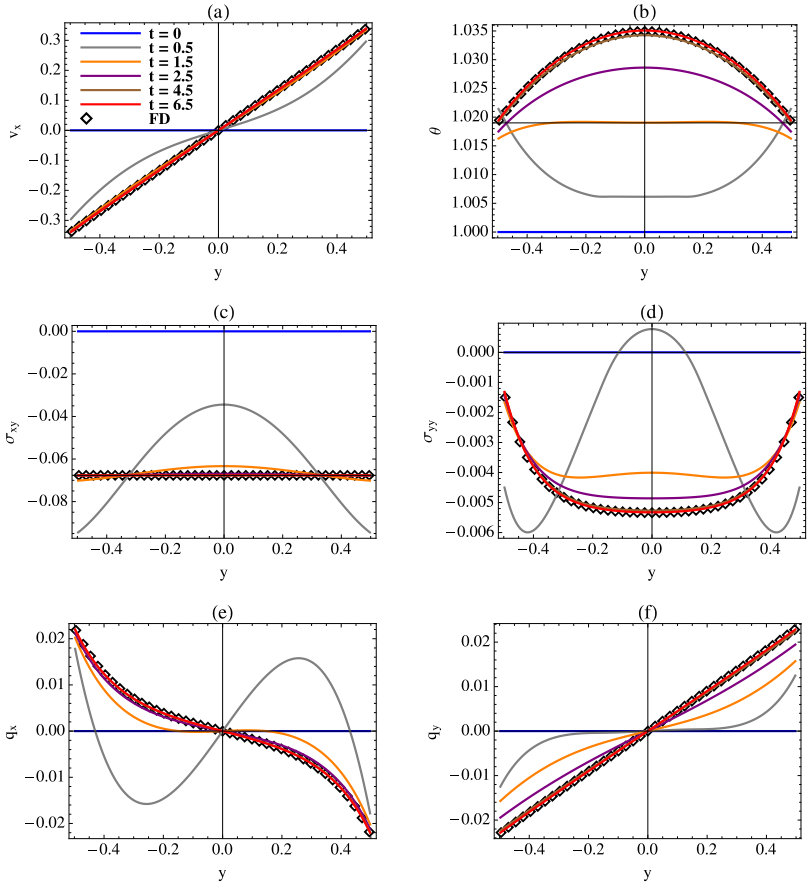

Figure 9.7: Time evolution of (a) velocity v_x, (b) temperature θ, (c) shear stress σ_{xy}, (d) normal stress σ_{yy}, (e) tangential heat flux q_x and (f) normal heat flux q_y, at Kn = 0.1 for non-linear R13 equations. The corresponding steady state solution obtained from FD approximation is represented by the symbols.

Analytic solutions using the R13 and NSF equations for the transient Couette flow problem are given in Taheri et al. [106]. These solutions are obtained by considering small deviations from the equilibrium state (i.e., U_0, St $\ll 1$).

However, the results based on the linearized equations show disagreements with the DSMC data [40], where the differences between the DSMC and analytical results was attributed to the non-linearity of the problem [106]. This section aims to find the numerical solution of the non-linear R13, R10 and NSF equations for the transient Couette flow, using the numerical scheme discussed above, and to compare them with DSMC solutions [40].

Three pairs of Knudsen and Stokes numbers are selected, Case 1: ($\widetilde{\text{Kn}} = 0.1$, St $= 4$), Case 2: ($\widetilde{\text{Kn}} = 0.2$, St $= 2$) and Case 3: ($\widetilde{\text{Kn}} = 0.4$, St $= 1$), which are

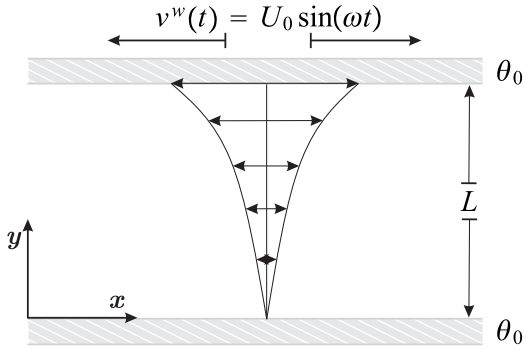

Figure 9.8: Schematic of oscillatory Couette flow: Gas confined between two infinite plates in the $yz-$plane, separated by a distance L in the $x-$direction.

those considered in the DSMC simulations of [40]. Notice the difference between the definitions of the Knudsen number defined in [40] $\widetilde{\mathrm{Kn}}$ and Kn used in this dissertation, which are related through the relation $\mathrm{Kn} = \widetilde{\mathrm{Kn}}\sqrt{2/\pi}$.

The results presented here are for $U_0 = 0.1$, at four points in time during a period of oscillation, corresponding to $\omega t = t_0$, $t_0 + \pi/2$, $t_0 + \pi$, and $t_0 + 3\pi/2$, where t_0 is the time before a quasi-steady state (harmonic state) is established. For all the solutions presented below, $t_0 = 16\pi$ has been taken, i.e., we show results after eight oscillation cycles.

Figure 9.9 shows the velocity v_x, normalized with U_0, obtained from (a) the R13, (b) R10 and (c) NSF equations. In Fig. 9.9, first, second and third rows represent Case 1, Case 2, and Case 3, respectively. In Fig. 9.9, indicated values of the Knudsen number correspond to the definition in [40]. The circles represent the DSMC data from [40].

For Case 1 in the first row of Fig. 9.9, where the case is close to hydrodynamics regime, all three theories yield good agreement with the DSMC solutions [40]. For Case 2 and Case 3, where non-equlibrium effects are strong, some differences to the DSMC results are observed. For Case 2, as depicted in second row of the Fig. (9.9), NSF results show less curvature in the velocity whereas the R13 and R10 results show over all good agreement with the DSMC.

For Case 3, as shown in the last row of Fig. 9.9, the R13 solutions show less curvature near the boundary, due to lack of Knudsen layers. However, R13 solutions in the bulk give good agreement with the DSMC. Furthermore, all the results presented in Fig. 9.9 show that, indeed, considering non-linear terms provide a better concurrence

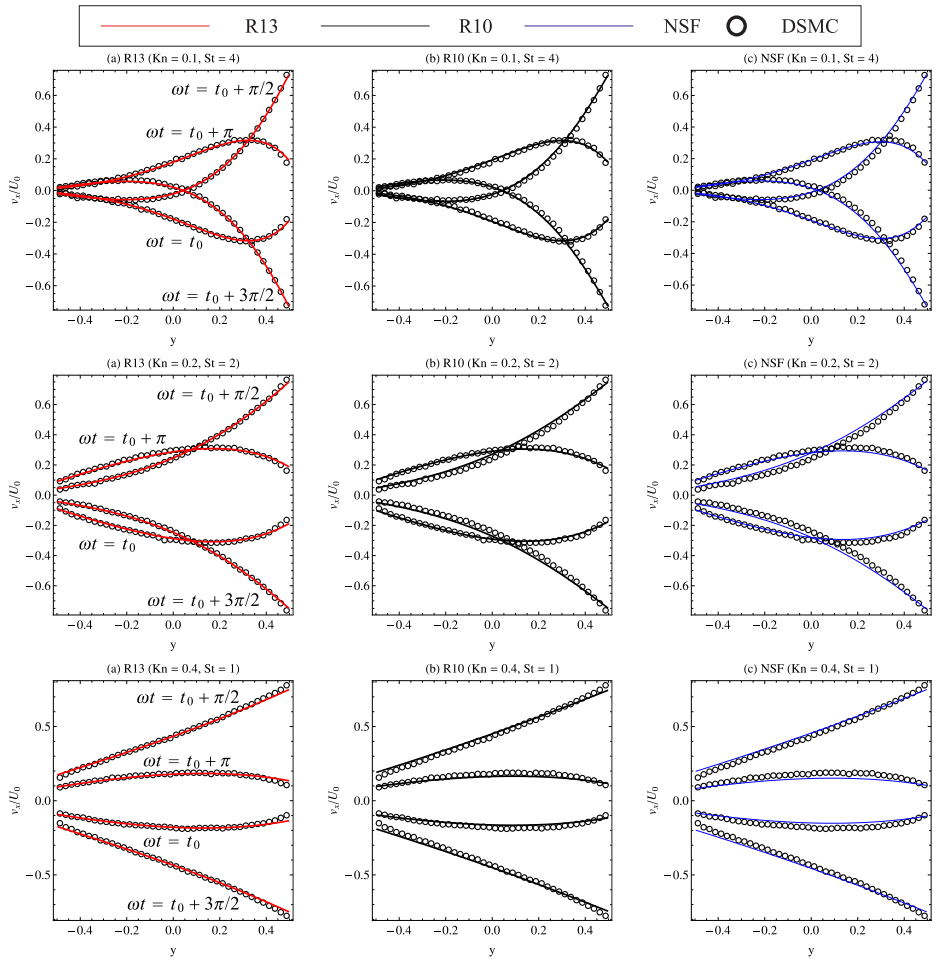

Figure 9.9: The velocity profiles obtained from (a) the R13, (b) R10 and (c) NSF equations at four points in time, corresponding to $\omega t = t_0$, $t_0 + \pi/2$, $t_0 + \pi$, and $t_0 + 3\pi/2$. First, second and third rows represent the Case 1, Case 2 and Case 3, respectively.The circles repersent the DSMC data from [40].

with the DSMC solutions.

Figure 9.10 shows the variations of the shear stress σ_{xy} (top row) and tangential heat flux q_x (bottom row) obtained from the R13, R10, and NSF equations for the Case 1, Case 2 and Case 3. In each subplot, the profiles of σ_{xy} or q_x are shown at different times corresponding to $\omega t = t_0$, $t_0 + \pi/2$, $t_0 + \pi$, and $t_0 + 3\pi/2$. For the shear stress σ_{xy}, the R13, R10 and NSF equations agree in all three cases.

Furthermore, the tangential heat flux, q_x, vanishes in NSF theory, as clear from Fig. 9.10. By comparing the results of the R13, R10 and NSF equations, in Fig. 9.10, we conclude that non-zero q_x is a rarefaction effect given by Knudsen layers and other

non-equilibrium effects.

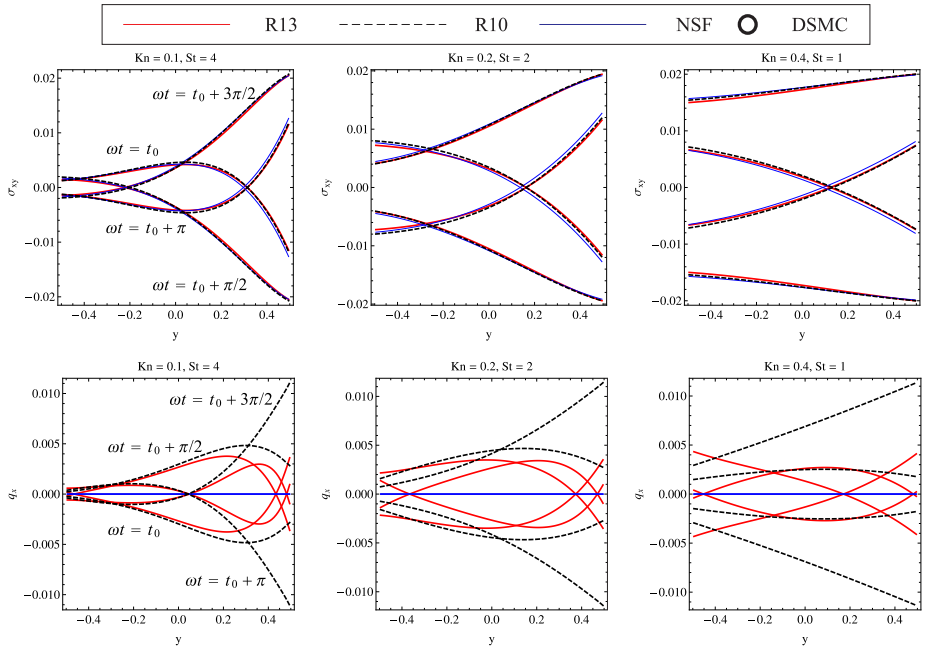

Figure 9.10: Variation of the shear stress σ_{xy} (top row) and tangential heat flux q_x (bottom row), obtained from the R13, R10, and NSF equations for Case 1, Case 2 and Case 3. The results are presented at four points in time, corresponding to $\omega t = t_0$, $t_0 + \pi/2$, $t_0 + \pi$, and $t_0 + 3\pi/2$.

Figure 9.11 shows the amplitude of the normalized velocity v_y/U_0, obtained by numerical solution of the R13, R10, and the NSF equations, for three different values of the Stokes number $\mathrm{St} = 4, 8, 12$. The results obtained for $\widetilde{\mathrm{Kn}} = 0.1$ and $\widetilde{\mathrm{Kn}} = 0.2$ are shown in first and second rows, respectively.

We can see from the Fig. 9.11 that the amplitude of the normalized velocity decreases as the Stokes number increases. By increasing the Stokes number, we increase the friction at the wall, as a result velocity decreases. It is also visible in the Fig. 9.12, which shows that the amplitude of the normalized shear stress σ_{xy}/U_0 grows as the Stokes number becomes large.

9.4 Gas flow through a channel of finite length

In this section, we shall present our preliminary results for the linear R13 equations, obtained using the in/out flow boundary conditions derived earlier in Section 4.3.2.

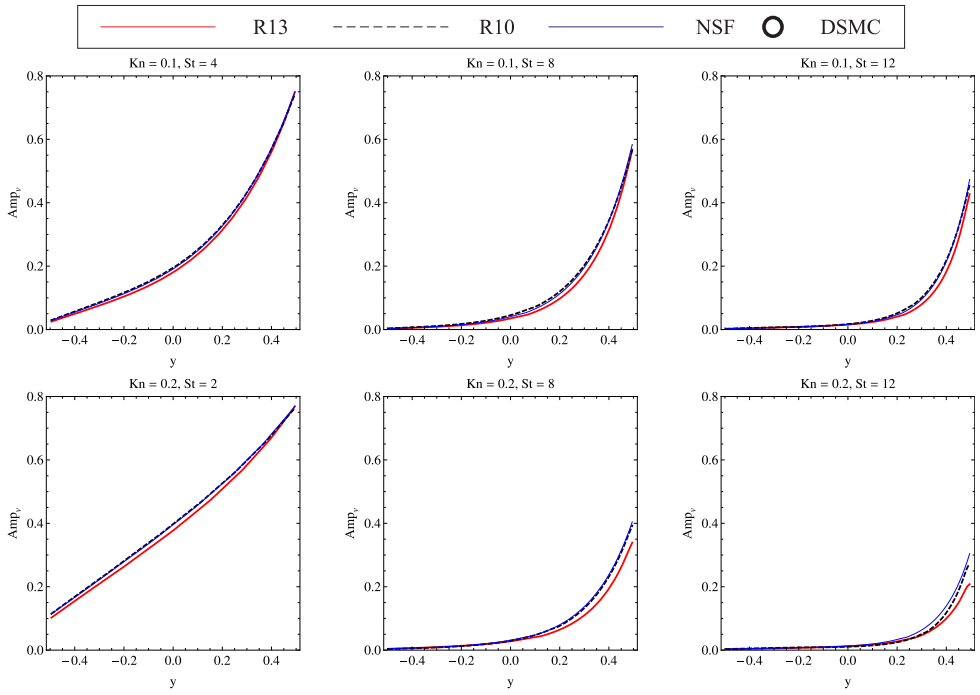

Figure 9.11: Variation of the shear stress σ_{xy} (top row) and tangential heat flux q_x (bottom row), obtained from the R13, R10, and NSF equations for Case 1, Case 2 and Case 3. The results are presented at four points in time, corresponding to $\omega t = t_0$, $t_0 + \pi/2$, $t_0 + \pi$, and $t_0 + 3\pi/2$.

The numerical scheme used here is a straightforward extension of the FVM scheme described earlier in this chapter.

Consider two large containers connected by an array of short channels of length L and height H as shown in Fig. 9.13. The container on the left contains a gas at pressure p_0, while that on the right contains the gas at a smaller pressure $p_1 < p_0$; further the temperatures of the gas in both the containers are at the reference temperature θ_0. The walls of both the containers are maintained at temperature θ_0.

The flow is assumed to be symmetric about axes $y = 0$, and $y = R$. In order to optimize the computational time, the symmetry boundary conditions are used and only the lower half of the domain is considered, see Fig. 9.13(b) for the computational domain and the imposed boundary conditions.

We assume that the pressure difference between two containers is small, i.e., $\Delta p = p_0 - p_1 \ll p_0$, so that the equations may be linearized about an equilibrium state of uniform pressure p_0 and temperature θ_0. The flow is characterized by the pressure ratio p_1/p_0, aspect ratio $a = L/H$, the spacing between the channels $2R$ and the

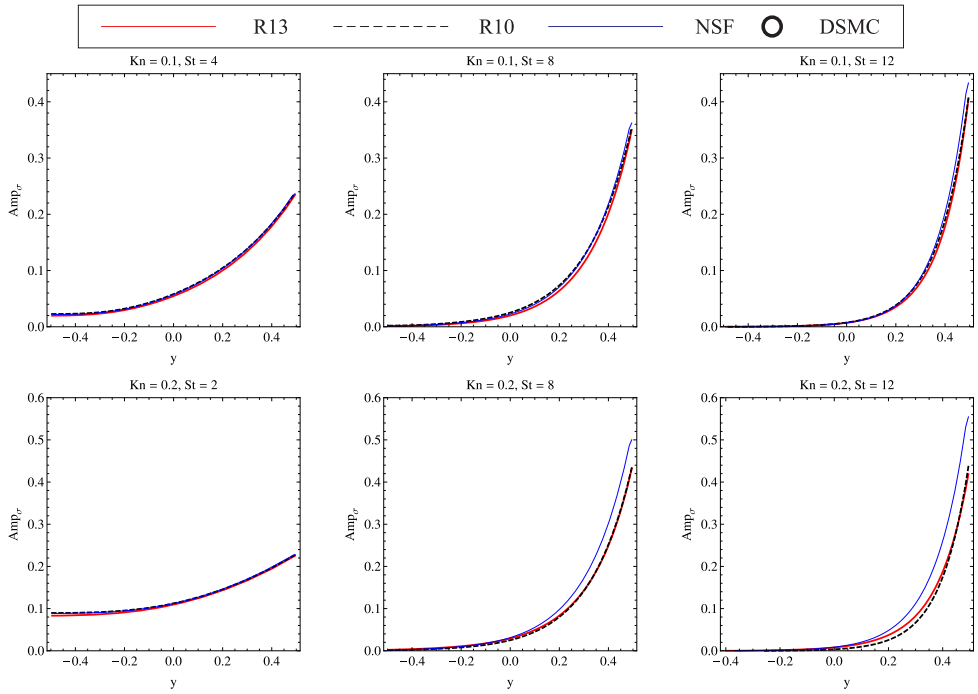

Figure 9.12: Amplitude of the normalized shear stress σ_{xy}/U_0 along y, for different Stokes numbers.

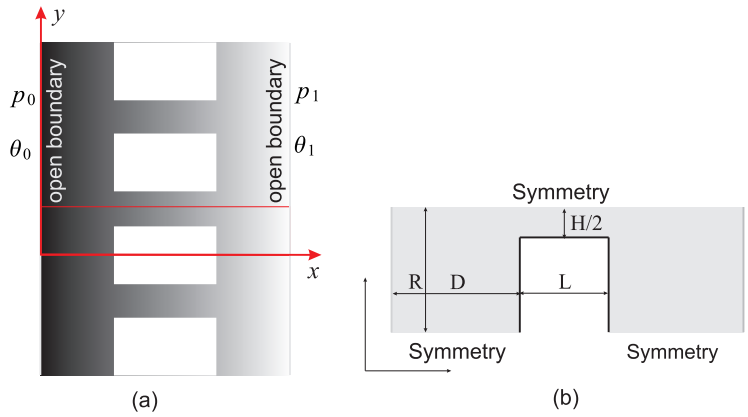

Figure 9.13: (a) Schematic of the flow; and (b) imposed boundary conditions for a single channel.

Knudsen number Kn, defined by considering H as the reference length scale. Here, we shall consider $\Delta p = 0.1$, $a = 4$, $R/H = 2$ and $\mathrm{Kn} = 0.05, 0.1$. Accordingly, the channel lies between $x = 3$ and 7.

The computational domain was covered with a regular grid with constant mesh size

$\Delta x = \Delta y = 0.01$. The calculations were carried out until all macroscopic quantities ρ, v_x and θ reached the steady-state. The computed velocity (normalized with Δp) and pressure variations along the symmetry axis ($y = 2$) are depicted in Fig. 9.14 (a) and Fig. 9.14 (b), respectively.

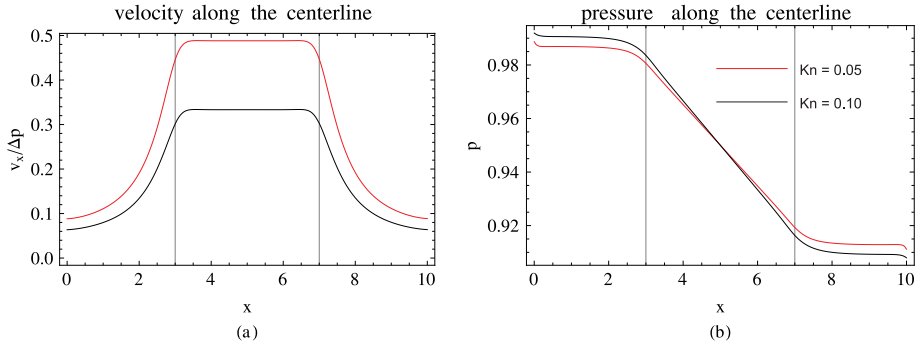

Figure 9.14: (a) Velocity and (b) pressure distributions along the symmetry axis $y = 2$, for Knudsen number Kn = 0.05 (red curves) and 0.1 (black curves).

Figure 9.14 shows that velocity decreases as Knudsen number increases. Moreover, in Fig. 9.14(b), we notice small pressure jump at the artificial boundaries ($x = 0$ and $x = 10$), which indicates that the computational domain must be further enlarged, i.e., the artificial boundaries are required to be extended further away.

Figure 9.15(a) and Figure 9.15(b) shows the $\sigma_{xy}/\Delta p$ contours and the velocity vector of the gas for Knudsen numbers 0.05 and 1. It is clear from Fig. 9.15 that the shear stress varies linearly across the channel and almost vanishes in the containers. Overall behavior of the axial distribution of shear stress and velocity is qualitatively very similar to the linear Poiseuille flow problem, presented in [108]. We reiterate that these are only preliminary results and need further investigation; this requires comparison with other theories and possibly the derivation of non-linear R13 boundary conditions for in/out flows.

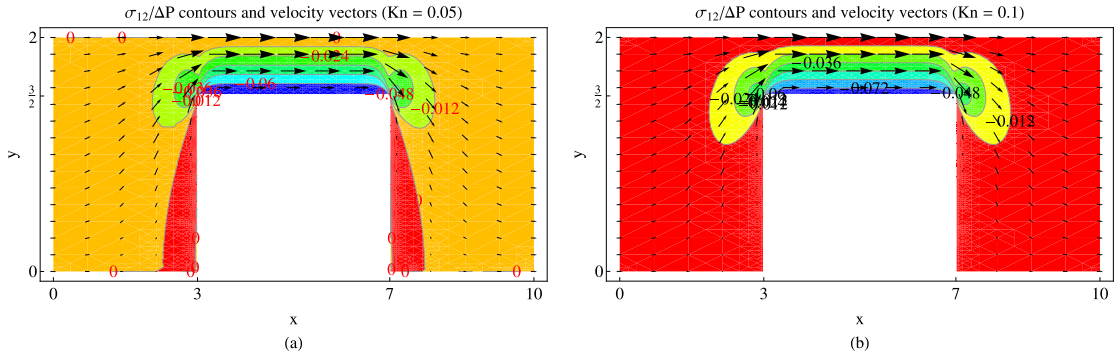

Figure 9.15: Velocity vectors v_i, superimposed on the normalized shear stress $\sigma_{xy}/\Delta p$ contours for $\Delta p = 0.1$, and (a) Kn $= 0.05$ and (b) Kn $= 0.1$.

Chapter 10

Conclusion and Recommendations

This study has been concerned with the application of moment equations to gas flow prediction in moderately rarefied conditions. Such flows are common in many applications, such as those found in MEMS and partial vacuumed devices. It was demonstrated that the moment equations offer valuable insight into the process while their computational cost are several orders of magnitude below that required for the highly accurate DSMC simulations. Another important point in this dissertation is that DSMC and the moment equations inform each other: We can validate the results of the macroscopic equations by comparison to DSMC simulations, and then, in turn, interpret the DSMC results in terms of macroscopic quantities.

Original contributions are listed below:

- We used order of magnitude arguments to rewrite the non-linear part of the R13 equations such that the third order accuracy is maintained, but linear and nonlinear equations require the same number of boundary conditions. This allowed us to obtain numerical solutions of non-linear R13 equations for multi-dimensional boundary value problems.

- We derived a set of regularized 10–moment equations based on the framework of phenomenological linear irreversible thermodynamics. This derivation of the R10 equations is independent of the collision model.

- We proposed a general phenomenological theory of boundary conditions for the R13 and R10 equations. The proposed approach allows us to correct the velocity-slip and temperature-jump coefficients in a systematic way.

- We developed macroscopic adiabatic wall boundary conditions by using the isotropic scattering model. Results obtained by using these boundary conditions yield a satisfactory agreement with the DSMC theory.

- The R13 and NSF equations were applied to solve the lid driven cavity problems for Knudsen numbers up to 0.7. The results compare well with those obtained from more costly solvers for rarefied gas dynamics, such as the IMM and the DSMC method. We observed that the R13 equations yield satisfactory agreement with DSMC data including *anti-Fourier heat flux* for Knudsen number $\lesssim 0.3$. This *cold to hot* heat transfer process was described through the various terms in the R13 equations. For the adiabatic lid driven cavity, in the DSMC results, the heat lines close to the side walls are not parallel to the walls. However, due to the linearity in the boundary conditions, the R13 and NSF results show that the heat lines close to the adiabatic boundaries are parallel to the walls.

- The flow behavior and heat transfer characteristics of a rarefied gas confined in a micro cavity were investigated by solving the R13 equations and NSF equations numerically and comparing the results with DSMC solutions. The results show that for Knudsen numbers below 0.3, the main heat transfer characteristics are described reasonably well by the R13 equations, and NSF equations with slip and jump boundary conditions, with higher accuracy offered by R13. Furthermore, we observed that DSMC shows a bimodal behavior for the normal heat flux along the bottom plate. This behavior of the normal heat flux is correctly predicted by the R13 equations, while the NSF equations fail to capture this. Moreover, the DSMC results show significant flow patterns which are absent in the NSF theory. This convective mechanism in the gas was described in detail through relative terms in the boundary conditions and their respective size. Combined effects of the temperature ratio, and the Knudsen number on the effective heat conductivity and flow structure were examined. The results show that the heat flux increased monotonically with temperature ratio, and the heat flux decreased as the Knudsen number increased. Our results show that the R13 equations yield satisfactory agreement with DSMC data, including flow patterns in the transition regime for Knudsen numbers below 0.3.

- Non-stationary boundary value problems have been solved numerically by us-

ing a finite volume method based on the kinetic flux vector splitting (KFVS) scheme. The KFVS scheme has an advantage over the Roe scheme as it does not require any eigenvalue decomposition of the flux Jacobian, which can be useful for solving larger non-linear systems, such as higher moment equations. In particular, we solved the oscillatory Couette flow problem using the non-linear R13, R10 and NSF equations. We found that the non-linear solutions of the R13 equations offer good agreement with the DSMC solutions for all the cases considered.

- A mathematical analysis of open systems was conducted and—based on the linear R13 equations—we deduced that the R13 system requires 8 and 6 boundary conditions at inflow and outflow, respectively. On a far-field boundary a total of 6 boundary conditions must be prescribed for the linear R13 equations. Some preliminary results for the linear R13 equations, obtained using open flow boundary conditions, were presented. However, an artificial jump in pressure was observed at the artificial boundary. This is an artifact of the computational domain being too small. Nevertheless, overall behavior of axial distribution of shear stress and velocity within the channel was qualitatively similar to the linear planar case of Poiseuille flow.

During the course of research, several ideas and issues were raised. However, due to time constraints, many of these ideas remain unfinished or untouched. They are listed below:

- By using a similar approach as presented in Chapter 4 for the linear case, one can obtain a set of *nonlinear* phenomenological boundary conditions. This will lead to more phenomenological coefficients in the boundary conditions, so that a wide variety of real life gas-surface interaction can be modelled.

- A non-linear adiabatic wall model—as considered in Chapter 4—can be constructed. For example, one can expand the distribution function to second degree (instead of linear), which yields some non-linear terms in the boundary conditions, e.g., frictional heating.

- The in/out flow and open boundary conditions as presented in Chapter 4 need further investigation, and comparison with the existing results.

- In this dissertation, we have considered the R13 equations for simple models (Maxwell molecules, BGK, ES-BGK), for which the derivation of moment equations is comparatively easy, and which are now well established for the linear and non-linear case. Only recently, the R13 equations were extended for the hard-sphere model [105], where presently only the linear equations are available. Already at the hydrodynamic level, different molecular interaction potentials for the collision term yield different transport parameters; e.g., the temperature exponent in viscosity ω for hard spheres is 0.5, for Maxwell molecules it is 1, whereas the measured value of ω is 0.81. It is straightforward to incorporate the different temperature dependence of viscosity and a different Prandtl number into the moment equations. However, for higher moment theories such as R13 or Burnett equations, not only the viscosity and heat conductivity varies with collision model but also other transport parameters change with the molecular interaction potentials [105]. Therefore, it is expected that differences in transport parameters due to different molecular interaction potentials will lead into small differences in transport quantities. The effects of the different interaction potential should be studied in the future; this requires the derivation of R13 boundary conditions for the hard sphere case, which are presently not available.

- An extension of the FVM method to an unstructured mesh is an attractive option. This not only provides greater flexibility for discretizing complex domains but also enables straightforward implementation of adaptive mesh algorithms.

- A promising opportunity for future work is to obtain extended moment equations for gas mixtures, polyatomic molecules, and mixtures of polyatomic gases.

It is an open question whether macroscopic models are adequate approximation strategy for the Boltzmann equation for all Knudsen numbers. The results of the presented research seem to indicate that they can be used best for small to moderate Knudsen numbers. Nevertheless, macroscopic models are still of wide use at the moment for simulations, in particular they can give fast solutions that serve to understand general flow behavior. Moreover, they permit us to understand and develop intuition for unexpected behavior, for instance, non-Fourier heat flux from cold to warm, or flow patterns that are driven by temperature gradients.

Appendix A

Matrix Structure

The original R13 equations (Sec. 3.2.2) can be written in matrix form as

$$\mathcal{A}(U)\frac{\partial U}{\partial x}+\mathcal{B}(U)\frac{\partial U}{\partial y}+\frac{1}{\mathrm{Kn}}P(U)U=0.$$

Here, matrices $\mathcal{A}(U)$ and $P(U)$ are given by

$$\mathcal{A}(U)=\begin{pmatrix}
v_1 & \rho & 0 & 0 & 0 & 0 & 0 & 0 & 0 & 0 & 0 & 0 & 0 & 0 & 0 & 0 \\
\theta & \rho v_1 & 0 & \rho & 0 & 0 & 1 & 0 & 0 & 0 & 0 & 0 & 0 & 0 & 0 & 0 \\
0 & 0 & \rho v_1 & 0 & 0 & 0 & 0 & 1 & 0 & 0 & 0 & 0 & 0 & 0 & 0 & 0 \\
0 & \theta\rho+\sigma_{11} & \sigma_{12} & \frac{3\rho v_1}{2} & 1 & 0 & 0 & 0 & 0 & 0 & 0 & 0 & 0 & 0 & 0 & 0 \\
-\frac{\theta\sigma_{11}}{\rho} & m_{111}+\frac{16q_1}{5} & m_{112}+\frac{2q_2}{5} & \frac{5\theta\rho}{2}+\frac{5\sigma_{11}}{2} & v_1 & 0 & \theta-\frac{\sigma_{11}}{\rho} & -\frac{\sigma_{12}}{\rho} & 0 & \frac{1}{2} & 0 & 0 & 0 & 0 & 0 & \frac{1}{6} \\
-\frac{\theta\sigma_{12}}{\rho} & m_{112}+\frac{7q_2}{5} & m_{122}+\frac{7q_1}{5} & \frac{5\sigma_{12}}{2} & 0 & v_1 & -\frac{\sigma_{12}}{\rho} & \theta-\frac{\sigma_{22}}{\rho} & 0 & 0 & \frac{1}{2} & 0 & 0 & 0 & 0 & 0 \\
0 & \frac{4\theta\rho}{3}+\frac{7\sigma_{11}}{3} & -\frac{2\sigma_{12}}{3} & 0 & \frac{8}{15} & 0 & v_1 & 0 & 0 & 0 & 0 & 0 & 1 & 0 & 0 & 0 \\
0 & 2\sigma_{12} & \theta\rho+\sigma_{11} & 0 & 0 & \frac{2}{5} & 0 & v_1 & 0 & 0 & 0 & 0 & 0 & 1 & 0 & 0 \\
0 & -\frac{2\theta\rho}{3}-\frac{2\sigma_{11}}{3}+\sigma_{22} & \frac{4\sigma_{12}}{3} & 0 & -\frac{4}{15} & 0 & 0 & 0 & v_1 & 0 & 0 & 0 & 0 & 0 & 1 & 0 & 0 \\
-\frac{2\theta q_1}{3\rho} & \frac{10\theta\sigma_{11}}{21} & \frac{5\theta\sigma_{12}}{21} & \frac{2q_1}{3} & \frac{2\theta}{3} & 0 & 0 & 0 & 0 & 0 & 0 & 0 & 0 & 0 & 0 & 0 \\
-\frac{\theta q_2}{2\rho} & \frac{5\theta\sigma_{12}}{21} & \frac{5}{14}\theta(\sigma_{11}+\sigma_{22}) & \frac{q_2}{2} & 0 & \frac{\theta}{2} & 0 & 0 & 0 & 0 & 0 & 0 & 0 & 0 & 0 & 0 \\
\frac{\theta q_1}{3\rho} & -\frac{10}{21}\theta(\sigma_{11}+\sigma_{22}) & \frac{5\theta\sigma_{12}}{21} & -\frac{q_1}{3} & -\frac{\theta}{3} & 0 & 0 & 0 & 0 & 0 & 0 & 0 & 0 & 0 & 0 & 0 \\
-\frac{3\theta\sigma_{11}}{5\rho} & \frac{8q_1}{25} & -\frac{4q_2}{25} & 0 & 0 & 0 & \frac{3\theta}{5} & 0 & 0 & 0 & 0 & 0 & 0 & 0 & 0 & 0 \\
-\frac{8\theta\sigma_{12}}{15\rho} & \frac{16q_2}{75} & \frac{16q_1}{75} & 0 & 0 & 0 & 0 & \frac{8\theta}{15} & 0 & 0 & 0 & 0 & 0 & 0 & 0 & 0 \\
-\frac{\theta(5\sigma_{22}-2\sigma_{11})}{15\rho} & -\frac{4q_1}{25} & \frac{16q_2}{75} & 0 & 0 & 0 & -\frac{2\theta}{15} & 0 & \frac{\theta}{3} & 0 & 0 & 0 & 0 & 0 & 0 & 0 \\
\frac{2\theta\sigma_{12}}{5\rho} & -\frac{4q_2}{25} & -\frac{4q_1}{25} & 0 & 0 & 0 & 0 & -\frac{2\theta}{5} & 0 & 0 & 0 & 0 & 0 & 0 & 0 & 0 \\
-\frac{8\theta q_1}{\rho} & 8\theta\sigma_{11} & 8\theta\sigma_{12} & 20q_1 & 8\theta & 0 & 0 & 0 & 0 & 0 & 0 & 0 & 0 & 0 & 0 & 0
\end{pmatrix}$$

and

$$\mathcal{P}(U) = \begin{pmatrix}
0&0&0&0&0&0 & 0 & 0 & 0 & 0&0&0&0&0&0&0&0 \\
0&0&0&0&0&0 & 0 & 0 & 0 & 0&0&0&0&0&0&0&0 \\
0&0&0&0&0&0 & 0 & 0 & 0 & 0&0&0&0&0&0&0&0 \\
0&0&0&0&0&0 & 0 & 0 & 0 & 0&0&0&0&0&0&0&0 \\
0&0&0&0&\frac{2}{3}&0 & 0 & 0 & 0 & 0&0&0&0&0&0&0&0 \\
0&0&0&0&0&\frac{2}{3} & 0 & 0 & 0 & 0&0&0&0&0&0&0&0 \\
0&0&0&0&0&0 & 1 & 0 & 0 & 0&0&0&0&0&0&0&0 \\
0&0&0&0&0&0 & 0 & 1 & 0 & 0&0&0&0&0&0&0&0 \\
0&0&0&0&0&0 & 0 & 0 & 1 & 0&0&0&0&0&0&0&0 \\
0&0&0&0&0&0 & \frac{5(\sigma_{11}-\sigma_{22})}{126\rho} & \frac{5\sigma_{12}}{126\rho} & -\frac{5(\sigma_{11}+2\sigma_{22})}{126\rho} & \frac{5}{24}&0&0&0&0&0&0 \\
0&0&0&0&0&0 & \frac{5\sigma_{12}}{84\rho} & \frac{5(\sigma_{11}+\sigma_{22})}{84\rho} & \frac{5\sigma_{12}}{84\rho} & 0&\frac{5}{24}&0&0&0&0&0 \\
0&0&0&0&0&0 & -\frac{5(2\sigma_{11}+\sigma_{22})}{126\rho} & \frac{5\sigma_{12}}{126\rho} & -\frac{5(\sigma_{11}-\sigma_{22})}{126\rho} & 0&0&\frac{5}{24}&0&0&0&0 \\
0&0&0&0&0&0 & 0 & 0 & 0 & 0&0&0&\frac{1}{2}&0&0&0&0 \\
0&0&0&0&0&0 & 0 & 0 & 0 & 0&0&0&0&\frac{1}{2}&0&0&0 \\
0&0&0&0&0&0 & 0 & 0 & 0 & 0&0&0&0&0&\frac{1}{2}&0&0 \\
0&0&0&0&0&0 & 0 & 0 & 0 & 0&0&0&0&0&0&\frac{1}{2}&0 \\
0&0&0&0&0&0 & \frac{2(2\sigma_{11}+\sigma_{22})}{3\rho} & \frac{4\sigma_{12}}{3\rho} & \frac{2(\sigma_{11}+2\sigma_{22})}{3\rho} & 0&0&0&0&0&0&0&\frac{2}{3}
\end{pmatrix}$$

The matrix $\mathcal{B}(U)$ can be constructed analogous to $\mathcal{A}(U)$, therefore, we have not given $\mathcal{B}(U)$ here. The transformed system results after eliminating the Navier-Stokes stress and the Fourier heat flux by the actual stress and heat flux, as described in Sec. 3.2.3, reduced matrices $\mathcal{A}(U)$ and $P(U)$ read

$$\mathcal{A}(U) = \begin{pmatrix}
v_1 & \rho & 0 & 0 & 0&0&0 & 0&0&0&0&0&0&0&0&0 \\
\theta & \rho v_1 & 0 & \rho & 0&0&1 & 0&0&0&0&0&0&0&0&0 \\
0 & 0 & \rho v_1 & 0 & 0&0&0 & 1&0&0&0&0&0&0&0&0 \\
0 & \theta\rho+\sigma_{11} & \sigma_{12} & \frac{3\rho v_1}{2} & 1&0&0 & 0&0&0&0&0&0&0&0&0 \\
-\frac{\theta\sigma_{11}}{\rho} & m_{111}+\frac{16q_1}{5} & m_{112}+\frac{2q_2}{5} & \frac{5\theta\rho}{2}+\frac{5\sigma_{11}}{2} & v_1&0&\theta-\frac{\sigma_{11}}{\rho} & -\frac{\sigma_{12}}{\rho}&0&\frac{1}{2}&0&0&0&0&0&\frac{1}{6} \\
-\frac{\theta\sigma_{12}}{\rho} & m_{112}+\frac{7q_2}{5} & m_{122}+\frac{7q_1}{5} & \frac{5\sigma_{12}}{2} & 0&v_1&-\frac{\sigma_{12}}{\rho} & \theta-\frac{\sigma_{22}}{\rho}&0&0&\frac{1}{2}&0&0&0&0&0 \\
0 & \frac{4\theta\rho}{3}+\frac{7\sigma_{11}}{3} & -\frac{2\sigma_{12}}{3} & 0 & \frac{8}{15}&0&v_1 & 0&0&0&0&0&1&0&0&0 \\
0 & 2\sigma_{12} & \theta\rho+\sigma_{11} & 0 & 0&\frac{2}{5}&0 & v_1&0&0&0&0&0&1&0&0 \\
0 & -\frac{2\theta\rho}{3}-\frac{2\sigma_{11}}{3}+\sigma_{22} & \frac{4\sigma_{12}}{3} & 0 & -\frac{4}{15}&0&0 & 0&v_1&0&0&0&0&0&1&0 \\
-\frac{2\theta q_1}{3\rho} & 0 & 0 & -\frac{2q_1}{3} & \frac{2\theta}{3}&0&0 & 0&0&0&0&0&0&0&0&0 \\
-\frac{\theta q_2}{2\rho} & 0 & 0 & -\frac{q_2}{2} & 0&\frac{\theta}{2}&0 & 0&0&0&0&0&0&0&0&0 \\
\frac{\theta q_1}{3\rho} & 0 & 0 & \frac{q_1}{3} & -\frac{\theta}{3}&0&0 & 0&0&0&0&0&0&0&0&0 \\
-\frac{3\theta\sigma_{11}}{5\rho} & 0 & 0 & -\frac{3\sigma_{11}}{5} & 0&0&\frac{3\theta}{5} & 0&0&0&0&0&0&0&0&0 \\
-\frac{8\theta\sigma_{12}}{15\rho} & 0 & 0 & -\frac{8\sigma_{12}}{15} & 0&0&0 & \frac{8\theta}{15}&0&0&0&0&0&0&0&0 \\
-\frac{\theta(5\sigma_{22}-2\sigma_{11})}{15\rho} & 0 & 0 & \frac{1}{15}(2\sigma_{11}-5\sigma_{22}) & 0&0&-\frac{2\theta}{15} & 0&\frac{\theta}{3}&0&0&0&0&0&0&0 \\
\frac{2\theta\sigma_{12}}{5\rho} & 0 & 0 & \frac{2\sigma_{12}}{5} & 0&0&0 & -\frac{2\theta}{5}&0&0&0&0&0&0&0&0 \\
-\frac{8\theta q_1}{\rho} & 0 & 0 & -8q_1 & 8\theta&0&0 & 0&0&0&0&0&0&0&0&0
\end{pmatrix}$$

and

$$\mathcal{P}(U) = \begin{pmatrix}
0&0&0&0&0&0&0&0&0&0&0&0&0&0&0&0&0&0&0&0\\
0&0&0&0&0&0&0&0&0&0&0&0&0&0&0&0&0&0&0&0\\
0&0&0&0&0&0&0&0&0&0&0&0&0&0&0&0&0&0&0&0\\
0&0&0&0&0&0&0&0&0&0&0&0&0&0&0&0&0&0&0&0\\
0&0&0&0&\frac{2}{3}&0&0&0&0&0&0&0&0&0&0&0&0&0&0&0\\
0&0&0&0&0&\frac{2}{3}&0&0&0&0&0&0&0&0&0&0&0&0&0&0\\
0&0&0&0&0&0&1&0&0&0&0&0&0&0&0&0&0&0&0&0\\
0&0&0&0&0&0&0&1&0&0&0&0&0&0&0&0&0&0&0&0\\
0&0&0&0&0&0&0&0&1&0&0&0&0&0&0&0&0&0&0&0\\
0&0&0&0&-\frac{16\,q_1}{45\,\theta\,\rho}&\frac{8\,q_2}{45\,\theta\,\rho}&-\frac{25\,(\sigma_{11}-\sigma_{22})}{126\,\rho}&-\frac{25\,\sigma_{12}}{126\,\rho}&\frac{25\,(\sigma_{11}+2\,\sigma_{22})}{126\,\rho}&\frac{5}{24}&0&0&0&0&0&0&0\\
0&0&0&0&-\frac{4\,q_2}{15\,\theta\,\rho}&-\frac{4\,q_1}{15\,\theta\,\rho}&-\frac{25\,\sigma_{12}}{84\,\rho}&-\frac{25\,(\sigma_{11}+\sigma_{22})}{84\,\rho}&-\frac{25\,\sigma_{12}}{84\,\rho}&0&\frac{5}{24}&0&0&0&0&0&0\\
0&0&0&0&\frac{8\,q_1}{45\,\theta\,\rho}&-\frac{16\,q_2}{45\,\theta\,\rho}&\frac{25\,(2\,\sigma_{11}+\sigma_{22})}{126\,\rho}&-\frac{25\,\sigma_{12}}{126\,\rho}&\frac{25\,(\sigma_{11}-\sigma_{22})}{126\,\rho}&0&0&\frac{5}{24}&0&0&0&0&0\\
0&0&0&0&-\frac{6\,\sigma_{11}}{25\,\theta\,\rho}&\frac{4\,\sigma_{12}}{25\,\theta\,\rho}&-\frac{4\,q_1}{25\,\theta\,\rho}&\frac{8\,q_2}{75\,\theta\,\rho}&0&0&0&0&\frac{1}{2}&0&0&0&0\\
0&0&0&0&-\frac{16\,\sigma_{12}}{75\,\theta\,\rho}&-\frac{2\,(5\,\sigma_{11}-2\,\sigma_{22})}{75\,\theta\,\rho}&-\frac{4\,q_2}{45\,\theta\,\rho}&-\frac{32\,q_1}{225\,\theta\,\rho}&\frac{8\,q_2}{225\,\theta\,\rho}&0&0&0&0&\frac{1}{2}&0&0&0\\
0&0&0&0&\frac{2\,(2\,\sigma_{11}-5\,\sigma_{22})}{75\,\theta\,\rho}&-\frac{16\,\sigma_{12}}{75\,\theta\,\rho}&\frac{8\,q_1}{225\,\theta\,\rho}&-\frac{32\,q_2}{225\,\theta\,\rho}&-\frac{4\,q_1}{45\,\theta\,\rho}&0&0&0&0&0&\frac{1}{2}&0&0\\
0&0&0&0&\frac{4\,\sigma_{12}}{25\,\theta\,\rho}&-\frac{6\,\sigma_{22}}{25\,\theta\,\rho}&0&\frac{8\,q_1}{75\,\theta\,\rho}&-\frac{4\,q_2}{25\,\theta\,\rho}&0&0&0&0&0&0&\frac{1}{2}&0\\
0&0&0&0&-\frac{112\,q_1}{15\,\theta\,\rho}&-\frac{112\,q_2}{15\,\theta\,\rho}&-\frac{10\,(2\,\sigma_{11}+\sigma_{22})}{3\,\rho}&-\frac{20\,\sigma_{12}}{3\,\rho}&-\frac{10\,(\sigma_{11}+2\,\sigma_{22})}{3\,\rho}&0&0&0&0&0&0&0&\frac{2}{3}
\end{pmatrix}$$

respectively. Also the boundary conditions, for the wall normal pointing toward x–direction, are being re-written into

$$U = \mathcal{X}(U)\,U + \mathcal{X}^d,$$

with matrices

$$\mathcal{X}(U) = \begin{pmatrix}
1&0&0&0&0&0&0&0&0&0&0&0&0&0&0&0&0&0&0&0\\
0&0&0&0&0&0&0&0&0&0&0&0&0&0&0&0&0&0&0&0\\
0&0&1&0&0&0&0&0&0&0&0&0&0&0&0&0&0&0&0&0\\
0&0&0&1&0&0&0&0&0&0&0&0&0&0&0&0&0&0&0&0\\
0&0&0&-2\,\xi\,\mathcal{P}\,n_x&0&0&-\frac{1}{2}\,\theta\,\xi\,n_x&0&0&-\frac{5\,\xi\,n_x}{28}&0&0&0&0&0&0&-\frac{\xi\,n_x}{15}\\
0&0&0&0&0&1&0&0&0&0&0&0&0&0&0&0&0&0&0&0\\
0&0&0&0&0&0&1&0&0&0&0&0&0&0&0&0&0&0&0&0\\
0&0&\xi\,(-\mathcal{P})\,n_x&0&0&-\frac{\xi\,n_x}{5}&0&0&0&0&0&0&0&-\frac{\xi\,n_x}{2}&0&0&0&0\\
0&0&0&0&0&0&0&0&1&0&0&0&0&0&0&0&0&0&0&0\\
0&0&0&0&0&0&0&0&0&1&0&0&0&0&0&0&0&0&0&0\\
0&0&7\,\theta\,\xi\,\mathcal{P}\,n_x&0&0&-\frac{11}{5}\,\theta\,\xi\,n_x&0&0&0&0&0&0&0&-\frac{1}{2}\,\theta\,\xi\,n_x&0&0&0&0\\
0&0&0&0&0&0&0&0&0&0&0&1&0&0&0&0&0&0&0&0\\
0&0&0&\frac{2\,\xi\,\mathcal{P}\,n_x}{5}&0&0&-\frac{7}{5}\,\theta\,\xi\,n_x&0&0&-\frac{\xi\,n_x}{14}&0&0&0&0&0&0&\frac{\xi\,n_x}{75}\\
0&0&0&0&0&0&0&0&0&0&0&0&0&1&0&0&0&0&0&0\\
0&0&0&-\frac{1}{5}\,\xi\,\mathcal{P}\,n_x&0&0&\frac{\theta\,\xi\,n_x}{5}&0&-\theta\,\xi\,n_x&0&0&-\frac{\xi\,n_x}{14}&0&0&0&0&-\frac{\xi\,n_x}{150}\\
0&0&0&0&0&0&0&0&0&0&0&0&0&0&0&1&0&0&0&0\\
0&0&0&0&0&0&0&0&0&0&0&0&0&0&0&0&1&0&0&0
\end{pmatrix}$$

and $\mathcal{X}^d(U) = \begin{pmatrix}
0\\0\\0\\0\\
\frac{1}{2}\,\xi\,\mathcal{P}\,n_x\left(\mathcal{V}_2{}^2+4\,\theta^W\right)\\
0\\0\\
\xi\,\mathcal{P}\,n_x\,v_2{}^W\\
0\\0\\
\xi\,(-\mathcal{P})\,n_x\left(6\,\mathcal{V}_2\,\theta^W+\mathcal{V}_2{}^3+7\,\theta\,v_2{}^W\right)\\
0\\
-\frac{1}{5}\,\xi\,\mathcal{P}\,n_x\left(3\,\mathcal{V}_2{}^2+2\,\theta^W\right)\\
0\\
\frac{1}{5}\,\xi\,\mathcal{P}\,n_x\left(4\,\mathcal{V}_2{}^2+\theta^W\right)\\
0\\0
\end{pmatrix}$

where, $\xi = \frac{\chi}{2-\chi}\sqrt{\frac{2}{\pi\theta}}$.

Appendix B

Conservation form of R13–moment equations

For one dimensions, the R13 moment equations can be rewritten in conservation form as [111]

$$\frac{\partial U}{\partial t}+\frac{\partial F}{\partial y}+\frac{\partial F^{\nu}}{\partial y}=\frac{1}{\mathrm{Kn}}\mathcal{S}\left(U\right) \tag{B.1}$$

where again U is the vector of conserved variables which can be expressed as

$$U=\begin{bmatrix} \rho \\ \rho v_1 \\ \rho v_2 \\ \frac{3\theta\rho}{2}+\frac{\rho v^2}{2} \\ p_{11}+\rho v_1^2 \\ \sigma_{12}+\rho v_1 v_2 \\ p_{22}+\rho v_2^2 \\ q_1+\left(p_{11}+\frac{3\theta\rho}{2}+\frac{\rho v^2}{2}\right)v_1+\sigma_{12}v_2 \\ q_2+\left(p_{22}+\frac{3\theta\rho}{2}+\frac{\rho v^2}{2}\right)v_2+\sigma_{12}v_1 \end{bmatrix}$$

while F and F^{ν} are convective and viscous fluxes in $y-$direction, given by

$$F = v_2 U + \begin{bmatrix} 0 \\ \sigma_{12} \\ p_{22} \\ p_{22}v_2 + \sigma_{12}v_1 + q_2 \\ 2\sigma_{12}v_1 + \frac{2q_2}{5} \\ p_{22}v_1 + \sigma_{12}v_2 + \frac{2q_1}{5} \\ 2p_{22}v_2 + \frac{6q_2}{5} \\ \frac{7\theta\sigma_{12}}{2} + \sigma_{12}v_1^2 + \frac{1}{2}\sigma_{12}v^2 + p_{22}v_2v_1 + \frac{7q_2v_1}{5} + \frac{2q_1v_2}{5} \\ \sigma_{12}v_1v_2 + \frac{7\theta p_{22}}{2} + \frac{1}{2}p_{22}v^2 + p_{22}v_2^2 - \rho\theta^2 + \frac{2q_1v_1}{5} + \frac{11q_2v_2}{5} \end{bmatrix}$$

and

$$F^{\nu} = \begin{bmatrix} 0 \\ 0 \\ 0 \\ 0 \\ m_{112} \\ m_{122} \\ m_{222} \\ \frac{R_{12}}{2} + v_1 m_{112} + v_2 m_{122} \\ \frac{R_{22}}{2} + \frac{\Delta}{6} + v_1 m_{122} + v_2 m_{222} \end{bmatrix}.$$

The R13 constitutive relations for m_{ijk}, R_{ij}, and Δ in the above equations are obtained from (3.31), by considering only the linear terms, they read

$$\mathrm{Pr_M}\frac{p}{\mu}m_{111} = \frac{6}{5}\theta\sigma'_{12} \tag{B.2a}$$

$$\mathrm{Pr_M}\frac{p}{\mu}m_{112} = \theta\left(\frac{2}{5}\sigma'_{22} - \sigma'_{11}\right) \tag{B.2b}$$

$$\mathrm{Pr_M}\frac{p}{\mu}m_{122} = -\frac{8}{5}\theta\sigma'_{12} \tag{B.2c}$$

$$\mathrm{Pr_M}\frac{p}{\mu}m_{222} = -\frac{9}{5}\theta\sigma'_{22} \tag{B.2d}$$

and

$$\begin{aligned}
\mathrm{Pr}_{\mathrm{R}}\frac{p}{\mu}R_{11} &= \frac{28}{15}\theta q_2' && \text{(B.3a)}\\
\mathrm{Pr}_{\mathrm{R}}\frac{p}{\mu}R_{12} &= -\frac{14}{5}\theta q_1' && \text{(B.3b)}\\
\mathrm{Pr}_{\mathrm{R}}\frac{p}{\mu}R_{22} &= -\frac{56}{15}\theta q_2' && \text{(B.3c)}\\
\mathrm{Pr}_{\Delta}\,\frac{p}{\mu}\Delta &= -8\theta q_2'. && \text{(B.3d)}
\end{aligned}$$

The source vector $S(U)$ in equation (B.1) has the form

$$S(U) = -\frac{p}{\mu}\left[0,0,0,0,\sigma_{11},\sigma_{12},\sigma_{22},\mathrm{Pr}\,q_1+\sigma_{11}v_1+\sigma_{12}v_2,\mathrm{Pr}\,q_2+\sigma_{12}v_1+\sigma_{22}v_2\right]^T.$$

Bibliography

[1] P. Andries, P. Le Tallec, J. Perlat, and B. Perthame. The Gaussian-BGK model of Boltzmann equation with small Prandtl number. *European Journal of Mechanics - B/Fluids*, 19:813, 2000.

[2] N. Anil. *Optimal Control of Numerical Dissipation in modified KFVS (m-KFVS) using Discrete Adjoint Method*. Ph.d. thesis, Indian Institute of Science, Bangalore.

[3] K. Aoki, H. Yoshida, T. Nakanishi, and A. L. Garcia. Inverted velocity profile in the cylindrical Couette flow of a rarefied gas. *Phys. Rev. E*, 68:016302, 2003.

[4] J. D. Au, M. Torrilhon, and W. Weiss. The shock tube study in extended thermodynamics. *Phys. Fluids*, 13:2423, 2001.

[5] C. BERTHON. Numerical approximations of the 10-moment Gaussian closure. *Math. Comp.*, 75:1809, 2006.

[6] P. L. Bhatnagar and E. P. Gross M. Krook. A model for collision processes in gases. I. Small amplitude processes in charged and neutral one–component systems. *Phys. Rev.*, 94:511, 1954.

[7] G. A. Bird. *Molecular gas dynamics and the direct simulation of gas flows*. Oxford University Press, 1998.

[8] A. V. Bobylev. The Chapman–Enskog and Grad methods for solving the Boltzmann equation. *Soviet Phys. Dolk.*, 27:29, 1982.

[9] A. V. Bobylev. Instabilities in the Chapman–Enskog expansion and hyperbolic Burnett equations. *J. Stat. Phys.*, 124:371, 2006.

[10] A. V. Bobylev. Generalized Burnett hydrodynamics. *J. Stat. Phys.*, 132:569, 2008.

[11] A. V. Bobylev and A. Windfall. Boltzmann equation and hydrodynamics at the Burnett level. *Kinet. Relat. Models*, 5:237, 2012.

[12] P. Taheri Bonab. *Macroscopic description of rarefied gas flows in the transition regime*. Ph.d. thesis, University of Victoria.

[13] S. L. Brown. *Approximate Riemann Solvers for Moment Models of Dilute Gases*. Ph.d. thesis, University of Michigan.

[14] M. Cada. *Compact Third-Order Limiter Functions for Finite Volume Methods*. Ph.d. thesis, Swiss Federal Institute of technology, Zurich.

[15] C. Cai. Heat transfer in vacuum packaged microelectromechanical system devices. *Phys. Fluids*, 20:017103, 2008.

[16] C. Cercignani. *Mathematical methods in kinetic theory*. Plenum Press, 1969.

[17] C. Cercignani. *Theory and application of the Boltzmann equation*. Scottish Academic Press, 1975.

[18] C. Cercignani and M. Lampis. Kinetic models for gas-surface interactions. *Transp. Theory Stat. Phys.*, 1:101, 1971.

[19] S. Chapman and T. G. Cowling. *The mathematical theory of non–uniform gases*. Cambridge University Press, 1970.

[20] T. J. Chung. *Computational Fluid Dynamics*. Cambridge University Press, 2010.

[21] E. Comini, G. Faglia, and G. Sberveglieri (Eds.). *Solid State Gas Sensing*. Elsevier BH, Oxford, 1998.

[22] J. W. Daniel and R. E. Moore. *Computation and Theory in Ordinary Differential Equations*. Freeman, San Francisco, 1970.

[23] S. R. de Groot and Peter Mazur. *Non-equilibrium Thermodynamics*. Dover, 1984.

[24] M. Dehghan. Numerical procedures for a boundary value problem with a non-linear boundary condition. *Appl.Math. Comput.*, 147:291, 2004.

[25] S. L. Dixon. *Fluid mechanics and thermodynamics of turbomachinery.* Elsevier BH, Oxford, 1998.

[26] W. Dreyer. Maximization of the entropy in non-equilibrium. *J. Phys. A: Math. Gen.*, 20:6505, 1987.

[27] Karl Jousten (Editor). *Handbook of Vacuum Technology.* Wiley, 2008.

[28] D. Einzel, P. Panzer, and M. Liu. Boundary condition for fluid flow: Curved or rough surfaces. *Phys. Rev. Lett.*, 64:2269, 1990.

[29] A. H. Epstein. Millimeter-scale, micro-electro-mechanical systems gas turbine engines. *J. Eng. Gas Turbines Power*, 126:205, 2004.

[30] M. A. Gallis, D. J. Rader, and J. R. Torczynski. Calculations of the near-wall thermophoretic force in rarefied gas flow. *Phys. Fluids*, 14:4290, 2002.

[31] L.S. Garcia-Colin, R.M. Velascoa, and F.J. Uribea. Beyond the Navier–Stokes equations: Burnett hydrodynamics. *Physics Reports*, 465:149, 2008.

[32] H. Grad. On the kinetic theory of rarefied gases. *Commun. Pure Appl. Math.*, 2:331, 1949.

[33] H. Grad. *Principles of the kinetic theory of gases*, volume 12 of *Handbuch der Physik.* Springer, Berlin, 1958.

[34] I. A. Graur and A. P. Polikarpov. Comparison of different kinetic models for the heat transfer problem. *J. Heat Mass Trans.*, 46:237, 2009.

[35] X. Gu and D.Emerson. A higher order moment approach for capturing non equlibrium phenomena in the transition regime. *J. Fluid. Mech.*, 636:177, 2009.

[36] X. Gu, D. R. Emerson, and G. Tang. Kramers' problem and the Knudsen minimum: a theoretical analysis using a linearized 26–moment approach. *Cont. Mech. Thermodyn.*, 21:345, 2009.

[37] X. Gu, D. R. Emerson, and G. Tang. Analysis of the slip coefficient and defect velocity in the Knudsen layer of a rarefied gas using the linearized moment equations. *Phys. Rev. E*, 81:016313, 2010.

[38] B. Gustafson and A. Sundstrom. Incompletely parabolic problems in fluid dynamics. *SIAM J. Appl. Math.*, 35:343, 1978.

[39] N. G. Hadjiconstantinou. Comment on Cercignani's second-order slip coeffcient. *Physics of Fluids*, 15:2352, 2003.

[40] N. G. Hadjiconstantinou. Oscillatory shear–driven gas flow in the transition and free–molecular–flow regimes. *Phys. Fluids*, 17:100611, 2005.

[41] L. Halpern. Artificial boundary conditions for incompletely parabolic perturbations of hyperbolic systems. *SIAM J. Math. Alal.*, 22:1256, 1991.

[42] L. H. Holway. Kinetic theory of shock structure using an ellipsoidal distribution function. In *Rarefied Gas Dynamics, (Proceedings of the Fourth International Symposium, University of Toronto, 1964)*, volume I, page 193. Academic Press, New York, 1966.

[43] T. M. M. Homolle and N. G. Hadjiconstantinou. A low-variance deviational simulation Monte Carlo for the Boltzmann equation. *J. Comput. Phys.*, 226:2341, 2007.

[44] S. Jin and M. Slemrod. Regularization of the Burnett equations via relaxation. *J. Stat. Phys.*, 103:1009, 2001.

[45] B. John, X. J. Gu, and D. R. Emerson. Investigation of heat and mass transfer in a lid-driven cavity under nonequilibrium flow conditions. *Numerical Heat Transfer B: Fundamentals*, 58:287, 2010.

[46] T. Kanki and S. Iuchi. Poiseuille flow and thermal ceep of a rarefied gas between parallel plates. *Phys. Fluids*, 16:594, 1973.

[47] G. M. Karniadakis and A. Beskok. *Micro flows: Fundamentals and simulation.* Springer, 2002.

[48] S. Kjelstrup, D Bedeaux, E Johannessen, and J Gross (Author). *Non-equilibrium Thermodynamics for Engineers.* World Scientific Publishing Company, 2010.

[49] M. Knudsen. Eine Revision der Gleichgewichtsbedingung der Gase. Thermische Molekularströmun. *Ann. Phys.*, 31:205, 1910.

[50] M. Knudsen. Thermischer Molekulardruck der Gase in Röhren. *Ann. Phys.*, 33:1435, 1910.

[51] M. N. Kogan. *Rarefied gas dynamics*. Plenum Press, 1969.

[52] G. M. Kremer. *An Introduction to the Boltzmann Equation and Transport Processes in Gases*. Springer, 2010.

[53] I. Kuscer. Reciprocity in scattering of gas molecules by surfaces. *Surface Science*, 25, 1971.

[54] R. J. LeVeque. *Finite Volume Methods for Hyperbolic Problems*. Cambridge University Press, 2002.

[55] C. D. Levermore. Moment closure hierarchies for kinetic theories. *J. Stat. Phys.*, 83:1021, 1996.

[56] C. D. Levermore and W. J. Morokoff. The Gaussian moment closure for gas dynamics. *SIAM J. Appl. Math.*, 59:72, 1998.

[57] T. P. Liu. Hyperbolic conservation laws with relaxation. *Comm. Math. Phys.*, 108:153, 1987.

[58] R. G. Lord. Some extensions to the Cercignani-Lampis gas-surface scattering kernel. *Phys. Fluids*, 3:710, 1991.

[59] S. K. Loyalka. Momentum and temperature slip coefcients with arbitrary accommodation at the surface. *J. Chem. Phys.*, 48:5432, 1968.

[60] S. K. Loyalka. Velocity profile in the Knudsen layer for the Kramer's problem. *Phys. Fluids*, 18:1666, 1975.

[61] S. K. Loyalka. Temperature jump and thermal creep slip: Rigid sphere gas. *Phys. Fluids A*, 1:403, 1989.

[62] S. K. Loyalka and J. W. Cipolla. Thermal creep slip with arbitrary accommodation at the surface. *Phys. Fluids*, 14:1656, 1971.

[63] S. K. Loyalka, N. Petrellis, and T. S. Storvick. Some numerical results for the BGK model: Thermal creep and viscous slip problems with arbitrary accomodation at the surface. *Phys. Fluids*, 18:1094, 1975.

[64] C. Maxwell. On stress in rarefied gases arising from inequalities of temperature. *Phil. Trans. Roy. Soc. Lon.*, 170:231, 1879.

[65] J. C. McDonald. *Extended fluid-dynamic modelling for numerical solutions of micro-scale flows*. Ph.d. thesis, University of Toronto.

[66] J. G. McDonald and C. P. T. Groth. Extended uid-dynamic model for micron-scale ows based on gaussian moment closure. *AIAA*, page 20080691, 2008.

[67] Simon Mizzi. *Extended macroscopic models for rareed gas dynamics in micro-sized domains*. Ph.d. thesis, University of Strathclyde.

[68] A. Mohammadzadeh and H. Niazmand. A parallel DSMC investigation of monatomic/diatomic gas flow in micro/nano cavity. *Num. heat trans. part A: applications*, 63:305, 2013.

[69] A. Mohammadzadeh, E. Roohi, and R. S. Myong H. Niazmand, S. Stefanov. Thermal and second-law analysis of a micro- or nanocavity using direct-simulation Monte Carlo. *Physical review E*, 85:056310, 2012.

[70] A. Mohammadzadeh, E. Roohi, and S. Stefanov H. Niazmand. Detailed investigation of thermal and hydrodynamic flow behaviour in micro/nano cavity using DSMC and NSF equation. *Proc. of the ASME 2011*, 2011.

[71] I. Müller. *Thermodynamics*. Pitman, Boston, 1985.

[72] I. Müller. Extended thermodynamics: a theory of symmetric hyperbolic field equations. *Entropy*, 10:477, 2008.

[73] I. Müller and T. Ruggeri. *Rational Extended Thermodynamics*. Springer, 1998.

[74] S. Naris and D. Valougeorgis. The driven cavity flow over the whole range of the Knudsen number. *Phys. Fluids*, 17:097106, 2005.

[75] T. Ohwada, Y. Sone, and K. Aoki. Numerical analysis of the Poiseuille and thermal transpiration flows between two parallel plates on the basis of the Boltzmann equation for hard–sphere molecules. *Phys. Fluids A*, 1:2042, 1989.

[76] T. Ohwada, Y. Sone, and K. Aoki. Numerical analysis of the shear and thermal creep flows of a rarefied gas over a plane wall on the basis of the linearized Boltzmann equation for hard–sphere molecules. *Phys. Fluids A*, 1:1588, 1989.

[77] L. Pareschi and G. Russo. Implicit-explicit Runge-Kutta schemes and applications to hyperbolic systems with relaxation. *J. Sci. Comput.*, 25:129, 2005.

[78] J. H. Park, P. Bahukudumbi, and A. Beskok. Rarefaction effects on shear driven oscillatory gas flows: A direct simulation Monte Carlo study in the entire Knudsen regime. *Phys. Fluids*, 16:317, 2004.

[79] A. Rana, M. Torrilhon, and H. Struchtrup. Numerical solution of the moment equations using kinetic flux-splitting schemes. *Proc. 28th Symposium on Rarefied Gas Dynamic, AIP Conference Proceedings 1501*, page 287, 2012.

[80] A. Rana, M. Torrilhon, and H. Struchtrup. A robust numerical method for the R13 equations of rarefied gas dynamics: Application to lid driven cavity. *J. Comp. Phys.*, 236:169, 2012.

[81] P. L. Roe. Approximate Riemann solvers, parameter vectors and difference schemes. *J. Comp. Phys.*, 43:357, 1981.

[82] E. Roohi, M. Darbandi, and V. Mirjalili. Direct simulation Monte Carlo solution of subsonic flow through micro/nanoscale channels. *J. Heat Trans.*, 131:92402, 2009.

[83] A. Schuetze. *Direct Simulation by Monty Carlo modelling Couette flow using dcmc1as.f: A user's manual.* Project report, University of Michigan.

[84] F. Sharipov and D. Kalempa. Oscillatory Couette flow at arbitrary oscillation frequency over the whole range of the Knudsen number. 4:363, 2008.

[85] F. Sharipov and V. Seleznev. Data on internal rarefied gas flows. *J. Phys. Chem. Ref. Data*, 27:657, 1998.

[86] F. M. Sharipov and G. M. Kremer. Nonlinear Couette flow between two rotating cylinders. *Transp. Theory Stat. Phys.*, 25:217, 1996.

[87] F. M. Sharipov and G. M. Kremer. Non–isothermal couette flow of a rarefied gas between two rotating cylinders. *European J. Mechanics – B/Fluids*, 18:121, 1999.

[88] L. H. Söderholm. Hybrid Burnett equations: A new method of stabilizing. *Trans. Theory and Stat. Phys.*, 36:495, 2007.

[89] Y. Sone. *Kinetic theory and fluid dynamics*. Birkhäuser, 2002.

[90] Y. Sone. Comment on "heat transfer in vacuum packaged microelectromechanical system devices" [Phys. Fluids 20, 017103 (2008)]. *Phys. Fluids*, 21:119101, 2009.

[91] Y. Sone and T. Doi. Ghost effect of infinitesimal curvature in the plane Couette flow of a gas in the continuum limit. *Phys. Fluids*, 16:952, 2004.

[92] Y. Sone, Sh. Takata, and H. Sugimoto. The behavior of a gas in the continuum limit in the light of kinetic theory: The case of cylindrical Couette flows with evaporation and condensation. *Phys. Fluids*, 8:3403, 1996.

[93] Y. Sone, Y. Waniguchi, and K. Aoki. One–way flow of a rarefied gas induced in a channel with a periodic temperature distribution. *Phys. Fluids*, 8:227, 1996.

[94] J. Strikwerda. *Initial boundary value problems for incompletely parabolic systems*. Ph.d. thesis, Stanford University.

[95] H. Struchtrup. Kinetic schemes and boundary conditions for moment equations. *Z. angew. Math. Phys.*, 51:346, 2000.

[96] H. Struchtrup. Stable transport equations for rarefied gases at high orders in the Knudsen number. *Phys. Fluids*, 16:3921, 2004.

[97] H. Struchtrup. *Macroscopic transport equations for rarefied gas flows: Approximation methods in kinetic theory*. Springer, 2005.

[98] H. Struchtrup. Scaling and expansion of moment equations in kinetic theory. *J. Stat. Phys.*, 125:565, 2006.

[99] H. Struchtrup. Linear kinetic heat transfer: Moment equations, boundary conditions, and Knudsen layers. *Physica A*, 387:1750, 2008.

[100] H. Struchtrup. Resonance in rarefied gases. *Cont. Mech. Thermodyn.*, 24:361, 2012.

[101] H. Struchtrup. Maxwell boundary condition and velocity dependent accommodation coefficient. *Phys. Fluids*, 2013.

[102] H. Struchtrup and M. Torrilhon. Regularization of grad's 13–moment equations: Derivation and linear analysis. *Phys. Fluids*, 15:2668, 2003.

[103] H. Struchtrup and M. Torrilhon. H theorem, regularization, and boundary conditions for linearized 13–moment equations. *Phys. Rev. Lett.*, 99:014502, 2007.

[104] H. Struchtrup and M. Torrilhon. Higher–order effects in rarefied channel flows. *Phys. Rev. E*, 78:046301, 2008.

[105] H. Struchtrup and M. Torrilhon. Regularized 13 moment equations for hard sphere molecules: Linear bulk equations. *Phys. Fluids*, 25:052001, 2013.

[106] P. Taheri, A. S. Rana, H. Struchtrup, and M. Torrilhon. Macroscopic description of steady and unsteady rarefaction effects in boundary value problems of gas dynamics. *Cont. Mech. Thermodyn.*, 21:423, 2009.

[107] P. Taheri and H. Struchtrup. Effects of rarefaction in microflows between coaxial cylinders. *Phys. Rev. E*, 80:066317, 2009.

[108] P. Taheri, M. Torrilhon, and H. Struchtrup. Couette and Poiseuille microflows: Analytical solutions for regularized 13–moment equations. *Phys. Fluids*, 21:017102, 2009.

[109] K. W. Tibbs, F. Baras, and A. L. Garcia. Anomalous flow profile due to the curvature effect on slip length. *Phys. Rev. E*, 56:2282, 1997.

[110] E. F. Toro. *Riemann Solvers and Numerical Methods for Fluid Dynamics*. Springer, 2009.

[111] M. Torrilhon. Two-dimensional bulk micro-flow simulations based on regularized Grad's 13-moment-equations. *SIAM Multiscale Model. Sim.*, 5:695, 2006.

[112] M. Torrilhon. Hyperbolic moment equations in kinetic gas theory based on multi-variate pearson-iv-distributions. *Comm. Comput. Phys.*, 7:639, 2010.

[113] M. Torrilhon. Slow rarefied flow past a sphere: Analytical solutions based on moment equations. *Phys. Fluids*, 22:072001, 2010.

[114] M. Torrilhon. H-theorem for nonlinear regularized 13-moment equations in kinetic gas theory. *Kinetic and Related Models*, 5:185, 2012.

[115] M. Torrilhon. Krylov-Riemann-solver for large systems of hyperbolic systems of conservation laws. *SIAM Sci. Comp.*, 34:2072, 2012.

[116] M. Torrilhon, J. D. Au, and H. Struchtrup. Explicit fluxes and productions for large systems of the moment method based on extended thermodynamics. *Cont. Mech. Thermodyn.*, 15:97, 2003.

[117] M. Torrilhon and H. Struchtrup. Regularized 13–moment–equations: Shock structure calculations and comparison to Burnett models. *J. Fluid Mech.*, 513:171, 2004.

[118] M. Torrilhon and H. Struchtrup. Boundary conditions for regularized 13–moment–equations for micro–channel flows. *J. Comp. Phys.*, 227:1982, 2008.

[119] Heat transfer in micro devices packaged in partial vacuum. *JPCS*, 362:012034, 2012.

[120] C. Truesdell and R. G. Muncaster. *Fundamentals of Maxwell's kinetic theory of a simple monatomic gas*. Academic Press, 1980.

[121] S. Varoutis, D. Valougeorgis, and F. Sharipov. Application of the integro-moment method to steady-state two-dimensional rarefied gas flows subject to boundary induced discontinuities. *J. Comput. Phys.*, 227:6272, 2008.

[122] W. Wagner. A convergence proof for Bird's direct simulation monte carlo method for the boltzmann equation. *J. Stat, Phys.*, 66:1011, 1992.

[123] Q. Wang, X. Yan, and Q. He. Heat-flux-specified boundary treatment for gas flow and heat transfer in microchannel using direct simulation monte carlo method. *Int. J. Numer. Meth. Engng.*, 74:1009, 2008.

[124] A. Westerkamp and M. Torrilhon. Slow rarefied gas flow past a cylinder: Analytical solution in comparison to the sphere. *Proc. 28th Symposium on Rarefied Gas Dynamic, AIP Conference Proceedings 1501*, page 207, 2012.

[125] K. Xu, Martinelli, and A. Jameson. A gas-kinetic BGK scheme for the Navier–Stokes equations and its connection with artificial dissipation and Godunov method. *J. Comp. Phys.*, 171:289, 2001.

[126] J. B. Young. Calculation of Knudsen layers and jump conditions using the linearised G13 and R13 moment methods. *Int. J. Heat and Mass Trans.*, 54:2902, 2012.

[127] S. Yuhong, R. W. Barber, and D. R. Emerson. Inverted velocity profiles in rarefied cylindrical Couette gas flow and the impact of the accommodation coefficient. *Phys. Fluids*, 17:047102, 2005.

[128] X. Zhong, R. W. MacCormack, and D. R. Chapman. Stabilization of the Burnett equations and applications to hypersonic flows. *AIAA Journal*, 31:1036, 1993.